THE CHEMISTRY OF IGNITION IMPROVERS

By

Mark David Poxon

A Thesis Submitted for the

Degree of Doctor of Philosophy

University of York

Department of Chemistry

September 1990

This thesis is dedicated to my mother and father

ABSTRACT

We have attempted to understand the empirical activity order of a variety of diesel fuel ignition improvers that, previously, have been found to sensitize the autoignitions of hydrocarbon and oxygen containing mixtures. Accordingly, the empirical activity order 2-^{n}butoxyethyl nitrate (BEN) > 2-methoxyethyl nitrate (MEN) > di-^{t}butyl peroxide (DTBP) > ^{i}propyl nitrate (IPN) has been investigated from, first, the low temperature pyrolyses of these materials, where the decomposition reactions of the initial pyrolyte alkoxy radicals were found to be ubiquitously important. Second, an autoignition study of the performance of nitrogen dioxide as an ignition improver, that was analogous to the previous nitrate and peroxide studies, has shown that the activities of the nitrate ignition improvers derive mainly from the alkoxy rather than the nitrogen dioxide moieties of these materials. An understanding of the activity order BEN > MEN > DTBP > IPN has been advanced then based on the various possible oxidations of the alkyl radicals, that are produced in the sequential pyrolyses of these ignition improvers and their daughter alkoxy radicals, and correlates with the ease of hydroxy radical formation in these processes.

ACKNOWLEDGEMENTS

I wish to record my gratitude to my many supervisors, Professor D.J. Waddington, Dr. C. Anastasi, Dr. C. Morley (Shell Research, Thornton, Ltd.) and Dr. P. Pagsberg (Danish National Laboratory, Riso) for their support, guidance and encouragement both of these studies and of this student.

Thanks also to Messrs. S.W. Moehr, A. Watson, C.H. Brookes and I. Brookes, for their technical assistance and to my friends, Dr. R.N. Cawthorne, Mr. J.D. Howson, Mr. D. McGrady, Mr. P. Herrmann, Mr. J.P. Heawood and Mrs. J. Spencer for their invisible support.

Finally thanks to Mrs. J. Lumley and Mr. J. Olive for helping in the final stages of preparing this thesis.

The Science and Engineering Research Council and Shell Research Ltd. are gratefully acknowledged for their joint financial assistance.

CONTENTS

CHAPTER 1 INTRODUCTION

(1.1) PREAMBLE

The petrochemical industry always aims to be competitive and ultimately attains this through the abilities to influence and respond to market desires. For instance, diesel fuels are now produced to contain ignition improving additives either to make better use of petrochemical resources or to be marketed as superior products.

Diesel fuels have been empirically formulated to contain ignition improving additives for a long time[1]. This formulation has rested on the measured cetane number improvements of a diesel fuel, that contained a range of single ignition improvers, under standard engine conditions[2], and features organic nitrates as the most promising class of improver.

Recent attempts[3,4] have been made, at the Thornton Research Centre, to base the use of diesel fuel ignition improvers on a more careful empiricism, from the autoignitions of diesel fuels, that singly contain these additives, under simplified rapid compression conditions. These studies are removed from the complications of the engine cycle, that is repetitive and involves a diesel injection, and are performed following the single stroke compression of a gaseous premix in a rapid compression machine (r.c.m.). The rapid compression raises both the pressure and temperature of these mixtures to precondition an autoignition. The autoignition process is manometrically followed from the end of compression to the ignition, where the phenomenological ignition delay is recorded between these

states. Various autoignition behaviours are observed in these experiments, including the two stage ignitions, with a cool flame first stage, and the single stage hot ignitions, that are both observed in static, low pressure studies[5]. Figure (1.1) shows the pressure–time evolutions during and following the rapid compression of a primary reference fuel (P.R.F.), 10% oxygen and ~ 90% diluent mixture to (a) 17.7 bar and 650K, where a two stage autoignition is observed and where the cool flame pressure pulse is clearly marked ΔP and (b) 20.4 bar and 760K, where a single stage autoignition is observed. The figure emphasises the measurement of ignition delays (t), which are recorded from the peak pressure reached by the compression to the maximum rate of pressure rise during the hot ignition (the total ignition delay). In the two stage autoignition case, this measurement can be divided between the first and second stage delays, where the maximum rate of cool flame pressure rise differentiates between the two stages.

Kirsch and Selby have respectively studied the effects of 2–^{n}butoxyethyl nitrate (BEN), 2–methoxyethyl nitrate (MEN), di–^{t}butyl peroxide (DTBP) and ^{i}propyl nitrate (IPN) on the autoignitions of a P.R.F., oxygen, diluent mixture at end of compression temperatures (e.o.c.t.'s) of 650 and 760K. The P.R.F. used in these studies was a 7:3 mixture of ^{i}octane and ^{n}heptane, with a research octane number (R.O.N.) of 70. The above ignition improvers were individually incorporated into the aforementioned mixtures, at various mole fraction ratios compared to the fuel, and the ignition delays of these modified mixtures were recorded following their rapid compressions. In these experiments, the ignition improvers always produced shorter ignition delays compared to the identically compressed unmodified mixtures and, to compare the

Figure (1.1) Pressure-time evolutions during and following the rapid compressions of (a) P.R.F., 10% O_2,~ 90% N_2 (e.o.c.t. = 650K) and (b) P.R.F., 10% O_2, 30% N_2,~ 60% Ar (e.o.c.t. = 760K) mixtures

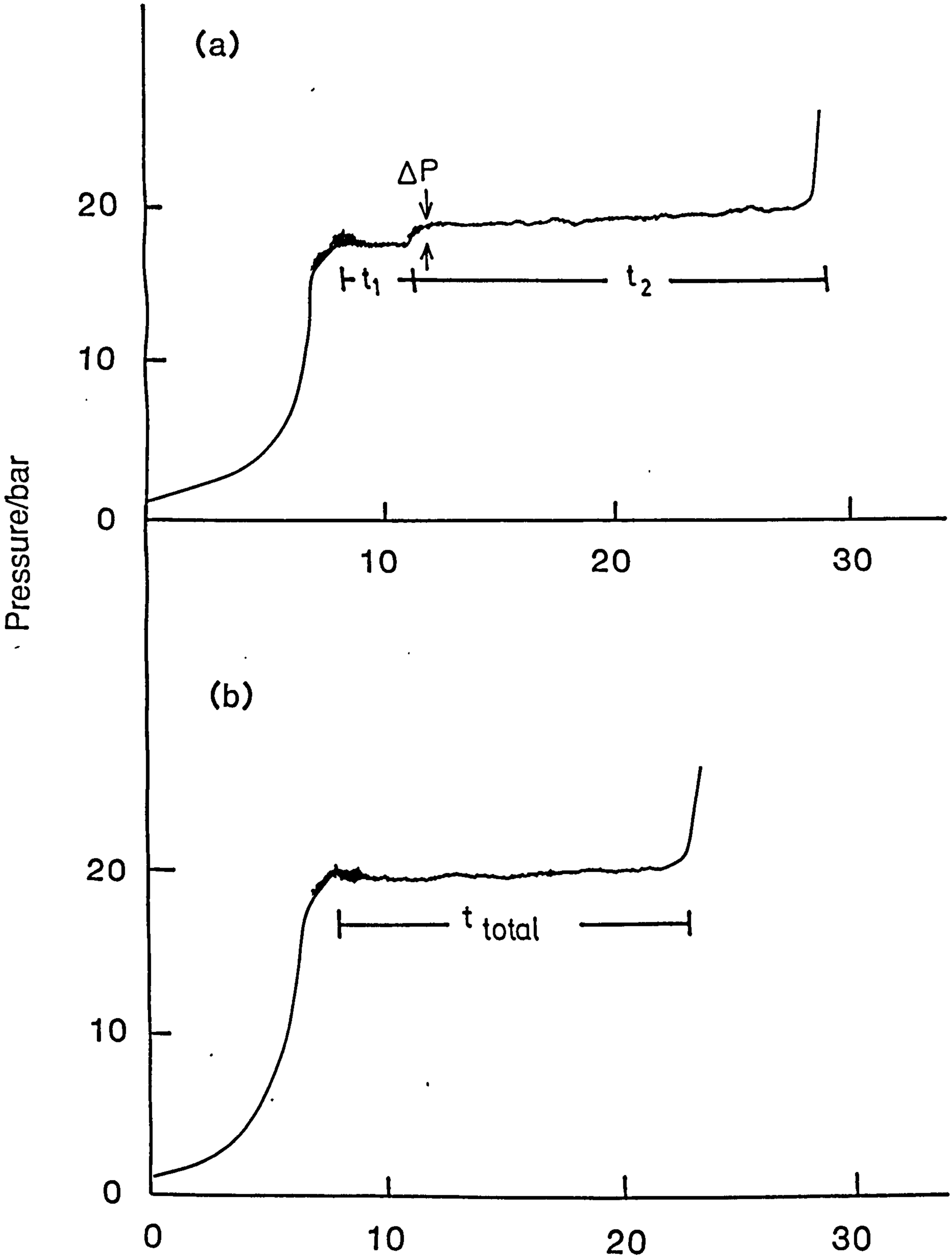

effects of these materials at 650 and 760K, these shortenings are expressed as fractions of the comparable unmodified ignition delays. Figure (1.2) shows then the fractional shortenings in the ignition delays, $\Delta t/t$, of a R.O.N. 70, 10% oxygen, ~ 90% diluent mixture, caused by the various mole fraction additions of a variety of ignition improvers at (a) 650 (b) 760K. These studies show the empirical order of ignition improver effectiveness to be BEN > MEN > DTBP > IPN, and, particularly, show the ether nitrates to be more active, in this regard, than either the nitrate or the peroxide.

Essentially, the study of this thesis aims to provide a chemical understanding of the behaviour of ignition improvers, according to the above rank order, and, thereby, to identify the desirable features of an ignition improving material.

This understanding has been approached from studies of both the low temperature pyrolyses of the above ignition improvers and by an experimental and theoretical autoignition study of nitrogen dioxide, a pyrolysis product of the (ether) nitrates, that is comparable to the ignition improver studies of Kirsch and Selby.

In support of these pyrolysis and autoignition studies, the previous pyrolyses of ignition improving materials, the studied chemistries of these initial pyrolyte organic radicals and the available theoretical autoignition models will now be briefly surveyed.

(1.2) THE PYROLYSES OF ORGANIC NITRATES PEROXIDES AND NITRITES

The pyrolyses of organic nitrates[6] ($RONO_2$), peroxides[7,8] (ROOR) and the related nitrites[9] (RONO) have been subject to

Figure (1.2) Fractional ignition delay shortenings of rapidly compressed RON 70, 10% oxygen, ~ 90% diluent mixtures at e.o.c.t's of (a) 650K (b) 760K.

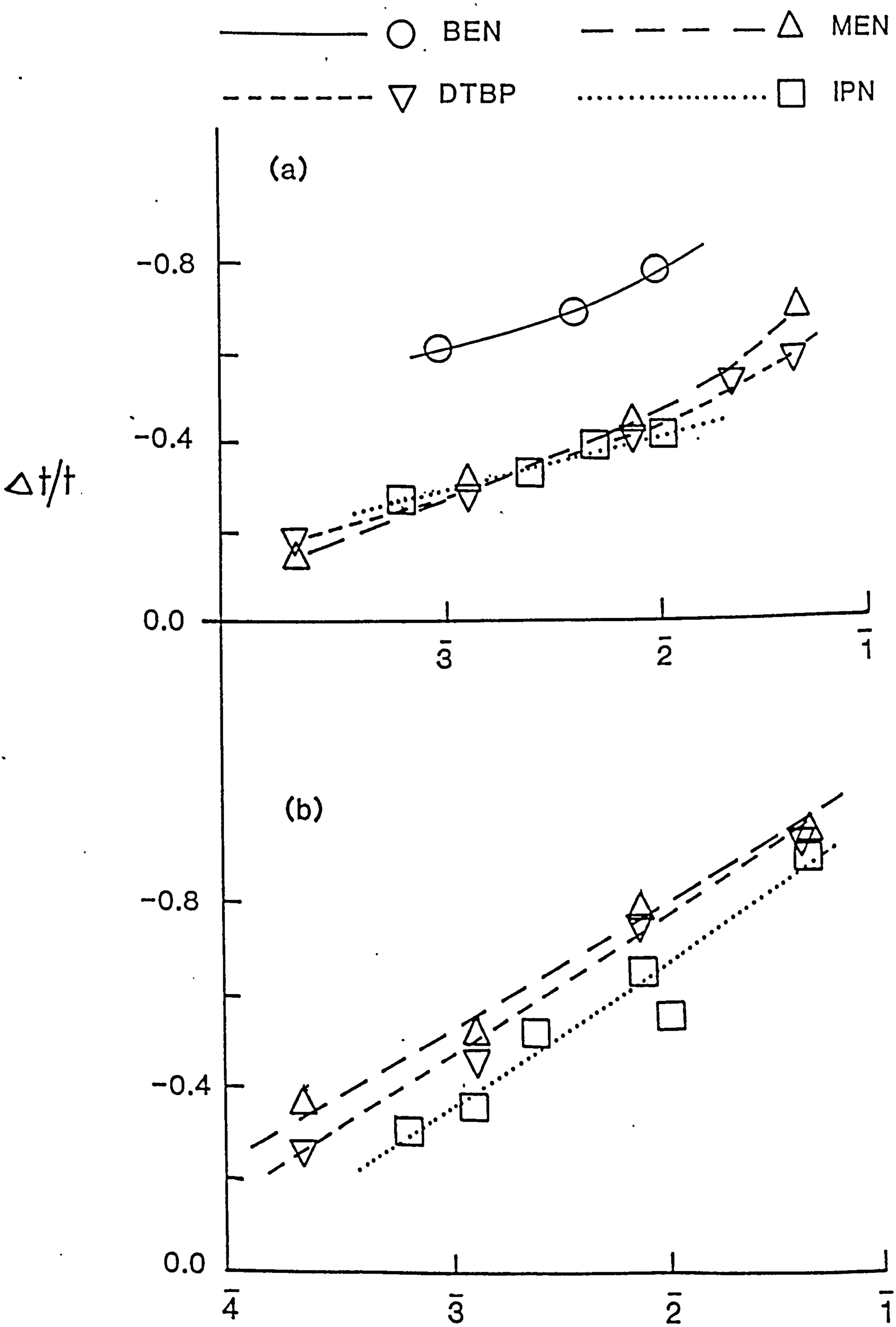

numerous recent reviews.

These pyrolysis studies began in the 1930s and aimed at the manometric determination of the overall Arrhenius parameters of these processes. On the basis of the similarities that emerged, these pyrolyses were asssumed to be uncomplicated homogenous first order processes, and the measured Arrhenius parameters were associated with the homolyses of the weakest bonds in the pyrolytes. The pyrolyses of these materials then, in each case, provide an alkoxy radical (RO·) as an initial product.

$$ROOR \longrightarrow RO\cdot + RO$$

$$RONO \longrightarrow RO\cdot + NO$$

$$RONO_2 \longrightarrow RO\cdot + NO_2$$

These early pyrolysis studies were suggested to be kinetically discrepant, however, by two subsequent developments. First, Benson, in 1958[10], proposed a group additivity based thermochemistry that was later quantified for organic nitrates, peroxides and nitrites[11]. Second, a large number of kinetic measurements on the pyrolysis of di-^{t}butyl peroxide[12] were concurrently made, and, by virtue of the exceptional stability of this peroxide, were in remarkably good agreement, both internally and with Benson's new thermochemical system. The suggestion then was that the early pyrolyses of these material classes should have proceeded with group additivity activation energies and, by discrepancy, had generally failed to isolate the homolyses of the weakest pyrolyte bonds. These pyrolysis studies were therefore generally considered to have involved a mixed homolytic and chain decomposition of the pyrolytes and consequently were repeated under conditions designed to eliminate this chain

complication.

This was achieved in various ways that included limiting the pyrolyses to small extents of reaction, the use of radical traps, generally nitrogen dioxide or nitric oxide, and by performing the pyrolyses at very low pressures. These studies are summarised in table (1.1) which, in each case, shows the pyrolysis conditions, the measured Arrhenius parameters and the method of analysis.

The first pyrolysis studies to employ radical traps were performed by Leggett and Thynne[13], who pyrolysed diethyl and di-^{i}propyl peroxides in nitric oxide and, subsequently, by Batt[14] and Benson[15], who independently pyrolysed dimethyl peroxide in the presence of nitrogen dioxide. Additionally, oxygen has been used as a radical trap in the pyrolyses of di-^{n}butyl and di-^{n}heptyl peroxides in a recent study by Rigny[16].

The pyrolyses of the nitrites were most comprehensively restudied by Batt, who has pyrolysed small concentrations of the methyl[12], ethyl[18], ^{i}propyl[19], ^{s}butyl[20] and ^{t}amyl[20] members of this material class, to only small extents of reaction.

Non chain conditions have also been achieved using the Very Low Pressure Pyrolysis (V.L.P.P.) technique[21], where Benson[22] has remeasured the Arrhenius parameters for the decompositions of ^{t}butyl nitrite and ^{n}propyl nitrate. A similar study of ^{n}butyl nitrite was performed by Golden[23].

Table (1.1) shows that the careful pyrolyses of ROX, where X = NO_2, OR or NO, occur with activation energies that, within experimental error, are independent of the identity of R, in accord with the principles of group additivity. The activation energy for the pyrolysis is given then by D(RO-X)-RT, where D(RO-X) is the

Table (1.1) The thermal decompositions of organic nitrates, peroxides and nitrites

System.	Technique.	Arrhenius Parameters. $\log_{10}(A/s^{-1})$.	E/kcal mol^{-1}.	Method of Analysis.	Ref.
$(MeO)_2 + NO_2$	Static	15.7	37.1	M	14
$(MeO)_2 + NO_2$	Static	13.9	33.76	GC	15
$(EtO)_2 + NO$	Static	16.1	37.3	MS	13
$(^{i}Pro)_2 + NO$	Static	15.4	37.1	MS	13
$(^{n}BuO)_2 + O_2$	Flow	16.0	38.3	Wet chemical analysis	16
$(^{n}HpO)_3 + O_2$	Flow	15.0	36.5	ESR of trapped $HO_2\cdot$	16
MeONO	Static, LPP	15.9	41.3 ± 0.8	GC	17
EtONO	Static, LPP	16.0	41.8 ± 0.9	GC	18
^{i}PrONO	Static, LPP	16.2	41.0 ± 0.8	GC	19
^{s}BuONO	Static, LPP	16.2	40.9 ± 0.8	GC	20
^{t}AmONO	Static, LPP	16.3	40.3 ± 0.1	GC	20
^{t}BuONO	VLPP	15.8	39.3	MS	22
^{n}BuONO	VLPP	16.5	41.0	MS	23
$^{n}PrONO_2$	VLPP	16.5	40.0	MS	22
$EtONO_2 + NO$	Static	16.9	41.2 ± 0.5	IR	24

LPP = Low Pressure Pyrolysis, VLPP = Very Low Pressure Pyrolysis, M = Manometry.
GC = Gas Chromatography, MS = Mass Spectrometry, IR = Infra-red Spectroscopy.

dissociation energy of this bond and T is the mean temperature of the study. The activation energy differences between the nitrates, peroxides and nitrites therefore reflect differences in the respective group values of D(RO–X). The most accurate thermochemical kinetic values for these are $D(RO-NO_2)$ = 41.4 kcal mol^{-1} [25], D(RO–OR) = 37.8 kcal mol^{-1} [26] and D(RO–NO) = 41.5 kcal $mol.^{-1}$ [9].

(1.3) THE CHEMISTRY OF ALKOXY RADICALS

The chemistry of alkoxy radicals has been the subject of two recent reviews[9,27]. Generally, the pyrolysis or photolysis of an organic nitrate, peroxide or nitrite has been used to generate these radicals in an environment where the reactions of this species, mostly the decomposition, metathesis with oxygen or isomerization reactions, could be selectively studied.

The alkoxy radical decomposition reactions have mainly been studied by Batt[17–20,28], who has independently pyrolysed a variety of organic peroxides and nitrites in nitric oxide and, to promote the radical decomposition reaction, in up to 0.9 bar of carbon tetrafluoride. These conditions allowed a relative rate measurement of the alkoxy radical decomposition reaction against the competing addition reaction of this radical with nitric oxide. The competition kinetics of the addition reaction were obtained from the pyrolysis kinetics of the neat nitrite, together with the appropriate group additivity entropy change for this homolysis.

$$ROOR \longrightarrow RO\cdot + RO$$

$$RONO \longrightarrow RO\cdot + NO$$

$$RO\cdot \longrightarrow \text{Products}$$

$$RO\cdot + NO \longrightarrow RONO$$

Varying the amount of carbon tetrafluoride showed that the rates of the alkoxy radical decomposition reactions are pressure dependent and consequently R.R.K.M. theory was used to correct the measured data to the high pressure limits. In the pyrolysis of methyl nitrite, it was necessary to offer isobutane as the competing agent for the methoxy radical removal due to the relative stability of this radical to decomposition. The limiting high pressure Arrhenius parameters, obtained by Batt, for the decompositions of the methoxy[17], ethoxy[18], ^{i}propoxy[19], ^{s}butoxy[20], ^{t}butoxy[28] and ^{t}amyloxy[20] radicals are given in table (1.2).

The alkoxy radical reactions with oxygen have occasioned the use, by Gutman[29], of Laser Induced Fluorescence[30] (L.I.F.), as a direct technique, to study this reactivity of several small members of this radical type. Accordingly, the reaction kinetics of the methoxy and ethoxy radical with oxygen were respectively measured between 413 and 628K, where $\log_{10}$ (k/M^{-1} s^{-1}) = 7.8–2.6 kcal mol^{-1}/RT ln 10 and at 296 and 353K, where the second order rate constant increased from 4.8×10^6 to 5.9×10^6 M^{-1} s^{-1}.

The alkoxy radical isomerization reactions have hardly been studied and mention will only be made of a recent, and elegant, study of the isomerization of the 2–pentoxy radical by Berces[31].

The general difficulty of these studies arises from the reactive

Table (1.2) Recommended Arrhenius parameters for the decomposition of alkoxy radicals

Radical.	Decomposition products.	$\log_{10}(A/s^{-1})$.	E/kcal mol^{-1}.	Ref.
MeO·	CH_2O + H·	13.4	27.5	17
EtO·	CH_2O + Me·	13.9	21.5	18
^{i}PrO·	MeCHO + Me·	14.6 ± 0.5	17.2 ± 1.0	19
^{s}BuO·	MeCHO + Et·	14.9 ± 0.5	15.3	20
^{t}BuO·	Me_2CO + Me·	14.0 ± 0.4	15.0 ± 0.1	28
^{t}AmO·	Me_2CO + Et·	14.7 ± 0.2	14.3 ± 1.0	20

radical products of the isomerization reaction, that convolute this reaction into other processes. Berces has overcome this difficulty by the efficient trapping of the isomerized 2–pentoxy radical with the methyl radical, to produce an easily observable molecular product, 2–hexanol.

Berces then has cophotolysed both di–2–pentyl peroxide, or 2–pentyl nitrite, in the presence of excess azomethane, and determined, from the relative yields of 2–hexanol and acetaldehyde, the competition kinetics of the 2–pentoxy radical isomerization reaction against the decomposition reaction of this radical.

$$C_5H_{11}O_2C_5H_{11} + h\upsilon \longrightarrow 2\ C_5H_{11}O\cdot$$

$$CH_3N_2CH_3 + h\nu \longrightarrow 2\ CH_3\cdot + N_2$$

$$CH_3\underset{\underset{O\cdot}{|}}{C}HCH_2CH_2CH_3 \longrightarrow CH_3CHO + {}^{n}Pr\cdot$$

$$CH_3\underset{\underset{O\cdot}{|}}{C}HCH_2CH_2CH_3 \longrightarrow CH_3\underset{\underset{OH}{|}}{C}HCH_2CH_2CH_2\cdot$$

$$CH_3\underset{\underset{OH}{|}}{C}HCH_2CH_2CH_2 + CH_3\cdot \longrightarrow CH_3\underset{\underset{OH}{|}}{C}HCH_2CH_2CH_2CH_3$$

The reference kinetics were determined, as part of this study, from the competition kinetics of the 2–pentoxy radical reactions by decomposition or with nitric oxide, under isomerization precluding conditions. Berces then has obtained the rate expression for the 2–pentoxy radical isomerization reaction to be $\log_{10}$ (k/s^{-1}) 11.7–9.5 kcal mol^{-1}/RT ln 10, over the temperature range 279 to 385K.

(1.4) AUTOIGNITION MODELS

An autoignition model has been used in a purely theoretical and previous investigation of the autoignition of a sprayed diesel fuel, ignition improver mixture[32]. The autoignition model was based on a gasoline engine knock model[33] that was physically extended to include the break up and evaporation of the spray, and allowed the relationships between these physical processes and the ignition improver activity to be explored. This autoignition investigation aimed at gauging the physico-chemical complexities of developing ignition improvers for engine applications and emphasized the need to carefully understand the autoignition behaviour of these materials in a physically simple situation. Our autoignition study of nitrogen dioxide, under r.c.m. conditions, conforms to this, and, was modelled to contribute to the above understanding concerning organic nitrates.

Accordingly, the autoignition properties of nitrogen dioxide have, in this work, been investigated using a model provided by Cox and Cole[34]. The Cox and Cole model was developed from an earlier model, produced at Thornton, by Halstead, Kirsch, Prothero and Quinn[32,35], that was based on r.c.m. studies of hydrocarbon autoignition. The Thornton model contained recognition that the phenomena of hydrocarbon autoignition could be understood thermo-kinetically[36]. The cool flames, thereof, were considered then to arise from a thermally driven mechanism change, effected by a thermo-kinetic switch, that in the cool flame quenching, decreased the branching rate relative to the termination rate. The Thornton model was expressed as a generalized reaction scheme for hydrocarbons, and implicitly contained the accepted cool flame "peroxy radical isomerization and decomposition"[37] and post cool flame "conjugate

olefin"[38] mechanisms for the oxidations of these materials. The thermokinetic switch between these mechanisms was provided by a varying alkyl radical reactivity towards oxygen, that switches from oxygenation to metathesis during a cool flame passage. The Cox and Cole model, we have used, is essentially a more explicit version of the Thornton model, that includes an updated and more detailed chemical understanding[39,40] of the elementary reactions involved. Figure (1.3) shows the Cox and Cole generalized mechanism for the autoignition of a hydrocarbon with a carbon number of $\geq$ 4.

The Cox and Cole model has been appraised, in the work of this thesis, in terms of the featured hydroperoxyalkyl radical reactivity. This appraisal was based on a kinetic study of a representative member of this radical type that used the pulse radiolysis/kinetic absorption technique[41].

(1.5) FINAL REMARKS

This study aims then to investigate the behaviour of a range of ignition improving materials, including 2-^{n}butoxyethyl nitrate, 2-methoxyethyl nitrate, di-^{t}butyl peroxide and ^{i}propyl nitrate, mainly from the low temperature flow reactor pyrolyses of these materials. The flow reactor was specifically built and validated for this purpose and resembles a reactor of Kershenbaum and Leaney[42,43]. These pyrolyses allowed both the decomposition kinetics of the above ignition improvers to be measured and the chemistries of the initial pyrolyte alkoxy radical fragments to be investigated, to respectively provide a physical and chemical basis for understanding the empirical, ranked performances of these materials.

Figure (1.3) Generalized mechanism for the autoignition of hydrocarbons, with carbon numbers > 4, at temperatures up to about 850K.

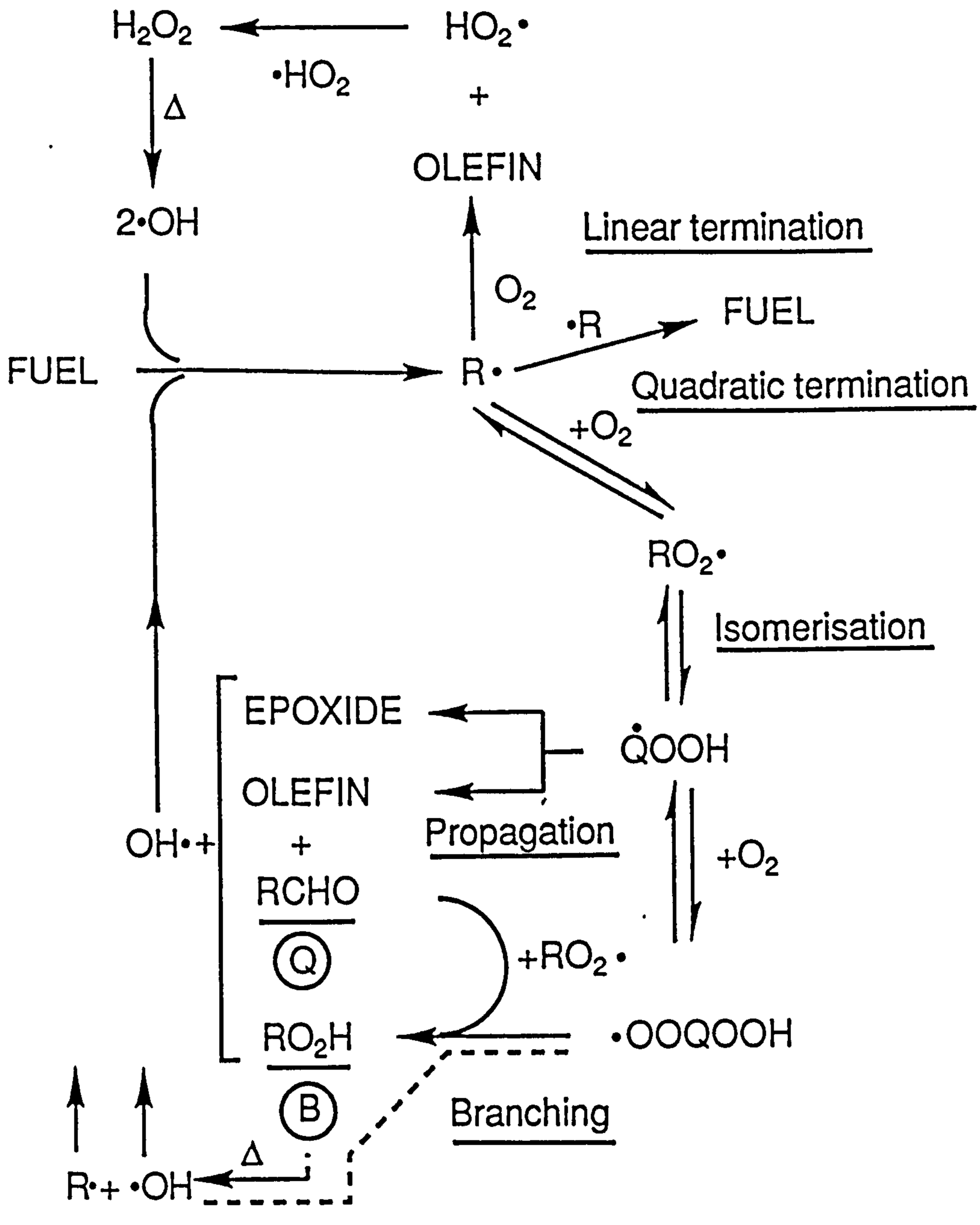

As mentioned earlier, an autoignition study of nitrogen dioxide as an ignition improver, that is analogous to the nitrate and peroxide studies of Kirsch and Selby, has also been performed, and allows a full comparison between the above nitrate and peroxide ignition improvers.

Additionally a spectrokinetic study of a hydroperoxyalkyl radical, the α–hydroperoxyisobutyl radical, has been undertaken to investigate the behaviour of this radical as an autoignition intermediate, and, retrospectively, to support our understanding of ignition improvers.

CHAPTER 2 EXPERIMENTAL METHODS

(2.1) THE PLUG FLOW REACTOR

(2.1.1) General description of the reactor

We have built a linear flow reactor specifically for the purpose of studying the low temperature pyrolyses of a variety of ignition improvers at high inert gas dilution. The flow technique was deemed desirable for this purpose owing to its steady state nature, where the pyrolysis chemistry can be temporarily resolved on a convenient second time scale along an axis.

In general the design of flow reactors aims at creating an environment where a chemistry can be studied free from any heat or mass transfer limitations. Desirably then the aforementioned axis is free from any temperature gradients and is temporarily resolved solely by the convective gas flow. We have attempted to achieve these ideals in a furnace heated flow tube that contains an independently heated metallic sinter, through which the reactor gases are passed. The sinter is made of 22 micron wide fecralloy (an Fe/Al alloy) fibres that have been pressed into a sheet, and serves as a highly efficient heat transfer medium by virtue of the extensive surface contact it provides with the permeating gases. The sinter was a gift of Shell Research Ltd., where it has found an application in a flat flame burner apparatus[44].

The reactor gases are supplied to the fecralloy sheet divided between the reactants and the main diluent, where the reactants are

directly delivered to the fecralloy surface by a cooled inlet tube and the diluent is furnace preheated. The double advantage of this arrangement is respectively that the reactants are preserved from premature reaction and that the sinter lifetime is extended by the minimization of its energy demands. The aims of the sinter, therefore, are to rapidly heat and turbulently dilute the reactants, and, by virtue of this turbulence, to establish a plug flow throughout the rest of the reactor. The pyrolysis studies can be performed then in this plug flow, that is isothermally maintained against heat losses by an additional furnace heating.

It is necessary, however, to ensure that these ideal conditions are preserved despite a means of sampling the various axially resolved steady reaction states. An intrusive gas cooled probe, that can traverse the central reaction axis, has been chosen for this purpose, and allows a gas sample to be withdrawn from any axial reaction position for chemical analysis. The probe aims to preserve the isothermal plug flow of the reactor both convectively, by sampling this flow at its indigineous linear rate, and thermally, by its judicious cooling action. The latter is achieved through the ability of the probe to sample, additionally, the axial temperature profile of the plug flow by means of a centrally positioned thermocouple, that can move independently of the probe itself. It is therefore possible to explore, and isothermally optimize, the temperature profile of the plug flow along the central reaction axis, by varying the balance between the fecralloy and furnace heating.

Finally, the flow reactor has been constructed using a wide bore quartz tube, with a small surface to volume ratio, to minimize the possibility of any heterogenous chemistry.

(2.1.2) Detailed description of the reactor

The flow reactor is constructed around a quartz flow tube, F, (H. Baumbach Ltd.) 86 cm long x 8.6 cm bore, that is horizontally mounted within a radiation furnace and is shown in figure (2.1). A 40 cm long quartz preheating tube, P, (H. Baumbach Ltd.) covered at one end by the fecralloy sinter, FS, is inserted, by this end, into the upstream end of the flow tube. The upstream end of the preheating tube, and downstream end of the flow tube, are both mounted and sealed in bench fixed stainless steel flanges, F1 and F2, and, additionally, these two tubes are connected by a similar "floating flange", F3, just outside the furnace. Flanges F2 and F3 are shown in figure (2.2), where the mechanism employed for sealing the reactor is clearly indicated. The flow tube locates into flanges F2 and F3 and the preheating tube passes completely through flange F3, where, in each case, a vacuum tight seal is made on compressing a silicone O ring around the entire tube circumference. The O ring is sited in a recess of the flange and is compressed by the movement of an annular plate towards the flange body. This is achieved on tightening six screws that pass evenly through the plate and into the flange. Flange F2 is bored to allow the passage of a movable sampling probe that is sealed in the flange by two press fitting silicone O rings. Flange F2 is, additionally, water cooled, to preserve the silicone O rings and possesses a protective pressure relief valve, that opens just in excess of 1 bar absolute flow tube pressure, and also a port that connects to a pressure measuring device. Flange F1 is similar to flange F2 except flange F1 passes the inlet tube rather than the sampling probe and possessses none of the additional features of flange F2. Flange F3, like flange F2, contains a pressure measuring

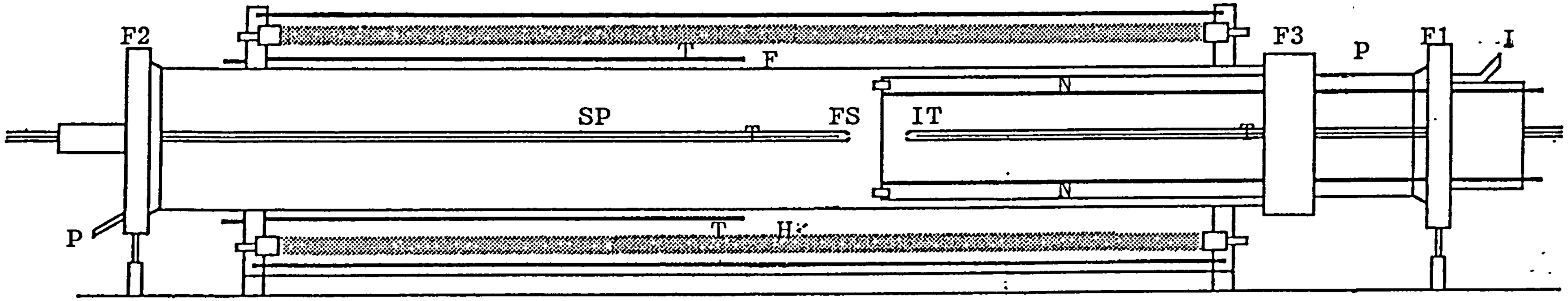

Key: F = Flow tube F1-3 = Flanges FS = Fecralloy sheet H = Furnace heater
I = Main gas inlet IT = Inlet tube N = Nickel rods SP = Sampling probe
T = Thermocouples

Figure (2.1) The reactor / furnace assembly.

Figure (2.2) (a) The fixed downstream flange and (b) the "floating flange".

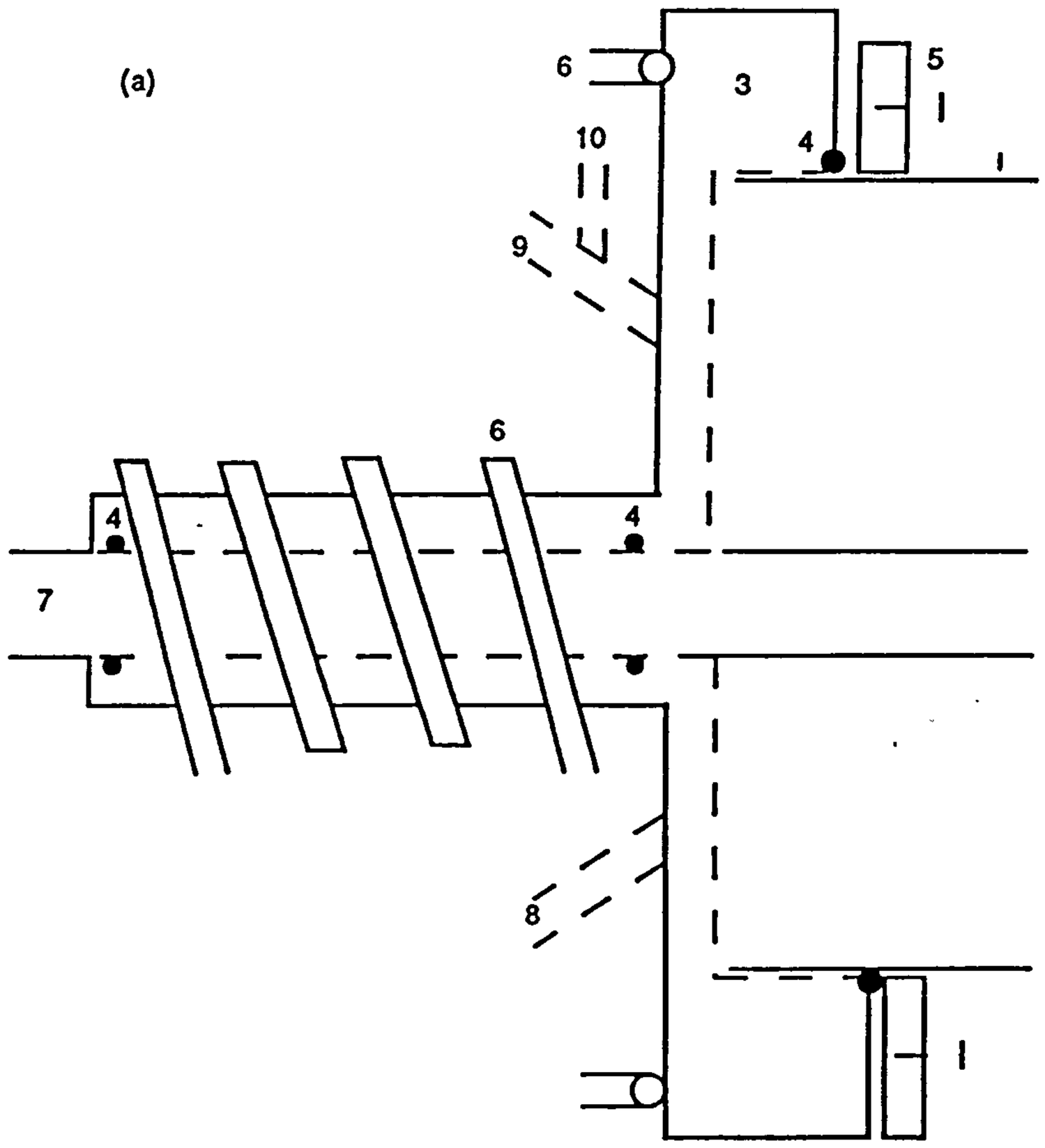

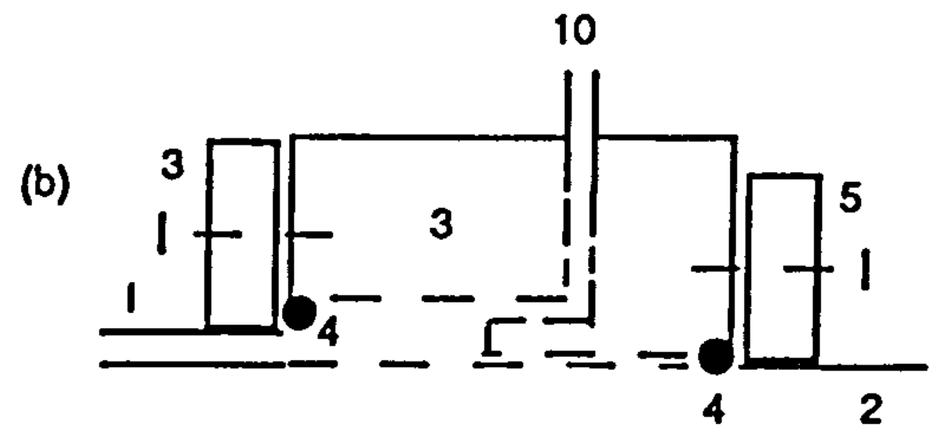

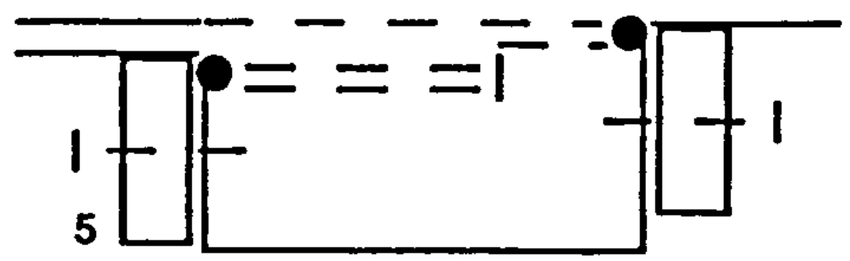

1 = Flow tube, 2 = Preheating tube, 3 = Flange body, 4 = Silicone O ring, 5 = Annular plate, 6 = Copper coils, 7 = Sampling probe, 8 = To pump, 9 = To pressure relief valve, 10 = Pressure port.

port. Flanges F1 and F3 are shown in photograph (2.1) together with the assembled preheating and inlet tubes.

The flow reactor is separately supplied with the reactant and diluent gases, which, in the latter case, are admitted to the preheating tube through the inlet, I, where they are furnace preheated. The reactant gases, however, are mainly heated by the fecralloy sheet, where, subsequently, the temperature of the flowing and diluted reactant mixture is furnace maintained.

The furnace consists of an enclosed ring of six infra-red heaters, H, (Sun Lighthouse Ltd.) that are evenly spaced around the flow tube at a fixed distance from its surface of ca. 4 cm. The arrangement is enclosed by an evacuated, circular, stainless steel jacket that, together with the heaters, is mounted between a pair of opposed sindanyo face plates (A.C.D. Ltd.).

The power supply to the furnace is thyristor controlled, with a manually supplied set point, and employs a thermal feedback mechanism. This mechanism operates by the thyristor taking an input signal that represents the difference between the set point and the output signal of a type K thermocouple (Minta Ltd.) that is in contact with the flow tube wall. Additionally, the radiation heaters are supplied in three pairs, where the heaters of each pair have equivalent vertical positions and are in series with a rheostat (Claude-Lyons Ltd.). The purpose of this arrangement is to preferentially heat the bottom rather than the top of the furnace, to counter the effect of convection in the large, otherwise stagnent, furnace cavity. This is achieved by adjusting the three rheostats until the wall temperatures around the middle of the post fecralloy heated flow tube, that are measured by an even circular distribution of six type K thermocouples, are all isothermal. The temperatures recorded

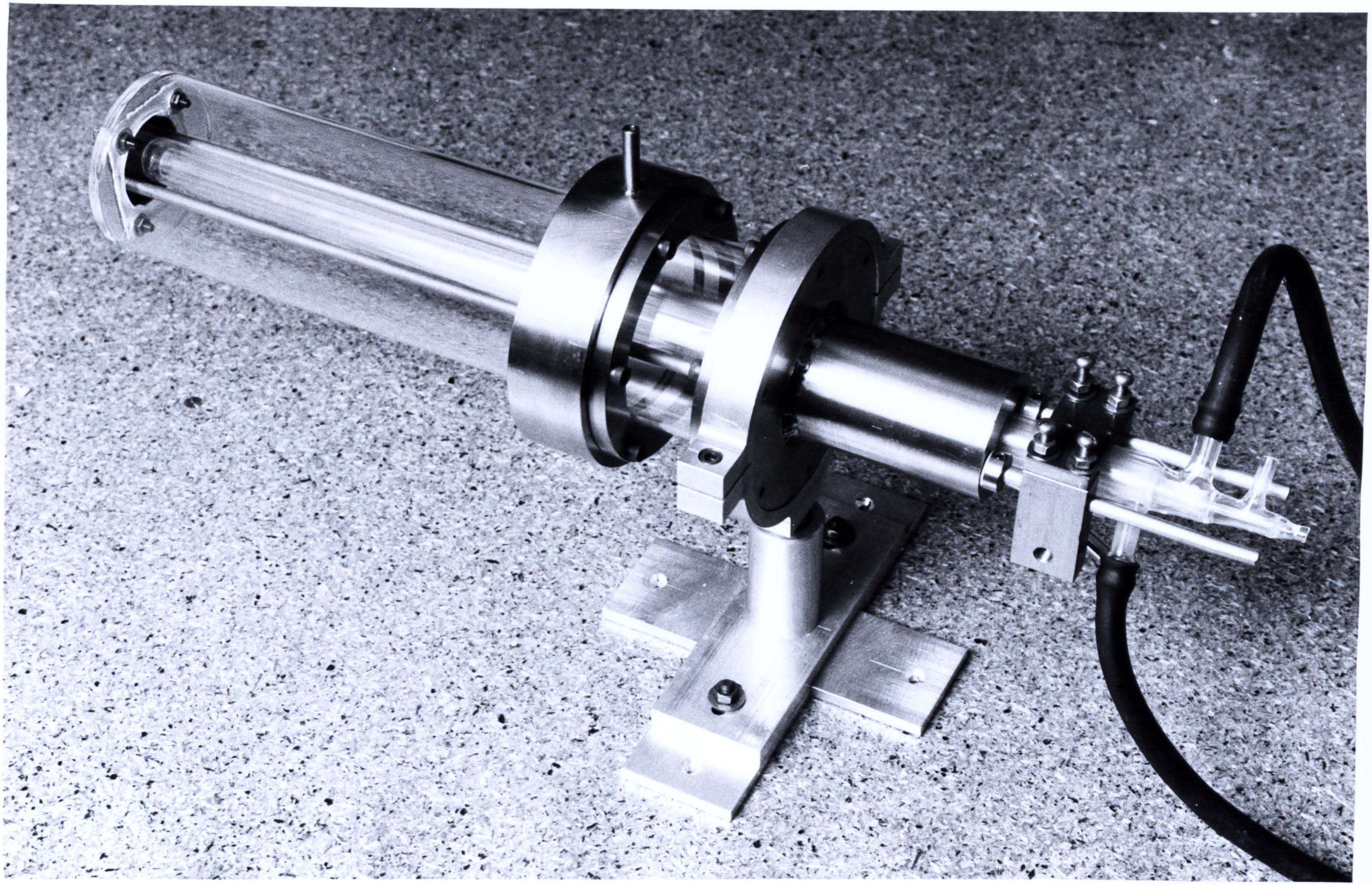

Photograph (2.1)

by these thermocouples are digitally displayed (Farnell Ltd. DTT2) using an appropriate power supply (Farnell Ltd. D5–5A). The total power of the radiation furnace is 7.5 kW and the reactor is protected from accidental overheating by a thermal switch.

The reactant gases are introduced directly onto the upstream surface of the heated fecralloy sheet by means of a gas cooled quartz inlet tube, I, that passes through flange F1. The inlet tube is shown in figure (2.3a) and is constructed from four concentric tubes (H. Baumbach Ltd.), where an inner tube carries the reactants and is surrounded by two outer tubes that carry a coolant. The coolant is supplied by a rotary vane air compressor (Gast Manufacturing Corporation, model 1022, free air flow 235 dm^3 min^{-1}) at a rotameter set flow rate (Platon Flowbits Ltd., 2–25 standard dm^3 min^{-1}). Additionally, a fourth tube, that inserts inside the reactant tube, serves as a jacket for a movable type K thermocouple. The temperature of the reactant gases can thereby be measured along the entire length of the inlet tube and is digitally displayed as before. To ensure that the inlet tube fits through flange F1, the outermost concentric tube is centreless ground to have a uniform outside diameter across its length of 19.95 mm. The inlet tube then clears flange F1 by only 0.05 mm, where it is doubly sealed by two press fitting silicone O rings that are partially recessed into the flange body.

The fecralloy sheet is mounted on the upstream end of the preheating tube in an arrangement that allows for an electrical heating of the sinter and that is shown both in figure (2.3b) and in photograph (2.2). Essentially the mounting is achieved by the passage of a squared configuration of four nutted screws through the fecralloy sheet, its contacts and the holed flange. The fecralloy sheet is similarly squared, to ensure a good electrical conduction, and its

Figure (2.3) The (a) inlet tube and the (b) fecralloy mounting.

(a)

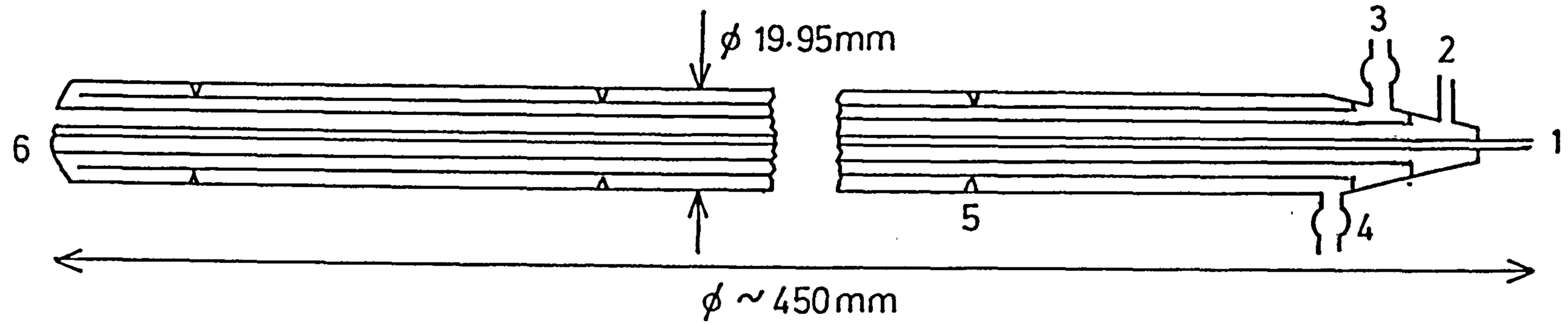

1 = Thermocouple probe, 2 = Reactant entrance, 3 = Coolant entrance, 4 = Coolant exit, 5 = Pintle, 6 = Tie.

(b)

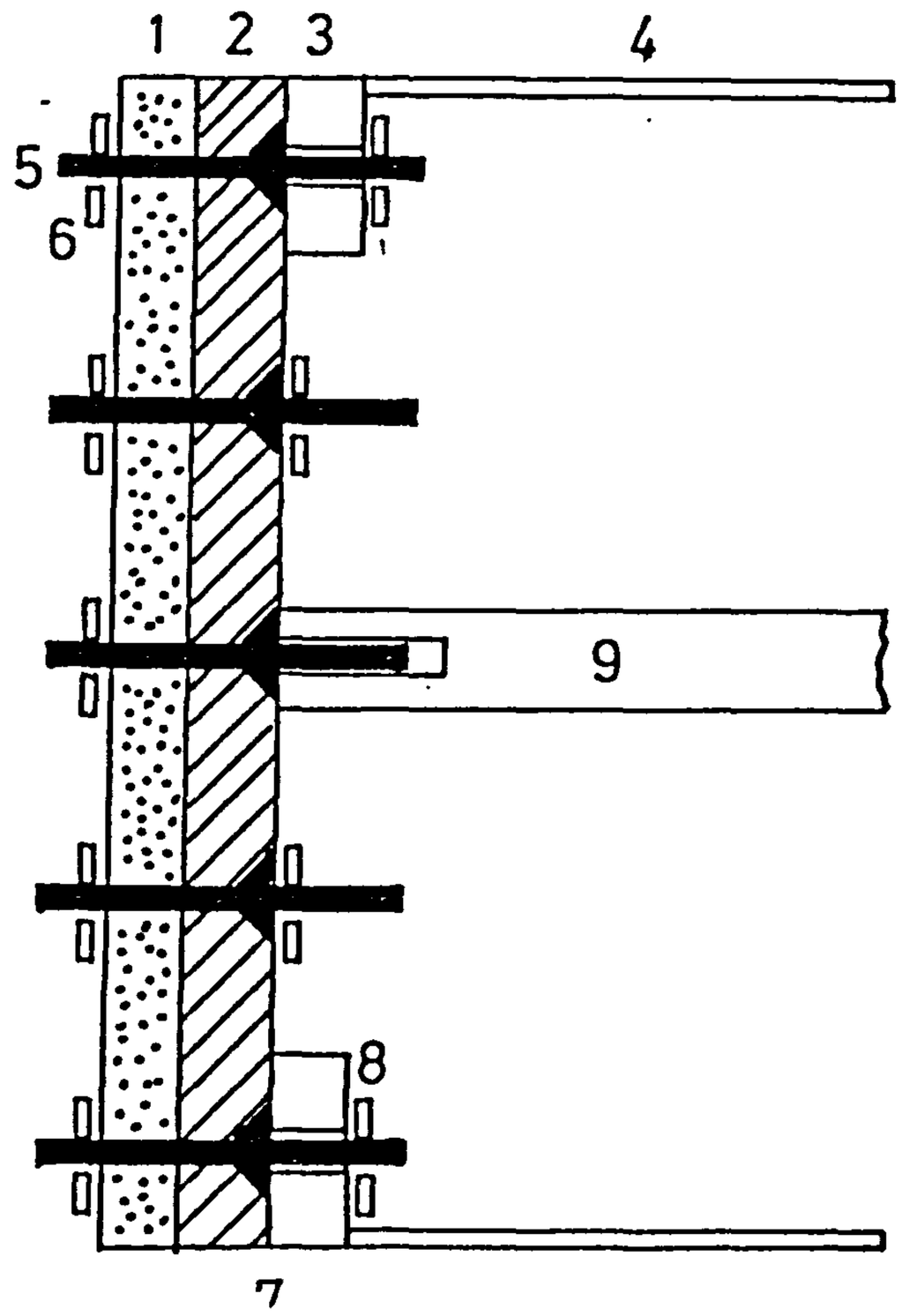

1 = Copper contact,
2 = Fecralloy sheet,
3 = Quartz flange,
4 = Quartz preheating tube,
5 = Stainless steel screws,
6 = Stainless steel nuts,
7 = Kaowool pad,
8 = P.T.F.E. washer,
9 = Nickel rod,

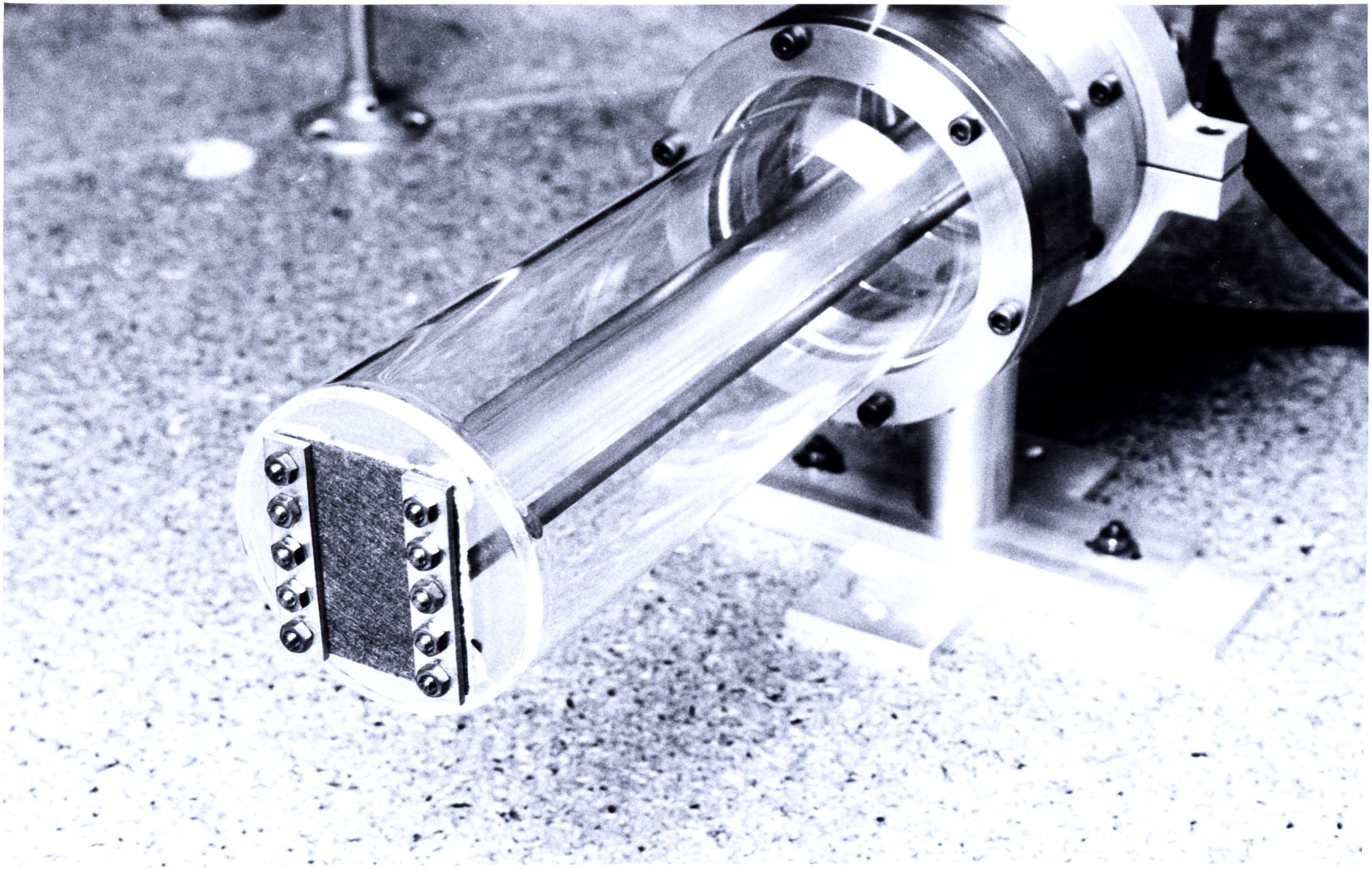

Photograph (2.2)

electrical contacts run inside two opposed edges of the sheet. The fecralloy sheet is mounted directly onto the upstream surface of the flange, where it forms a press fitting seal, leaving the electrical contacts to be made on the upstream surface of the sheet by two copper strips. The fecralloy sheet is supplied by a 13A variac, the output of which is stepped down by a 1.6 kVA transformer (F. Vowles Ltd.) to provide a high current supply that minimizes contact resistance problems. The fecralloy sheet contacts are connected to the transformer terminals by two nickel rods.

The reactor gases are sampled from the flow tube by a movable quartz probe. The probe is of an identical construction to the inlet tube and passes through flange F2 with an analogous fit and sealage to that of the inlet tube in flange F1. The probe then is thermocoupled, by a type K theromocouple, to measure the sample temperature throughout, and air cooled, in accordance with this measurement, to ensure that the sample is removed without any further reaction. The temperature measured by this thermocouple is also digitally displayed as before. The probe is mounted on a motorised drive and can traverse the centre axis of the flow tube up to the fecralloy sheet. Photograph (2.3), like figure (2.1), also shows the furnace/reactor assembly, and, particularly, reveals the flanging and sampling mechanism of the reactor.

The flow rates of the reactor gases are set by mass flow controllers (A.F.C. 260 A.S.M. Ltd.) that are powered and take their set points from a six channel read out box (A.S.M. Ltd.). A bulk flow rate and absolute pressure of, respectively, the order cm s^{-1} and 1 bar can be stabilized in the flow tube by a carefully throttled downstream pumping of the tube by an oil rotary pump (Edwards ED5O). The pump is throttled by an on–off Saunder's valve in

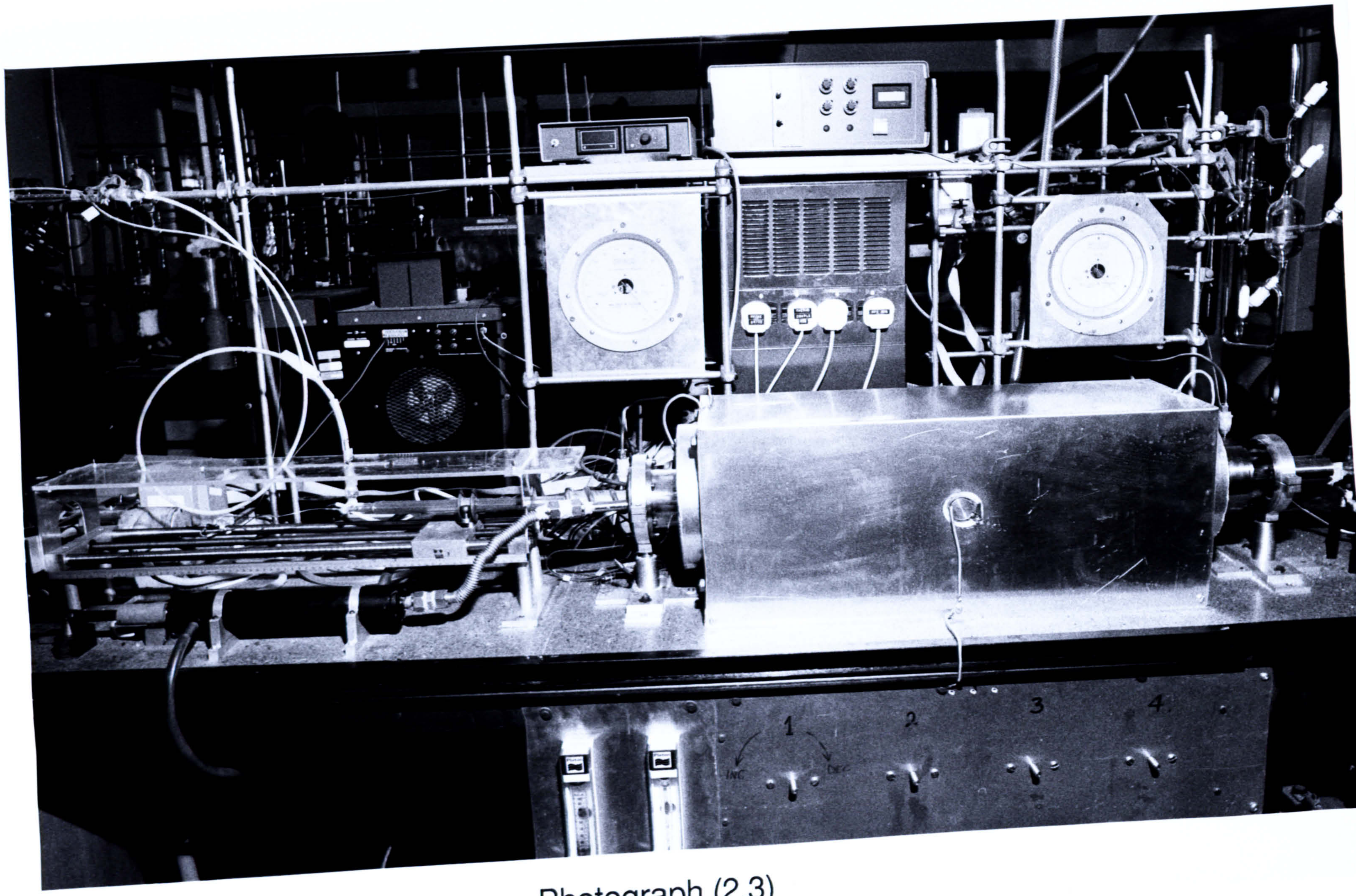

Photograph (2.3)

parallel with a calibrated needle valve (Edwards LV5). The reactor exhaust is passed through a heat exchanger on immediately exiting the flow tube. The pump then receives a cooled exhaust and expels these gases to an outdoor area.

The pressure at each end of the flow tube is monitored by an aneroid Wallace and Tiernan gauge that is calibrated over the range 0–800 torr. The pressure gauges are connected to the reactor, as mentioned earlier, by means of ports in flanges F2 and F3.

(2.1.3) The inlet system.

The flow reactor is introduced to the reactant gases using the inlet system shown in figure (2.4a). The introduction of a reactant that is a room temperature liquid is achieved using a bubbler that contains this reactant and that is connected to a mass flow controlled gas supply. The supply gas is bubbled through the liquid reactant, via an immersed sintered thimble that breaks this gas into fine bubbles, and the bubbler effluent is subsequently scrubbed and then transferred to the reactor. The scrubbing is achieved by passing the effluent through a glass wool containing U–tube that removes any contained droplets and the reactor is thereby supplied with the reactant vapour pressure, at the bubbler temperature, in the supply gas. The bubbler is immersed in a cold ice bath to ensure an even delivery of the reactant over a period of time and the supply gas is provided by either the main reactor gas or oxygen. Exceptionally, for studies that employ two reactants that are room temperature liquids, two bubbler systems are operated in parallel and their respective effluent gases, both after scrubbing, are premixed in a vessel before their admittance to the reactor. In either case the

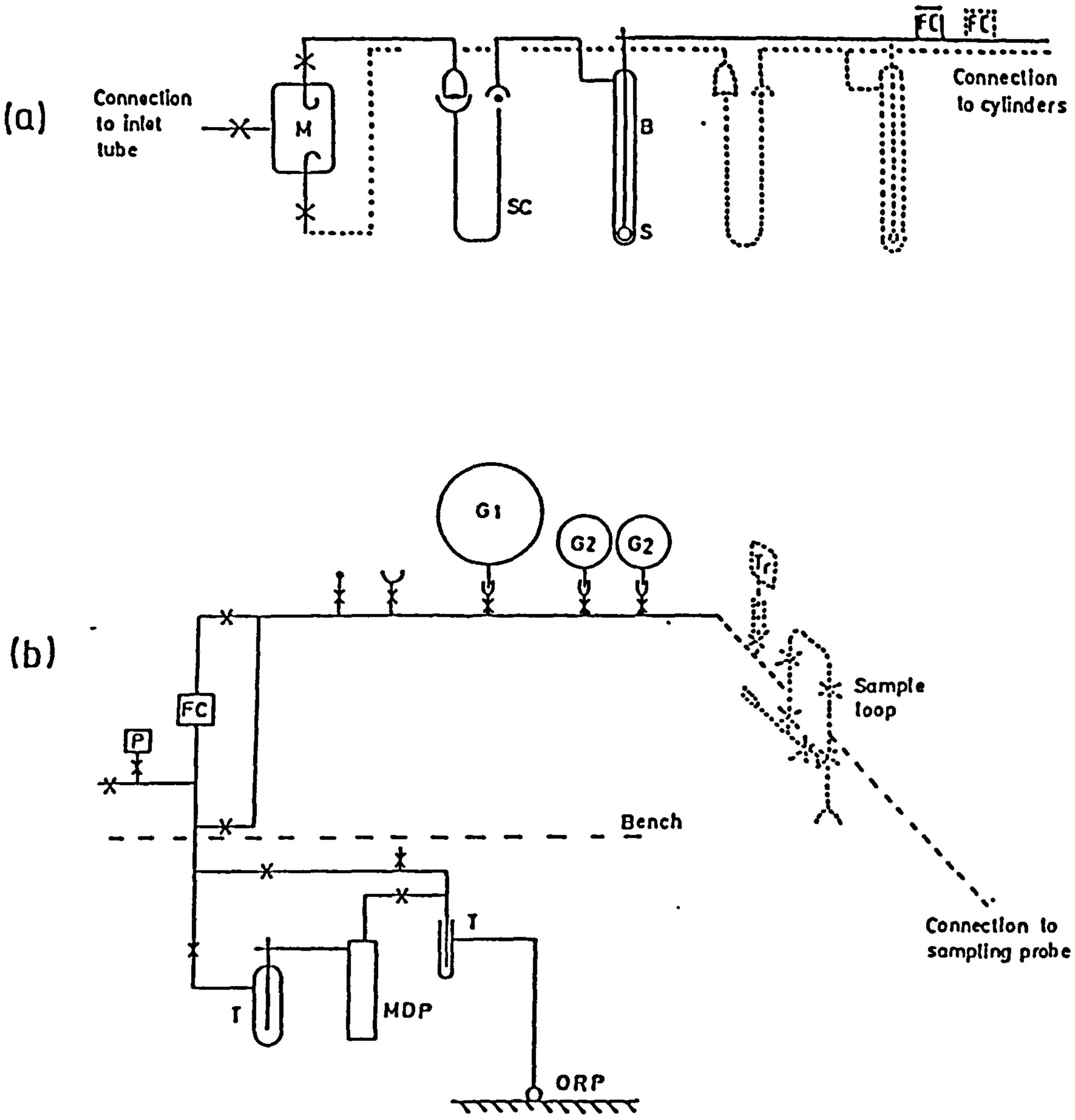

ORP = Oil rotary pump
T = Trap
MDP = Mercury diffusion pump
P = Pirani gauge
FC = Flow controller
G1 = 4dm^3 globe
G2 = 1dm^3 globe
Tr = Pressure transducer
M = Mixing vessel
B = Bubbler
S = Sintered thimble
Sc = Scrubber.

Youngs fittings

X	= SPOR	6	
+	= POR	6 RA	
X	= SPOR	15	
+	= POR	15 RA	
Y	= GBM	12/5	
	= GBF	12/5	Ball joints
Y	= GBM	28/12	
	= GBF	28/12	
Y	= ORS	10	Tapered joints
	= ORS	7	

Figure (2.4) The (a) inlet system and (b) the sampling / analysis line.

reactant gases are transferred from the mixing vessel to the inlet tube by nylon tube.

(2.1.4) The sampling and analysis system.

The sampling system is shown in figure (2.4b) and enables a gas sample to be removed from the flow tube and subsequently analysed by gas chromatography (Perkin Elmer PU4500 F.I.D. detection). The gas sample is continuously withdrawn from the reactor using the movable probe under the action of an oil rotary pump that is throttled by a further mass flow controller. The sampling is exactly throttled to occur at the bulk linear flow rate and transfers a gas sample to the sampling system, via a flexible nylon tube coil, through the sample loop of the gas chromatograph (g.c.) and subsequently to the pump.

The gas chromatographic analysis of the reactor gas is performed using a system that is respectively apriori understood for its separation characteristics and apostpriori calibrated. These pre and post-requisites require the gas chromatographic analysis of a variety of gaseous standards that are, formerly, the suspected components and, latterly, the known components of the reactor gas mixtures.

These gaseous standards are analysed after their presentation to the sampling and analysis system under evacuated conditions. This system is evacuated up to and including the sampling loop by a pumping arrangement that consists of an oil rotary pump (Edwards ES35) and a two stage mercury diffusion pump that is isolated on its high and low vacuum sides by a pair of liquid nitrogen maintained cold traps (77K). The rotary pump serves to back the diffusion pump, in a combination that respectively provides a soft and a hard

evacuation of this system, where the traps both protect the pumps from the removed gases and contain any mercury vapour that escapes from the diffusion pump. To improve the pumping speed of this system, the sampling line is warmed to ca. 50°C by a heated exterior winding of nichrome wire that is supplied by a 13A variac. The vacuum achieved by this system is measured at a remote site from the pumps, using a pirani head (Edwards PRE 10K) and gauge (Edwards 501) combination, where it can reach 10^{-3} mb. The standards are admitted to this evacuated sampling and analysis system both via ports in the sampling line and according to the room temperature state of the standard. Accordingly, the gaseous standards are directly admitted whereas the liquid standards are degassed, to remove the dissolute air, and are then admitted as their vapour pressures.

The liquid standard is contained in a ported glass bulb, where it is degassed by a series of freeze–pump–thaw cycles. In the first of these cycles, the standard is initially chilled by a brief immersion in liquid nitrogen and then exposed to the pumped sampling system where it is subsequently frozen with maintained exposure. The standard is next isolated from the pumped sampling system and allowed to thaw to room temperature, where the majority of dissolute air is degassed in vacuo. The amount of degassed air can be measured by the pirani head and gauge combination on isolating the evacuated sampling system from the pumping arrangement and by then exposing this isolated system to the standard. The freeze–pump–thaw cycle is repeated, without intially chilling the standard, until the pirani measurement indicates that the standard is thoroughly degassed. This usually requires three cycles.

As mentioned earlier, the purposes of these standard analyses is

either to establish the separation characteristics of a chromatographic system or to calibrate such a system for a particular analyte. In the former case, the standards are analysed as neat gases and can be admitted to the sample loop of the gas chromatography system at known pressures that are measured by a strain gauge pressure transducer (Transamerica Inc.) and are digitally displayed (Transamerica Inc.). In the latter case, the standards are analysed in a nitrogen diluent, rather than as neat gases, to increase both the flexibility of the quantitative analysis and, thereby, the accuracy of the calibration. These latter standard mixtures are made in ported globes, where the standards are admitted at measured pressures and are then diluted by a ported supply of nitrogen diluent to a measured total pressure. The standard mixtures are subsequently allowed > 20 minutes to achieve an even mix, prior to analysis. These standard mixtures can also be diluted, if desired, by an analogous procedure.

The gas chromatography systems that have been used in the work of this thesis are discussed in Chapter 3. Finally photograph (2.4) shows a broad view of the flow reactor, including the inlet, sampling and analysis systems.

(2.1.5) Characterization of the flow reactor.

As a prerequisite to using the flow reactor for any new kinetic studies, it was necessary to confirm the desired isothermal and plug flow ideals throughout the reaction space.

Initially the operated reactor was thermally investigated to characterize the temperature distribution of the reactor gas across the reaction axis. Accordingly the reactor was representatively operated

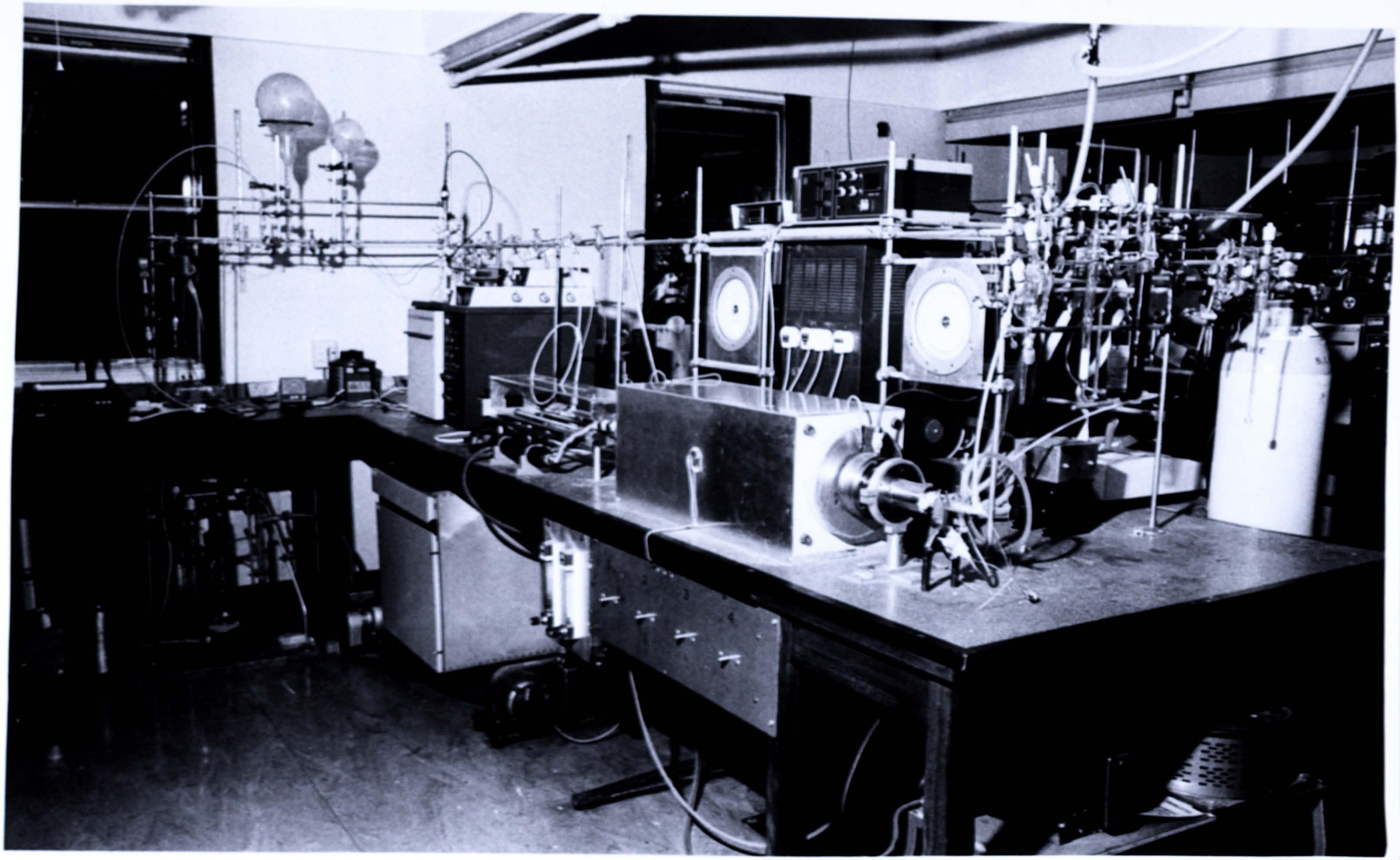

Photograph (2.4)

at a temperature of ~ 500K and at a bulk linear flow rate of ~ 0.5 cm s^{-1} of nitrogen. As mentioned in the general description of the reactor, the sampling probe carries an independently moving thermocouple and allows a temperature measurement anywhere between the downstream surface of the fecralloy sheet and the sampling probe tip. The temperature distribution between these extremities is affected certainly by the balance between the fecralloy and furnace heatings, as noted in the general description of the reactor, and possibly by the cooled sampling probe. To simply explore this temperature distribution, the above two, and opposing, effects thereon were resolved by a far downstream siting of the cooled sampling probe in the flow tube. In this situation, the movable thermocouple was positioned to be axially equivalent with the flow tube wall-contacting thermocouples and the balance between the furnace and fecralloy heating was adjusted so that these thermocouples all recorded an isothermal temperature of ~ 500K. In this condition, the temperature distribution across the reaction axis could be explored to investigate the possible effect thereon of only the cooled sampling probe. The sampling probe was cooled so that the tip temperature was nominally 20K lower than the above isothermal temperatures, where the probe sampling is expected to quench the isothermal pyrolyses of the ignition improvers, and the aforementioned exploration showed that the sampling probe cooled the upstream gas across the reaction axis by a logarithmically decreasing amount that extended for about 5 cm from the probe tip.

The sampling probe shortfalls the original ideal of maintaining isothermality across the reaction axis then with implications that concern the anticipated use of the flow reactor. Accordingly, the pyrolyses of the ignition improvers occur both at isothermal and

exponentially decreasing temperatures across the reaction axis, and the kinetics of these processes, therefore, can only be freely studied from this non ideal under first order conditions. The first order rate equation that expresses the fractional removal of a pyrolyte, a/a_o, where a and a_o are respectively the sampled and initial pyrolyte concentrations, between the upstream surface of the fecralloy sheet and the probe tip is given by the following expression, where k and k' respectively represent the isothermal and exponentially decreasing rate constants and where t and t' are the corresponding reaction times.

$$a = a_o \exp(-kt) \int \exp(-k't') dt'$$

This equation implies that the first order pyrolysis kinetics of an ignition improver can be conveniently measured by varying the total reaction time, where the following simplified rate expression applies.

$$a = \text{const.} \exp(-kt)$$

Finally, this expression is only valid if the relative pyrolyte concentrations are all measured after a partial pyrolysis at the isothermal temperature. The second implication concerning the sampling probe then is that the reactor gas can only be sampled at or beyond ~ 5 cm, measured downstream from the fecralloy sheet, of the reaction axis.

Subsequently, the flow character of the reactor was investigated in distribution experiments, under the previously stated operating conditions, where a trace amount of methane was introduced, via the inlet tube, into the reactor's main nitrogen flow with a subsequent probe sampling along the flow tube axis. These experiments showed the methane to rapidly achieve an homogeneous distribution in the reactor, even in close proximity to the fecralloy sheet. The

implication of this finding is that the apparent flow behaviour of the reactor is ideal, although it is not identified whether this is of a plug, as desired, or stirred character. To resolve this uncertainty, the methane was replaced by a chemical reactant. In these experiments then, the temporal variation of the reactant concentration reflects its loss by reaction, which was investigated by independently varying both the sampling position, to test for plug flow, and the flow rate, to test for stirred flow.

Accordingly, the pyrolysis of di-^{t}butyl peroxide ($Me_3CO_2CMe_3$) was chosen for this purpose, owing to both its simplicity and to the large number of previous studies[12]. This pyrolysis proceeds by the rate determining decomposition of the parent peroxide followed by the faster decomposition of the ^{t}butoxy radical. In the presence of oxygen, the methyl radicals that are produced in the latter decomposition are essentially terminated by oxygenation to their peroxy analogues. The simplicity of this pyrolysis arises then

$$Me_3CO_2CMe_3 \longrightarrow Me_3CO\cdot + Me_3CO\cdot$$

$$Me_3CO\cdot \longrightarrow Me_2CO + Me\cdot$$

$$Me\cdot + O_2 \longrightarrow MeO_2\cdot$$

from the presence of oxygen, which ensures that both the peroxide decomposition and acetone formation occur by first order kinetics, that are already of desired notability, as represented below, where k_d is the first order decomposition rate constant of the peroxide.

$$\log_{10}[Me_3CO_2CMe_3]_t = \frac{-k_d t}{2.3} + \text{constant}$$

$$\log_{10}\left[1-\frac{[Me_2CO]_t}{[Me_2CO]_\infty}\right] = \frac{-k_d t}{2.3} + \text{constant}$$

The pyrolysis of 0.55 mb di-^{t}butyl peroxide in 1 bar of a 5% mixture of oxygen in nitrogen was therefore appropriated to the aforementioned characterization experiments, where the effects of independently varying the sampling position and the flow rate were investigated. These experiments surprisingly found the pyrolysis to be unaffected by the former changes and significantly affected by the latter changes. The implication of this finding is that the reactor flow is appreciably stirred, although a stirred flow treatment of the pyrolysis data was kinetically unsatisfactory. In response to these findings, attempts were made to, at least partially, quench the stirring of the reactor gases. As signficant flow rate variations had failed in this, these experiments were repeated in the flow of a different gas. Helium was chosen for this purpose, where it was hoped that the low molecular weight of this gas would reduce the amount of stirring in the region of the fecralloy sheet, the considered origin of this difficulty.

The pyrolysis experiment was repeated, with the above change, and both the peroxide decay and acetone formation were successfully resolved along the flow tube axis, implying that under these conditions, a plug flow behaviour pertains. To confirm this, the pyrolysis was extended over the temperature range 460–504 K, where the maximum temperature across the reaction axis was always isothermal with the wall temperature.

Figures (2.5) and (2.6) respectively, plot the first order decays and formations of the peroxide and acetone at each temperature of the study. The first order plots for the acetone formation required

Figure (2.5) First order di-^{t}butyl peroxide decompositions in the pyrolysis of 0.55mb di-^{t}butyl peroxide in 47.6mb oxygen and a 1b helium balance.

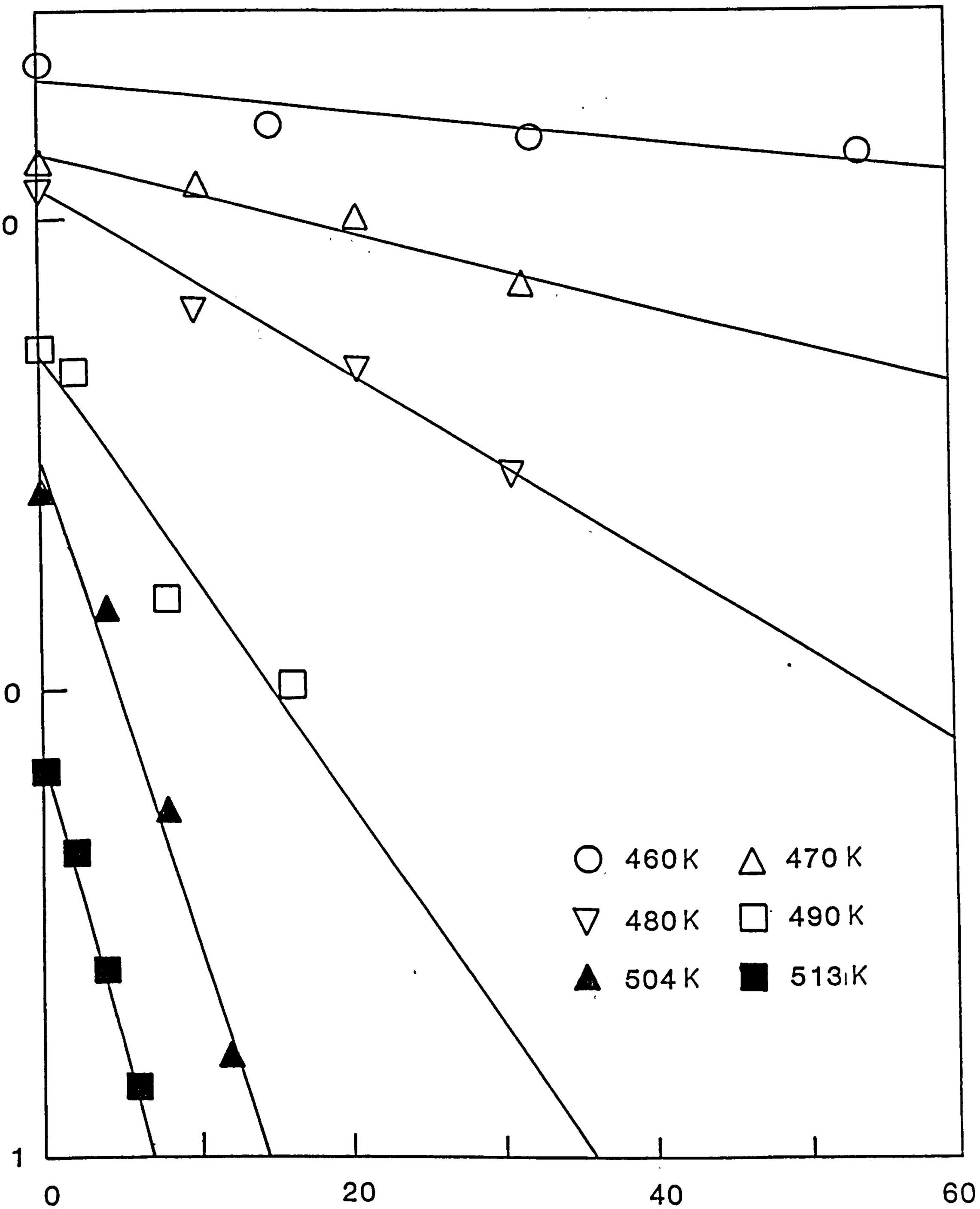

Figure (2.6) First order acetone formations in the pyrolysis of 0.55mb di-^{t}butyl peroxide in 47.6mb oxygen and a 1b helium balance.

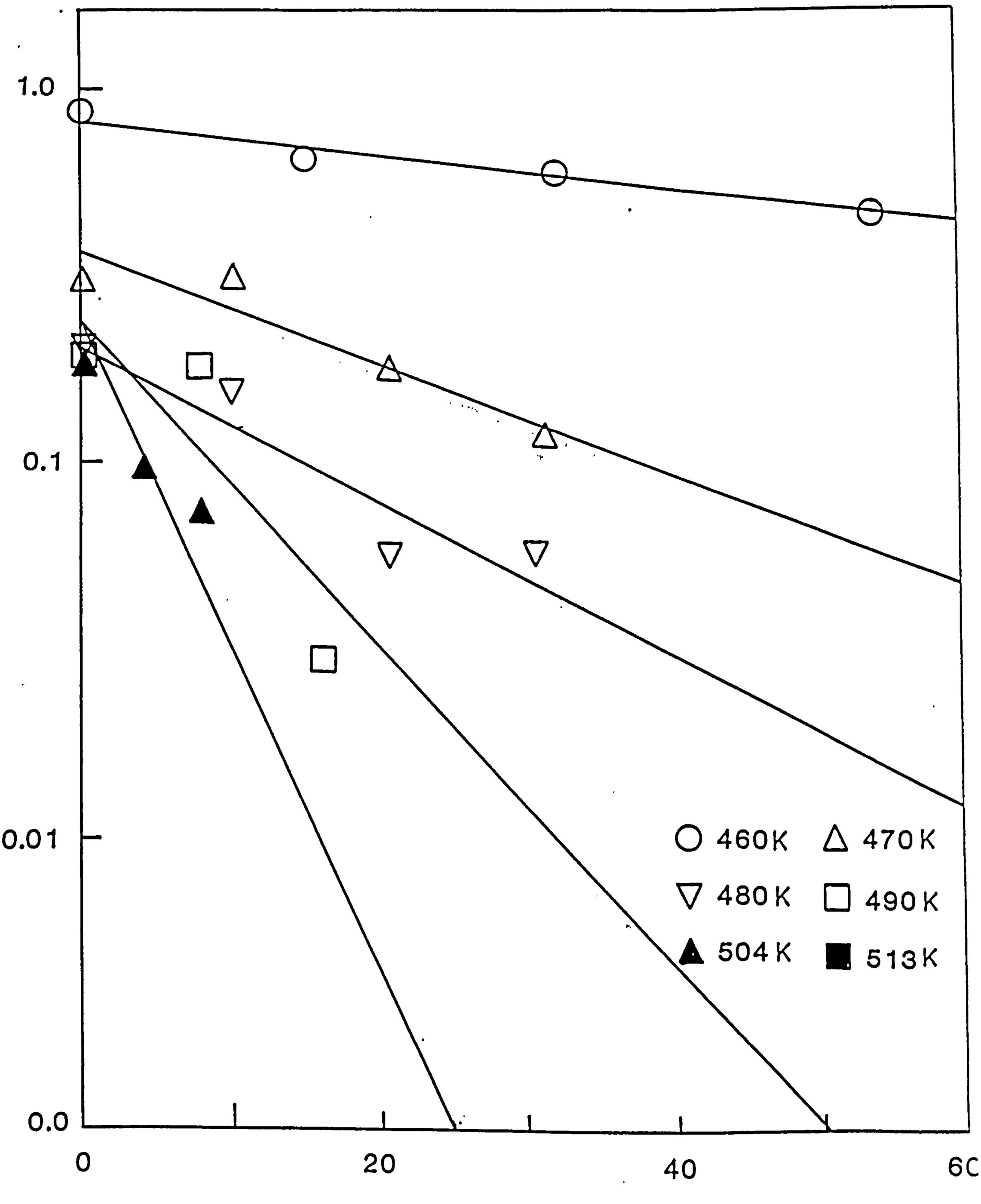

$[Me_2CO]_\infty$ / arbitrary units = 55 at 460K and 60 at other temperatures

each studied temperature, by an extrapolation of the observed acetone yields reciprocally against the residual amounts of the peroxide. These infinite acetone yields varied with temperature, by an effect that is considered to be an experimental artefact, and were not therefore calculated, more simply, from the stoicheiometry of the pyrolysis. It should be noted that this artefact implies a limitation to the use of this reactor to explore mechanisms, by the suggested difficulties of mass balancing a studied process. The slopes of figures (2.5) and (2.6) provide the first order pyrolysis rate constants of the peroxide, that are typically measured to ± 25%. Figure (2.7) is an Arrhenius plot of the first order pyrolysis rate constants against the reciprocal temperature, where (a) the solid line refers to the peroxide decomposition and (b) the broken line refers to the acetone formation, where the highest temperature datum has been omitted. Linear regression analyses of these data respectively gives the following Arrhenius equations for the pyrolysis, where the errors quoted here, and throughout the rest of the thesis, are to two standard deviations.

(a) $\log_{10}(k/s^{-1}) = 15.03 \pm 0.69 - (36.1 \pm 1.5)$ kcal $mol^{-1}/RT \ln 10$

(b) $\log_{10}(k/s^{-1}) = 14.35 \pm 2.12 - (34.6 \pm 4.6)$ kcal $mol^{-1}/RT \ln 10$

The pyrolysis kinetics of di-^{t}butyl peroxide have, as mentioned earlier, been extensively studied. Shaw and Pritchard[12] have re-evaluated much of the available data and recommend the following Arrhenius equation for this process.

$\log_{10}(k/s^{-1}) = 15.80 \pm 0.03 - (37.8 \pm 0.1)$ kcal $mol^{-1}/RT \ln 10$

Clearly then there is good kinetic agreement between the pyrolysis studies performed here and previously, and the position of our flow

Figure (2.7) Arrhenius plot for the pyrolysis of di-^{t}butyl peroxide.

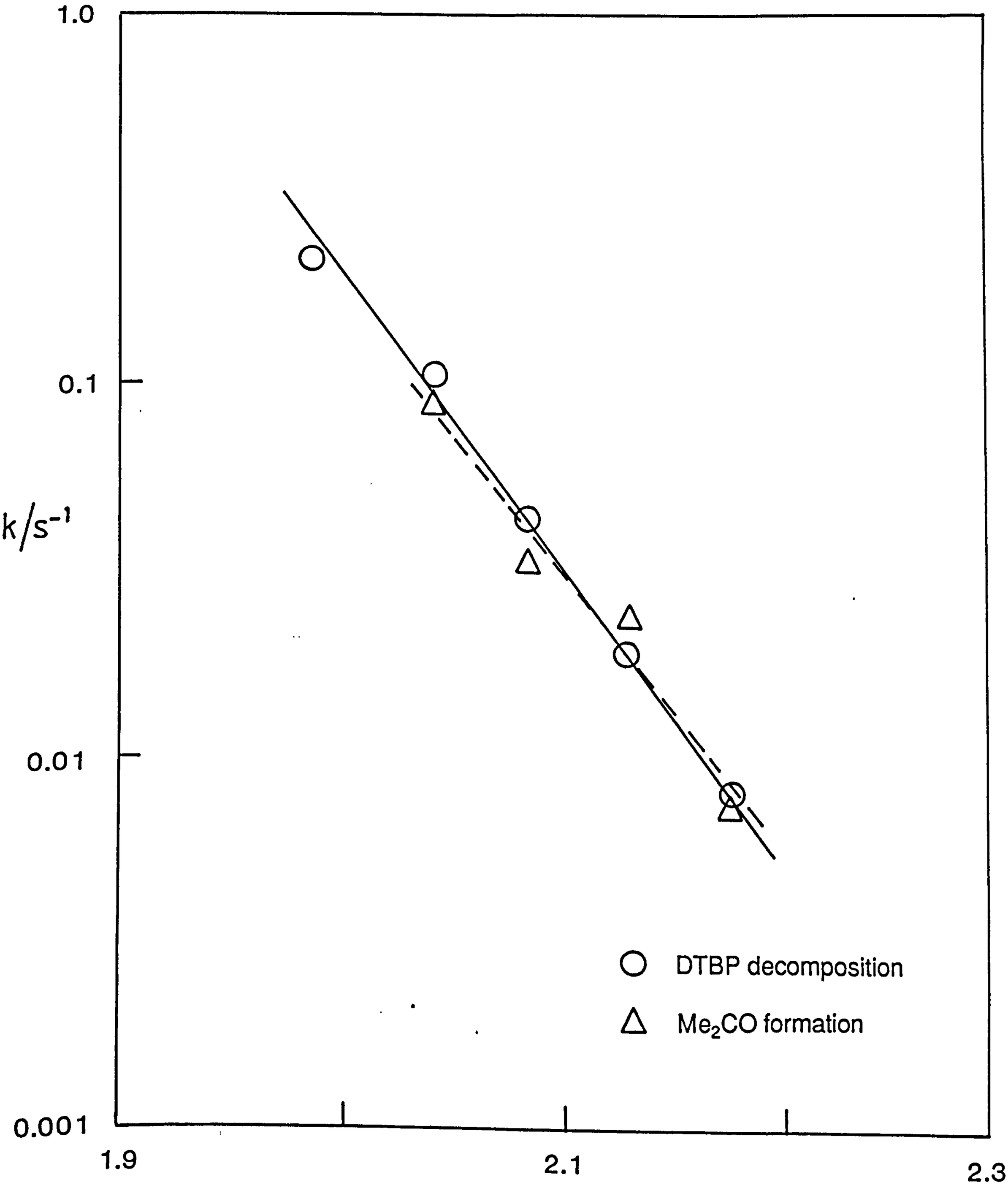

tube study amongst these earlier, mostly static, studies is shown in the Arrhenius plot of figure (2.8).

The pyrolysis of di-^{t}butyl peroxide has therefore successfully established an ideal plug flow performance of our reactor, that can be similarly employed to study the pyrolysis kinetics of a variety of ignition improvers.

(2.2) THE RAPID COMPRESSION MACHINE

The Thornton r.c.m. has been described in detail elsewhere[55] and is shown in figure (2.9).

The r.c.m. rapidly compression heats a gas mixture, by pneumatically driving a pair of opposed pistons together, and the subsequent autoignition process is manometrically followed, with time, up to the autoignition.

Briefly, an evacuated reaction chamber is filled with the desired gaseous precompression mixture. The fuel components of these mixtures are generally injected through a septum capped port of the electrically warmed chamber, where they subsequently evaporate. These mixtures are then compressed by a mechanism that allows the initially withdrawn pistons to be pneumatically armed and locked in this position. This is respectively achieved by applying a high nitrogen pressure to the driving cylinder and by transferring a lesser nitrogen pressure to the hydraulic fluid that fills the hydraulic control chamber.

The r.c.m. is fired by the electronic opening of a solenoid valve that vents a small volume of liquid from the hydraulic control chamber and breaks the hydraulic lock. This causes the pistons to accelerate together, under the driver gas pressure, where the piston

Figure (2.8) Arrhenius plot for the pyrolysis of di-^{t}butyl peroxide, reproduced from Pritchard, and including the data of this study.

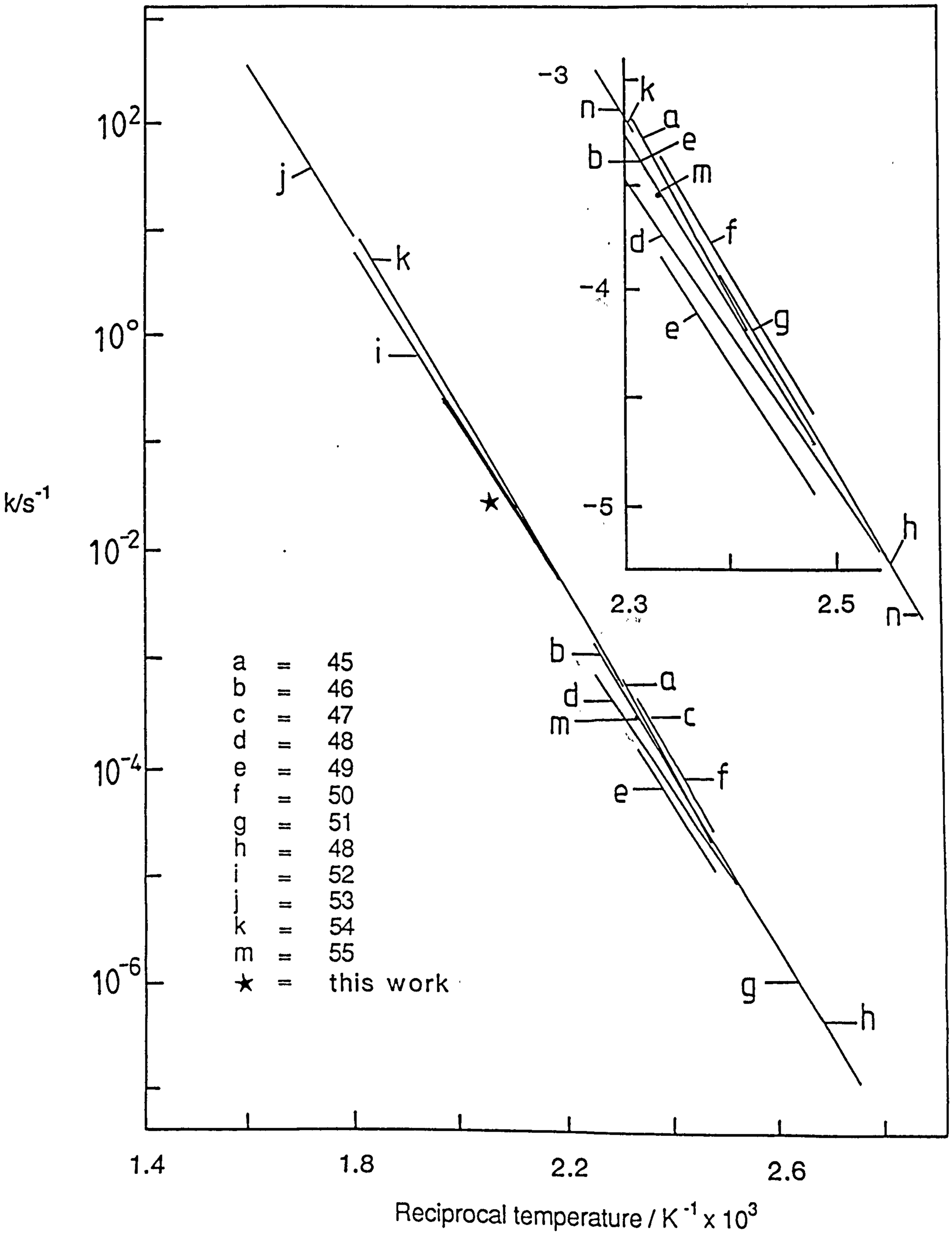

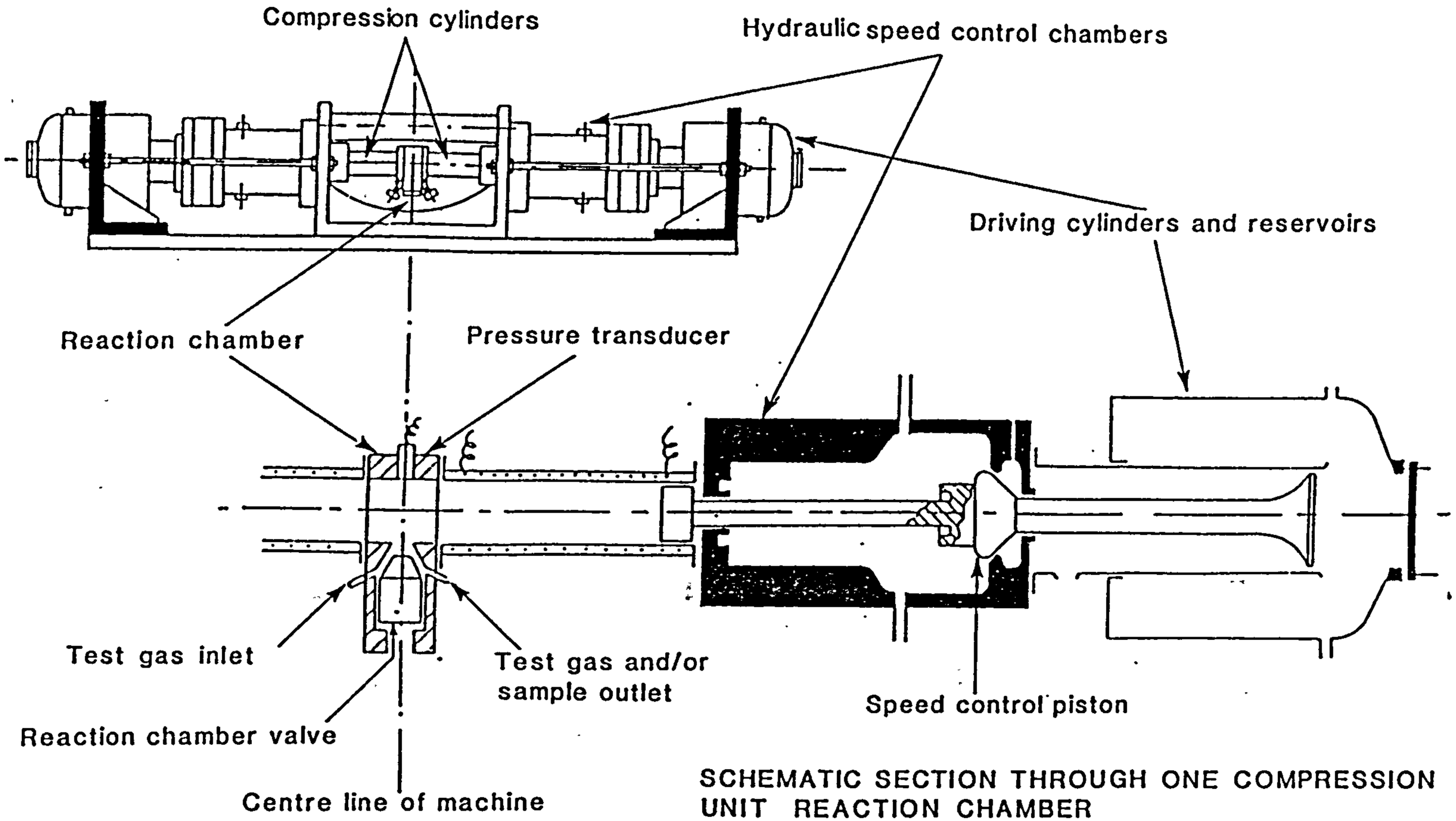

Figure (2.9) The Thornton Rapid Compression Machine.

movement is arranged to be synchronous and to fully compress the gas charge, to a final volume of $\sim$ 45 cm^3, in about 10 ms.

The pressure of the gas charge is measured from the start of the piston movement to the eventual autoignition by a piezoelectric transducer, is displayed on an oscilloscope and can be stored on a minicomputer for subsequent analysis.

The gas charge is compressed to a temperature and pressure that depends primarily on the heat capacity and secondarily on the compressed ratio of the charge. In general, the charge contains an excess of a diluent gas and the end of compression temperature (e.o.c.t.) and pressure (e.o.c.p.) are mainly determined by, and increase in sympathy with, the heat capacity of this gas. This diluent gas is commonly varied between carbon dioxide, to provide a relatively low e.o.c.t. and e.o.c.p., nitrogen and argon, to provide a relatively high e.o.c.t. and e.o.c.p.. The e.o.c.t. is calculated from the e.o.c.p. using the ideal gas law. The compression ratio can be varied in the range 10–7:1. Typically, the compression of a gas charge, at a precompression pressure of 1 bar, can provide an e.o.c.t. that varies between about 600 and 1000K.

Finally, the operating cycle of the machine is completed by independently evacuating the reaction chamber and the driving cylinders, which in the latter case withdraws the pistons, using a pair of oil rotary pumps.

(2.3) THE PULSE RADIOLYSIS/KINETIC ABSORPTION APPARATUS

The Riso pulse radiolysis/kinetic absorption (P.R./K.A.) apparatus has been described in detail elsewhere[56] and is shown in figure (2.10).

Essentially the P.R./K.A. technique is used to create a radical population, by the pulsed irradiation of a suitable gas mixture and allows the subsequent decay kinetics of these radicals, that usually occurs over between 10–100 μs, to be studied by kinetic absorption spectroscopy.

The gas mixture is pulse irradiated by an electron source and the desired radicals are produced either directly from the radiation or indirectly via a chemical sensitizer. A Febetron 705B field emission accelerator provides an intense beam (3000A) of 2MeV electrons with a pulse duration of 30 ns, corresponding to an irradiation energy of 180J/pulse.

The gas mixture is contained in a 1 dm^3 stainless steel cell that is mounted on the end of the Febetron and receives the electron beam through a thin stainless steel entrance window in the cell. The irradiation cell is incorporated into a conventional all metal vacuum line and the gas mixtures are made in the cell by introducing the desired component partial pressures using an MKS Baratron model 170 membrance manometer.

The pulse radiolysis machine is fired in coincidence with the pulsing of an analysing light source. A Varion 150W high pressure xenon lamp, with an aluminized parabolic reflector and sapphire window, is used as this source and emits light in the region of 200–300 nm. Using a pulsing device originally designed by Hvild and

Figure (2.10) The Pulse Radiolysis / Kinetic Absorption Apparatus.

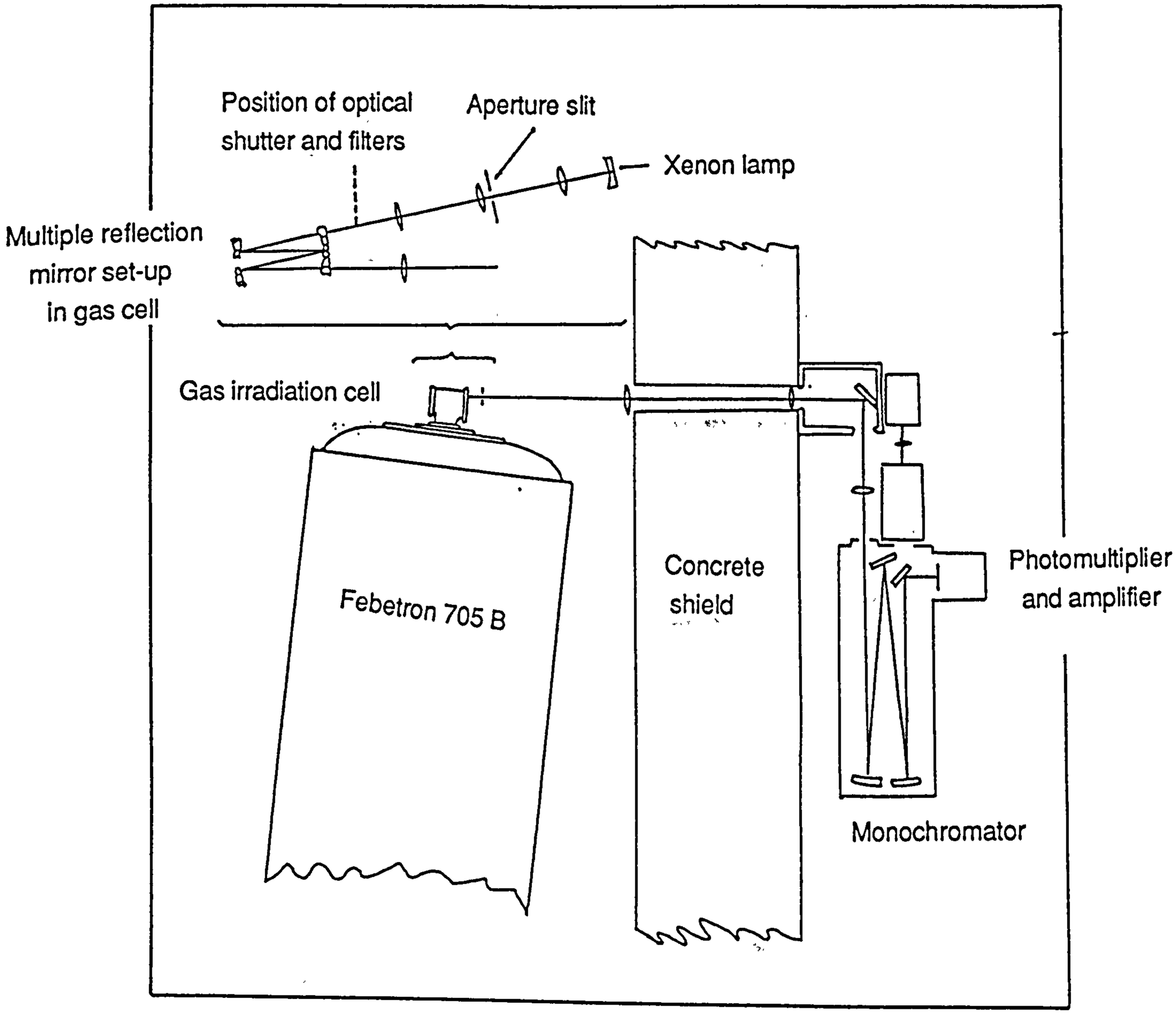

Nielson[57], the lamp can emit "flat" light pulses with a duration of a few milliseconds and at a roughly 50-fold gain in the normal output. The P.R./K.A. event is triggered by pulsing the xenon lamp and uses the attainment of the gained output as a signal for the Febetron to deliver the electron pulse.

The pulse radiolysed mixtures are analysed using an optical system, that consists of seven suprasil lenses and a sequence of aluminised mirrors, and is shown in figure (2.11). This system directs the xenon lamp output through the irradiation cell, where it undergoes a multi-pass, by virtue of a conjugate pair of internal mirrors, and subsequently into a 1m Hilger and Watts monochromator. The conjugate mirrors are used to allow up to 16 traversals of the analysing eight through the irradiation cell, giving a path length of up to 160 cm. The monochromator possesses a grating that consists of 1200 lines/mm, blazed at 300 nm, and gives a reciprocal dispersion of 0.8 nm/mm. The analysing light that passes the exit slit of the monochromator is detected by an EMI 9558 QB photomultiplier to give a transient signal that is stored in a Biomation 8100 2000 word waveform digitizer. The minimum sampling time for each word is 10^{-8} s and the experimental time is thereby limited to $> 20\ \mu s$. The digitizer is interfaced to a PDP 8 minicomputer that is used in the analysis of the raw data. Additionally, the observed absorbance is immediately plotted against time on a display screen.

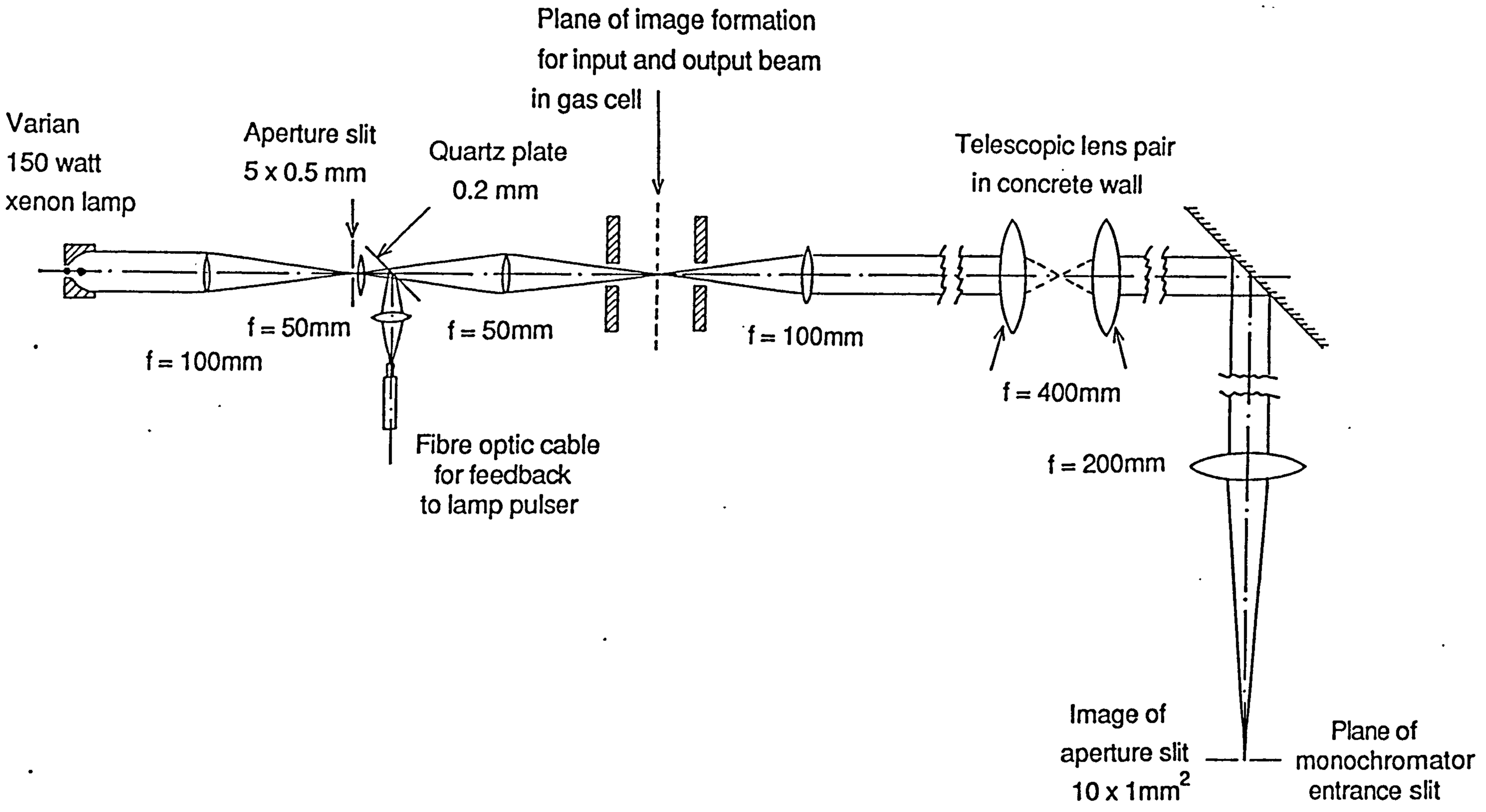

Figure (2.11) Optical System of the Pulse Radiolysis / Kinetic Absorption Apparatus.

CHAPTER 3 THE PYROLYSES OF ORGANIC NITRATES PEROXIDES AND NITRITES

(3.1) INTRODUCTION

This chapter concerns the low temperature pyrolyses, in our flow reactor, of the ignition improvers that were studied by Kirsch and Selby under autoignition conditions. Accordingly, the pyrolyses of 2-^{n}butoxyethyl nitrate (BEN), di-^{t}butyl peroxide (DTDP) (Chapter 2), ^{i}propyl nitrate (IPN) and the surrogates of both 2-methoxyethyl nitrate, di-^{n}butyl peroxide (DNBP) and ^{n}butyl nitrite (NBN), and di-^{t}butyl peroxide, ^{t}butyl cumyl peroxide (TBCP), have been performed. These pyrolysis studies allow the empirical rank activities of these ignition improvers, found by Kirsch and Selby, to be understood from both the decomposition kinetics of these materials and from the chemistries of the alkoxy radicals, they decompose to furnish.

An autoignition study of nitrogen dioxide as an ignition improver, analogous to the nitrate and peroxide studies of Kirsch and Selby, constitutes the following chapter and, eventually, will allow an inter alia extension of the above understanding between these nitrates and peroxides.

The previous pyrolyses of organic nitrates, peroxides and nitrites, under first order conditions, were briefly surveyed in Chapter 2 and the Arrhenius parameters for the homolyses of the weakest bonds in these materials were summarized. An additional advantage of these pyrolysis conditions arises from the attendant freedom of the initial pyrolyte alkoxy radicals from reaction with their parents, that

allows the reactivities of these radicals to be easily explored both unimolecularly or, by offering additional reactant molecules, bimolecularly.

The pyrolyses of the above ignition improvers have been performed in our flow reactor under first order conditions of low pyrolyte partial pressures and in an excess of oxygen. In order to preserve the plug flow character of the reactor, the amount of oxygen was limited to only a few per cent of the total flow. The presence of oxygen converts the intermediate alkyl radicals to their peroxy analogues, both irreversibly[58], and, under the composition and temperature conditions of these studies, without any subsequent pyrolysis kinetic complications[27].

The low temperature pyrolysis studies of the above ignition improvers were anticipated to complicate in sympathy with their activities and were therefore performed in reciprocal order to the empirical activity order, found by Kirsch and Selby, of these materials.

(3.2) EXPERIMENTAL

(3.2.1) Sources of materials.

The ignition improvers that have been pyrolysed in our studies came from the following sources. Di-^{t}butyl peroxide, ^{i}propyl nitrate and ^{n}butyl nitrite were all bought from Aldrich. ^{t}Butyl cumyl peroxide was a gift from Laporte, 2-^{n}butoxyethyl nitrate was provided by Shell Research Ltd. and di-^{n}butyl peroxide was specifically synthesised for this pyrolysis study. Both the preparative work that supported these studies, and most of the materials that

were used as gas chromatography standards, were bought from Aldrich or Lancaster Synthesis.

(3.2.2) Preparative work.

(i) The preparation of di-^{n}butyl peroxide.

Di-^{n}butyl peroxide was prepared in a two step synthesis from ^{n}butanol. The first step reacted ^{n}butanol with methanesulphonyl chloride to give ^{n}butyl methanesulphonate, by the method of Sekara and Marvel[59]. The ^{n}butyl methanesulphonate was isolated for the second step, where it was reacted with hydrogen peroxide to give di-^{n}butyl peroxide by the method of Welch, Williams and Mosher[60]. The synthesis is shown in the scheme below and steps (I) and (II) are subsequently discussed.

$$^{n}BuOH + CH_3SO_2Cl \xrightarrow{(I)} CH_3SO_2O^{n}Bu \xrightarrow{(II)} {}^{n}BuOO^{n}Bu$$

(I) The preparation of ^{n}butyl methanesulphonate.

A mixture of 304 g (2.64 mole) of methanesulphonyl chloride and an equivalent amount of ^{n}butanol was stirred in an ice bath. 417.6 g (5.28 mole) of dry pyridine was added at a temperature of 0-5^{o}C over a period of 3.5 hours. The stirring was continued for one-quarter hour, after which the reaction mixture was poured into 825 ml of ice-cold 10% hydrochloric acid, and the product was extracted with 495 ml of ether. The resulting solution was washed with two 130 ml portions of water, followed by a 200 ml portion of saturated sodium bicarbonate solution. The solution was dried over anhydrous potassium carbonate solution, filtered and rotary evaporated

to remove the ether.

The crude ^{n}butyl methanesulphonate was vacuum distilled, without a column, using an oil rotary pump. The ^{n}butyl methanesulphonate boiled between 77 and 79°C at 2.6 mb, where 250 g (1.65 mole) were collected. The efficiency of this step was 63%.

(II) The preparation of di-^{n}butyl peroxide.

A mixture of 200 g (1.32 mole) of n-butyl methanesulphonate, 0.66 mole 30% aqueous hydrogen peroxide, prepared by diluting an accurately determined ~ 100 vol. aqueous solution of this reagent, and 670 ml methanol was cooled to 0°C. 1.32 mole of 50% aqueous potassium hydroxide was added to the cooled mixture over a period of a few minutes with stirring. The resulting solution was allowed to come slowly to room temperature and to react thereafter, for a total of 12 hours, where a precipitate of potassium methanesulphonate formed. Water was added to the reaction mixture to dissolve the potassium methanesulphonate and the resulting solution was extracted twice, each with 100 cm^3 of pentane.

The two pentane solutions were combined and washed successively with 50 cm^3 of 5% aqueous potassium hydroxide, to remove any hydroperoxide, and then with distilled water, until the washings were neutral. The pentane solution was finally dried over anhydrous sodium sulphate and the pentane was removed by rotary evaporation.

The crude di-^{n}butyl peroxide was vacuum distilled, through a 10 cm column packed with glass beads, using an oil rotary pump. The di-^{n}butyl peroxide boiled between 39 and 41°C at 0.8 mb, where 36.1 g (0.25 mole) were collected. The efficiency of this step was 38%.

The successful peroxide synthesis was confirmed by mass spectrometry, using the Department's Kratos MS 20 machine, and the observed mass spectrum is shown in figure (3.1). Although a literature mass spectrum of di-^{n}butyl peroxide could not be found, for comparison with that of figure (3.1), the spectrum can be assigned in accordance with both the parent molecular ion and fragmentation pattern expected for the peroxide. Accordingly, the principal peaks of the mass spectrum, at low resolution, are assigned below.

Peak m/e	Assignment
146	$(^{n}C_4H_9O)_2^{+\cdot}$
86	$C_6H_{14}^{+\cdot}$
72	$C_3H_7CHO^{+\cdot}$
57	$C_4H_9^{+\cdot}$
43	$C_3H_7^{+\cdot}$

The peak at m/e = 86 has a particularly interesting assignment to the hexane radical cation, which may be formed from the parent molecular ion by a six centred cyclic extrusion reaction.

The purity of the peroxide was checked by gas chromatography, where no impurities could be found.

(ii) The preparation of ^{n}butoxyacetaldehyde

^{n}Butoxyacetaldehyde was synthesised on a small scale as a gas chromatographic standard, in connection with the pyrolysis study of 2-^{n}butoxyethyl nitrate.

High boiling aldehydes can not be prepared classically from the oxidation of the corresponding alcohol with acidified sodium dichromate, due to the difficulties of isolating the product[61].

Figure (3.1) Mass spectrum of di-^{n}butyl peroxide.

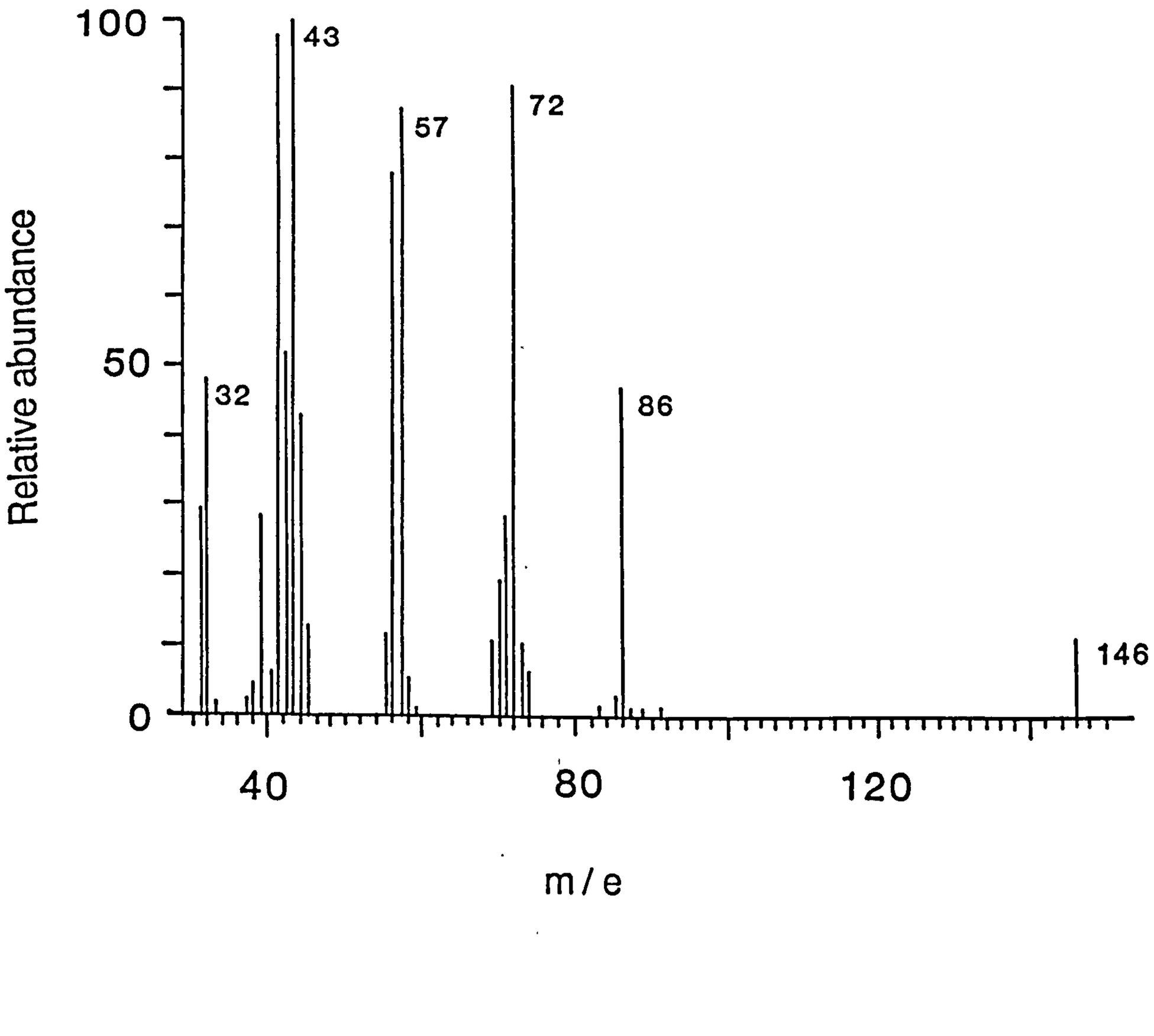

^{n}Butoxyacetaldehyde was therefore prepared by a variation of a method of Johnson and Pelter[62].

A mixture of 238 cm^3 of dried dimethyl sulphoxide and 31.8 g of sodium hydrogen carbonate was stirred at 150°C under dry nitrogen. 1.26 g of 2-^{n}butoxyethyl bromide was added to this mixture and after 4 minutes the reaction was quenched by rapid external cooling. The reaction mixture was poured into water and extracted three times, each with 150 cm^3 of ether. The ether solutions were combined, washed twice, each with an equal volume of water, dried over anhydrous magnesium sulphate and filtered. The ether was removed by rotary evaporation to give the crude aldehyde.

(3.2.3) Purification of materials.

All of the commercially obtained ignition improvers were found by gas chromatography to be sufficiently pure for immediate use (ca. 99%).

Di-^{n}butyl peroxide was purified by vacuum distillation after synthesis. ^{t}Butyl cumyl peroxide and 2-^{n}butoxyethyl nitrate were found to be impure by gas chromatography and were purified chemically and by vacuum distillation respectively. ^{t}Butyl cumyl peroxide contained acetone and acetophenone impurities and was purifed by stirring for half an hour with an aqueous solution of saturated sodium metabisulphite ($Na_2S_2O_5$), where these ketones were removed by precipitation as their metabisulphite adducts. The supplied 2-^{n}butoxyethyl nitrate contained the corresponding alcohol as an impurity and was purified by vacuum distillation through a 30 cm column packed with glass beads, using an oil rotary pump. The nitrate boiled between 38 and 40°C at 0.06 mb.

(3.2.4) Vapour pressures of pure materials.

The vapour pressures of the ignition improvers were measured to allow their pyrolysis amounts in the flow reactor to be calculated. The procedure for making these measurements was described in sub-section (2.1.4), and the measured vapour pressures, at 273K and room temperature, are given in table (3.1). The ignition improvers were generally introduced into the flow reactor as their vapour pressures at 273K, except for ^{t}butyl cumyl peroxide and 2-^{n}butoxyethyl nitrate, that were introduced as their room temperature vapour pressures on account of their involatility.

Table (3.1) Vapour pressures of the studied ignition improvers.

Ignition Improver	Vapour Pressure at 273K/mb.	Vapour Pressure at room temp./mb.
$^{t}BuO_2{}^{t}Bu$	11.6	25.5
$^{t}BuO_2Cu$	-	2.8
$^{n}BuO_2{}^{n}Bu$	0.8	2.8
$^{n}BuONO$	36.2	117.6
Me_2CHONO_2	20.6	45.9
$^{n}BuOCH_2CH_2-ONO_2$	-	2.0

(3.2.5) Gas Chromatography. The selection and operation of columns.

The pyrolysis studies we have performed are of a range of closely related ignition improvers. The gas chromatographic analyses of these pyrolyses were all attempted then using a di-nonyl phthalate (DNP) column that only proved suitable concerning the pyrolysis of

di-^{t}butyl peroxide and was generally unsuitable for these analyses in several regards. First, the more high boiling and less polar, ignition improvers, ^{t}butyl cumyl peroxide, di-^{t}butyl peroxide and 2-^{n}butoxyethyl nitrate, failed to elute from this column under any conditions and required the use of a variety of low loaded (3%) OV101 columns. Second, the DNP column was unable to separate ^{n}butyl nitrite and ^{n}butyaldehyde, which have closely similar boiling points, that required the use of a highly polar β,β-oxydipropionitrile, column that is recommended for nitrite separations[63]. Third, a Porapak Q column was required to separate hydrocarbons[64] and, fourth, a Carbopak column was required for a very specialized separation of some isomeric alcohols[65].

The above chromatography systems were used under optimized column, pre-operation and operation, conditions.

Optimized pre-operation conditions were achieved by using silanized gas chromatography materials and by thermally conditioning the column immediately prior to use. Silanization[66] is a desirable pre-treatment of chromatography materials, including the empty glass columns, glass wool plugs, and for gas liquid chromatography, the liquid phase support, and is aimed at eliminating any problems due to tailing. The column packings were purchased then, where appropriate, with silanized supports, and all of the glass columns and plugs were silanized by the following treatment. (1) The empty column or plug was washed with dilute acid and rinsed with distilled water. (2) The column or plug was silanized with a 5% solution of hexa-methyl disilazine (H.M.D.S.) in toluene and allowed a ten minute standing time. (3) The column solution was displaced first with toluene and then with methanol. The plugs were similarly washed. (4) The column was purged with nitrogen. Subsequently,

the prepared columns were always thermally cleaned before use by an overnight heating, at a maximum temperature ca. 20K higher than the maximum analysis temperature, with the through-passage of the nitrogen carrier gas.

The gas chromatography was developed, initially, by injecting the individual and suspected pyrolysis mixture components into a selected column that was ballistically operated between its lower and upper temperature limits, in a timed program that began with the injection. These analyses gave an idea of a suitable isothermal column temperature to separate the suspected pyrolysis mixture components, that was subsequently optimized by repeating this procedure, except, first, at varying isothermal temperatures, and, subsequently, using gas phase samples, as described in sub-section (2.1.4). The g.c. separations achieved by this procedure are detailed in table (3.2).

(3.3) RESULTS AND DISCUSSION

(3.3.1) The pyrolysis of ^{t}butyl cumyl peroxide.

The pyrolysis of 0.11 mb ^{t}butyl cumyl peroxide, 38.5 mb oxygen in a balance of 1b helium was performed between 450 and 491K.

The pyrolysis of ^{t}butyl cumyl peroxide provides both the ^{t}butoxy and cumyloxy radicals in, according to the earlier pyrolysis study of di-^{t}butyl peroxide, reactive states that are disposed towards decomposition, that, in the latter case, can competitively occur to give either acetone or acetophenone as molecular products.

Table (3.2) Summary of gas chromatography analysis

Column	Number of turns Int. Diam/mm	Flow Rate N_2 /ml min^{-1}	Temp. /°C.	Material	Retention time/min.
20% DNP on 80-100 mesh Gas Chrom Q. (Phase Sep.)	3,4	30	55	Me_2CO	4.4
				^nBuOMe	6.4
					7.0
				^nPrCHO	8.5
				$^tBuO_2{}^tBu$	14.7
				^nBuOH	24.1
				MeCHO	1.9
				Me_2CO	3.4
				Me_2CHOH	5.5
				Me_2CHONO_2	13.5
				$^tBuO_2H$	26.6
20% DNP on 80-100 mesh Gas Chrom Q (Phase Sep.)	½,4	46	75	Me_2CO	0.7
			75°C for 0.7 mins and then ballistically to 125°C.	PhCOMe	8.6
3% OV101 on 80-100 mesh Chromosorb W HP. (Phase Sep.)	3,4	30	65	$^nBuO_2{}^nBu$	9.1
				$^nBuOCH_2CHO$	2.5
				$^nBuOCH_2CH_2OH$	4.7
				$^nBuOCH_2CH_2ONO_2$	2.7

3% OV101 on 80-100 mesh Chromosorb W HP (Phase Sep.)	½ (including a 2/5 turn Gas Chrom Q pre-column.) 4	30	90	$^{t}BuO_2Cu$	2.5
20% β,β-dioxypropionitrile on 80-100 mesh Gas Chrom Q. (Phase Sep.)	8,2	30	75	$^{n}BuONO$	5.5
				$^{n}PrCHO$	16.0
				$^{n}BuOH$	45.4
Porapak Q at 80-100 mesh (Phase Sep.)	3,4	30	125	C_3H_6	3.7
				C_4H_{10}	10.3
Carbopak C/0.1% SP1000 at 80-100 mesh (Supelco)	3,2	13	150	Me_2CO	1.9
				$CH_2=CHCH_2CH_2OH$	3.8
				$^{n}BuOH$	4.2
				$CH_3CH=CHCH_2OH$	4.4
				$(CH_3)_2CHCH_2CH_2OH$	10.0
				$^{n}PrCHO$	10.8
				$^{n}C_5H_{11}OH$	12.2
				$^{t}BuO_2{}^{t}Bu$	25

$$^{t}BuO_2Cu \longrightarrow {}^{t}BuO\cdot + CuO\cdot$$

$$^{t}BuO\cdot \longrightarrow Me_2CO + Me\cdot$$

$$CuO\cdot \longrightarrow PhCOMe + Me\cdot$$

$$CuO\cdot \longrightarrow Me_2CO + Ph\cdot$$

The pyrolysis of ^{t}butyl cumyl peroxide, under the above conditions, proceeded by first order kinetics, and, accordingly, the peroxide decompositions and acetone and acetophenone formations are shown, in the usual forms, in figures (3.2) to (3.4) respectively. The product yields, at complete reaction, used to plot figures (3.3) and (3.4), are given, in tables (3.3) and (3.4) respectively. The slopes of the lines in figures (3.2) to (3.4) give the first order pyrolysis rate constants for ^{t}butyl cumyl peroxide and are plotted together, in Arrhenius form, in figure (3.5), where the solid line is a linear regression fit through all of the data. Accordingly, the Arrhenius equations are given below for (a) the peroxide decomposition (b) the acetone formation (c) the acetophenone formation (d) all the rate constant data.

(a) $\log_{10}(k/s^{-1}) = 14.74 \pm 0.87 - (34.3 \pm 1.9)$ kcal mol^{-1}/RT ln 10

(b) $\log_{10}(k/s^{-1}) = 13.72 \pm 1.56 - (31.9 \pm 3.4)$ kcal mol^{-1}/RT ln 10

(c) $\log_{10}(k/s^{-1}) = 15.25 \pm 2.54 - (35.0 \pm 5.5)$ kcal mol^{-1}/Rt ln 10

(d) $\log_{10}(k/s^{-1}) = 14.5 \pm 1.07 - (33.8 \pm 2.3)$ kcal mol^{-1}/RT ln 10

The pyrolysis of ^{t}butyl cumyl peroxide in the gas phase, has been performed, here, for the first time, and the similarities between the above Arrhenius equations confirm their reference to the isolated

Figure (3.2) First order ^{t}butyl cumyl peroxide decompositions in the pyrolysis of 0.11mb ^{t}butyl cumyl peroxide in 38.5mb oxygen and a 1b helium balance.

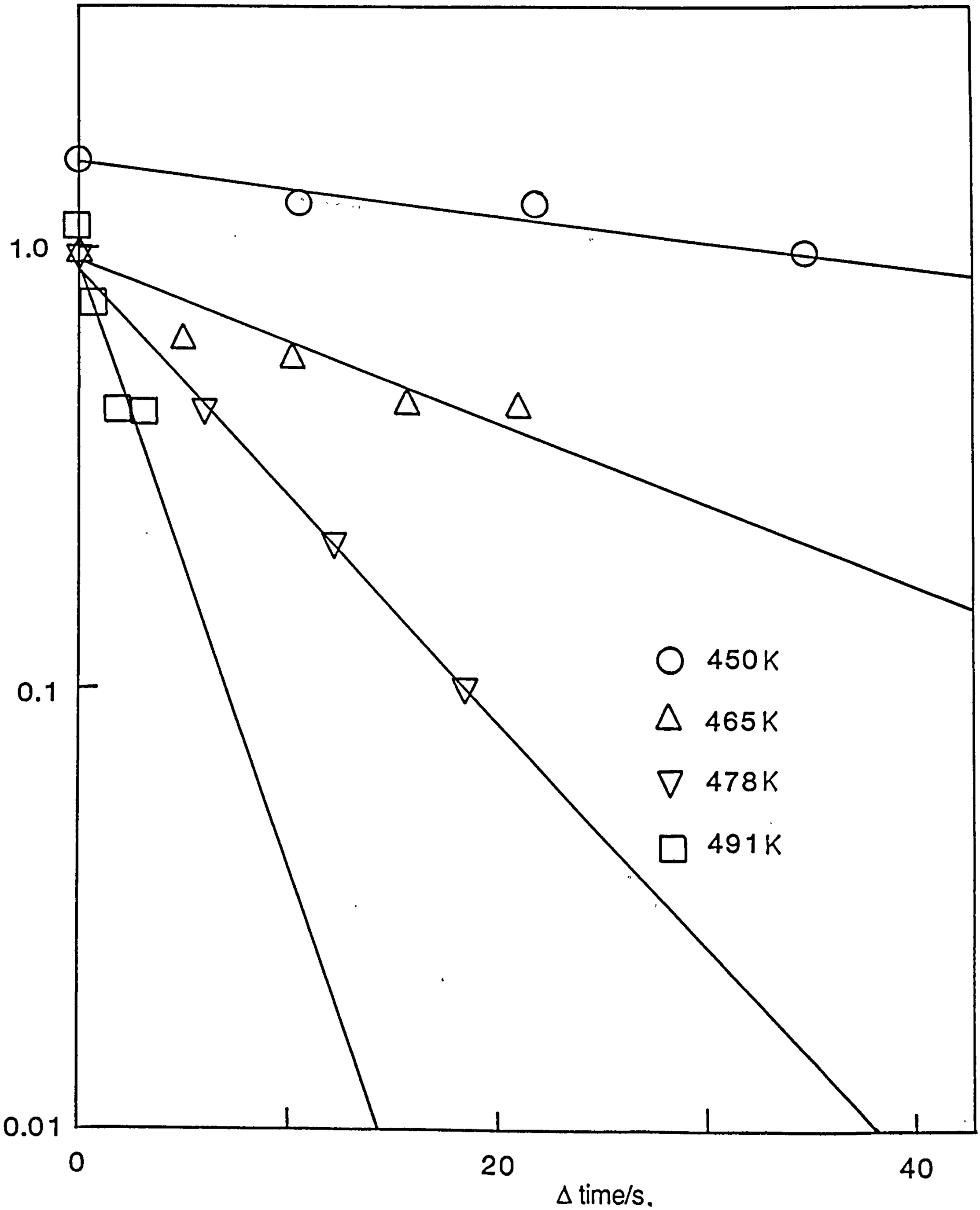

Figure (3.3) First order acetone formations in the pyrolysis of 0.11mb ^{t}butyl cumyl peroxide in 38.5mb oxygen and a 1b helium balance.

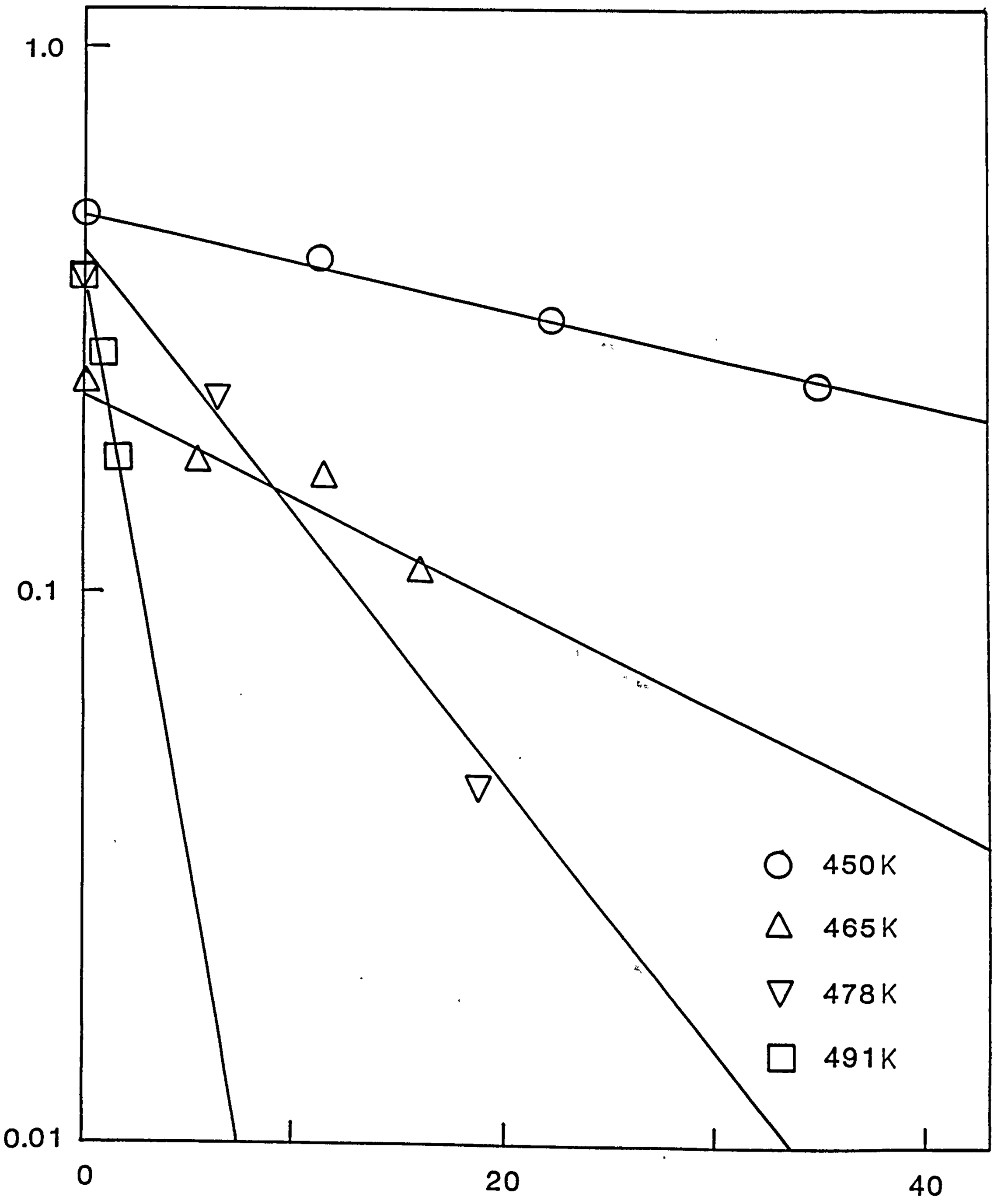

Figure (3.4) First order acetophenone formations in the pyrolysis of 0.11mb ^{t}butyl cumyl peroxide in 38.5mb oxygen and a 1b helium balance

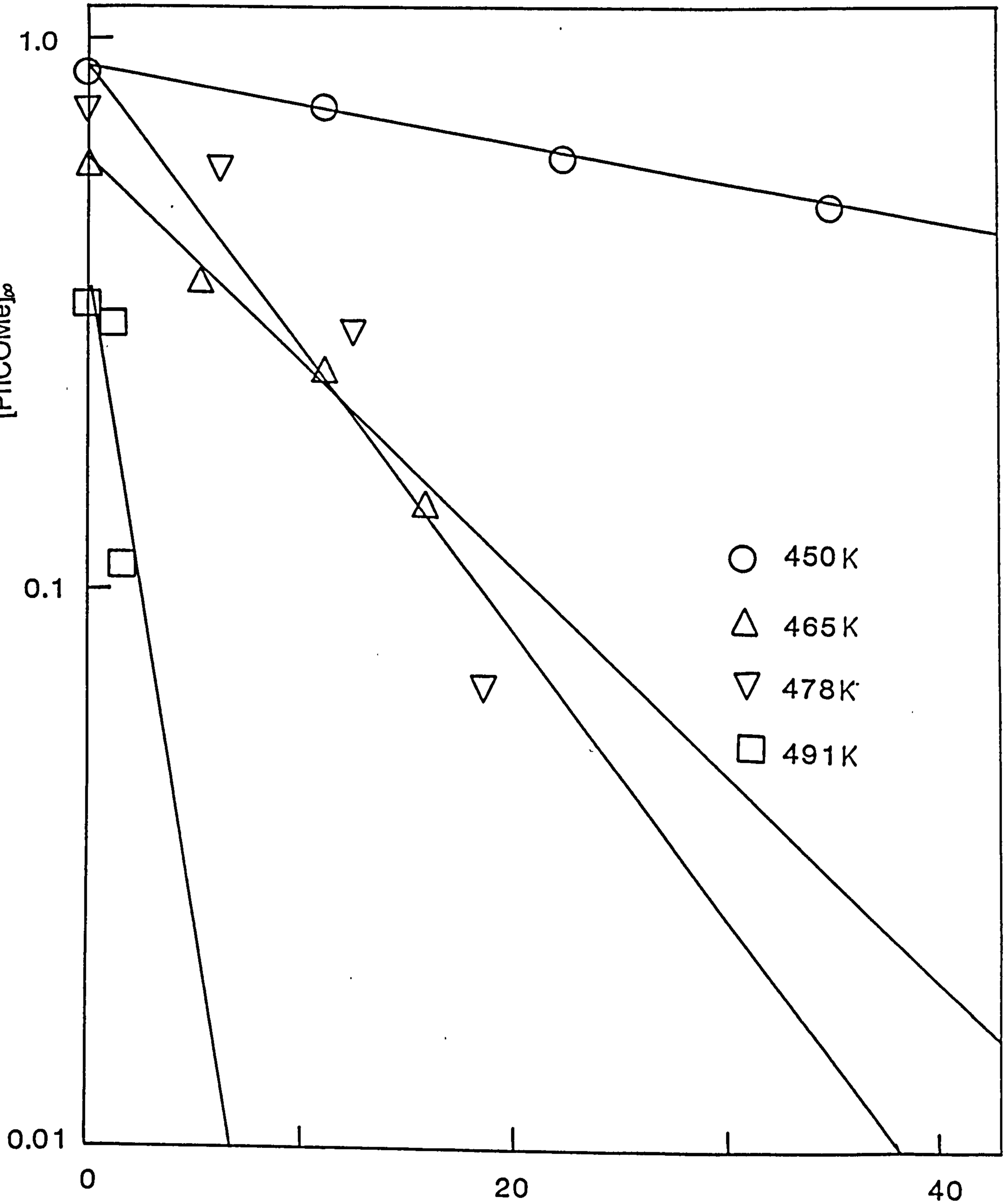

Figure (3.5) Arrhenius plot for the pyrolysis of ^{t}butyl cumyl peroxide.

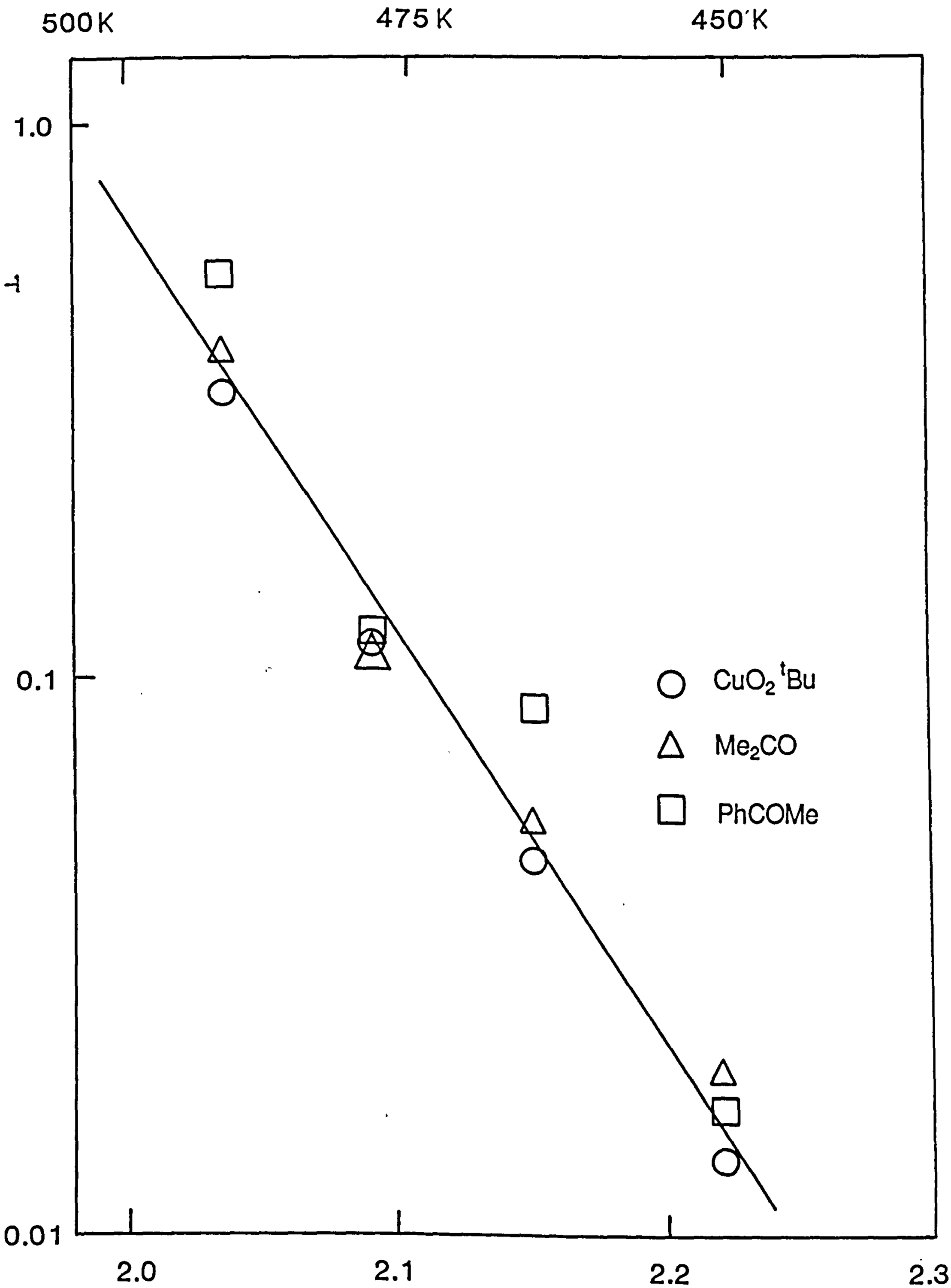

Table (3.3) Acetone formations in the pyrolysis of ^{t}butyl cumyl peroxide. Acetone absolute pressures in mb x 10^2. Values in parenthesis are changes in reaction time in seconds.

Temp.(K)					
450	2.0(0)	2.4(11.1)	2.7(22.2)	3.0(35.0)	4.0(∞)
465	0.37(0)	2.1(5.3)	2.1(10.6)	2.2(16.0)	2.5(∞)
478	3.3(0)	4.0(6.3)	-	5.0(18.8)	5.3(∞)
491	2.7(0)	3.2(1.0)	3.6(2.0)	-	4.4(∞)

Table (3.4) Acetephenone formations in the pyrolysis of ^{t}butyl cumyl peroxide. Acetophenone absolute pressure in mb x 10^2. Values in parenthesis are changes in reaction time in seconds.

Temp.(K)					
450	0.29(0)	0.55(11.1)	0.86(22.2)	1.1(35.0)	2.2(∞)
465	0.64(0)	1.0(5.3	1.2(10.6)	1.3(16.0)	1.5(∞)
478	0.60(0)	1.0(6.3)	1.7(12.5)	2.2(18.8)	2.4(∞)
491	1.5(0)	1.5(1.0)	2.0(2.0)	-	2.2(∞)

pyrolytic homolysis of the peroxide. The pyrolysis of ^{t}butyl cumyl peroxide, in liquid cumene, has been studied by Kharasch[67], where the Arrhenius equation for the pyrolysis was found to be $\log_{10}(k/s^{-1}) = 13.3 - 35.0$ kcal mol^{-1}/RT ln 10, and is in good agreement with our study.

The competitive cumyloxy radical decomposition reactions have been kinetically determined from the relative yields of acetone, $y(Me_2CO)$, and acetophenone, y(PhCOMe), that are given, calibrated, in tables (3.3) and (3.4) respectively. The relative rates of these respective reactions, T, is given by the expression below, that accounts for the exclusive formation of acetone from the ^{t}butoxy radical.

$$T = 0.5 \frac{y(Me_2CO)}{y(PhCOMe)} - 0.5$$

The average values of y(Me_2CO)/y(PhCOMe) are 3.8 at 450K, 1.6 at 465K, 3.5 at 478K and 1.9 at 491K. The errors in these ratios suggest an average value of 2.7 at the mid-temperature of the study, 471K, where T then is 0.85. The cumyloxy radical then, allowing for the one and two fold decomposition degeneracies of this radical, to respectively give acetone and a phenyl radical or acetophenone and a methyl radical, undergoes a methyl radical loss that is 1.7 times faster than that of the phenyl radical at 471K.

This conclusion is supported first, by the work of Benson[69], who has shown that the rate differences between competing alkoxy radical decomposition reactions increase in sympathy with their endothermicity differences, and in the case of the cumyloxy radical, are given by a 16.3 kcal mol^{-1} lower endothermicity for the loss of a methyl than a phenyl radical[68]. Second, Bailey and Godin[70] have pyrolysed dicumyl peroxide in liquid cumene between 384 and 483K, where a product study found that the cumyloxy radical exclusively decomposed to give acetophenone and a methyl radical under these conditions.

(3.3.2) The pyrolysis of ^{i}propyl nitrate.

The pyrolysis of 0.23 mb ^{i}propyl nitrate in 47.6 mb oxygen in a balance of 1b helium was performed between 489 and 545K.

The pyrolysis of ^{i}propyl nitrate provides the ^{i}propoxy radical, that may decompose to give either acetaldehyde and the methyl radical or acetone and the hydrogen atom, or react with oxygen, again to give acetaldehyde.

$$Me_2CHONO_2 \longrightarrow Me_2CHO\cdot + NO_2$$

$$Me_2CHO\cdot \longrightarrow MeCHO + CH_3\cdot$$

$$Me_2CHO\cdot \longrightarrow Me_2CO + H\cdot$$

$$Me_2CHO\cdot + O_2 \longrightarrow Me_2CO + HO_2\cdot$$

The first order nitrate decompositions and acetaldehyde formations are shown, in the usual forms in figures (3.6) and (3.7) respectively. The temperature dependencies of the rates of (a) nitrate decomposition and (b) acetaldehyde formation are shown, in Arrhenius form, in figure (3.8), where a linear regression analysis has been used to derive the Arrhenius equations for these processes.

(a) $\log_{10}(k/s^{-1}) = 14.56 \pm 1.69 - (37.4 \pm 4.0)$ kcal mol^{-1}/RT ln 10

(b) $\log_{10}(k/s^{-1}) = 14.50 \pm 1.53 - (37.4 \pm 3.6)$ kcal mol^{-1}/RT ln 10

The activation energies measured here, for these processes are in fair agreement with a value of 43.1 ± 3.1 kcal mol^{-1} reported by Gray[71] from a closed reactor study.

The ^{i}propoxy radical reactions to give either acetaldehyde or acetone have been kinetically determined from the calibrated formations of these products, that are given in tables (3.5) and (3.6) respectively. The yield ratios of acetaldehyde to acetone are 20.7 at 489K, 3.0 at 497K, 15.3 at 523K and 5.9 at 529K and suggest a value of 11.2, or a 12% ^{i}propoxy radical removal by decomposition to give acetaldehyde and the methyl radical, at the mean temperature of the study of 510K. The ^{i}propoxy radical decomposion kinetics to give acetaldehyde or acetone can be competitively determined from the above yield ratio at 510K, using a literature indication of the kinetics of the various ^{i}propoxy radical reactions. First, the relative ^{i}propoxy

Figure (3.6) First order ^{i}propyl nitrate decompositions in the pyrolysis of 0.23mb ^{i}propyl nitrate in 47.6mb oxygen and a 1b helium balance.

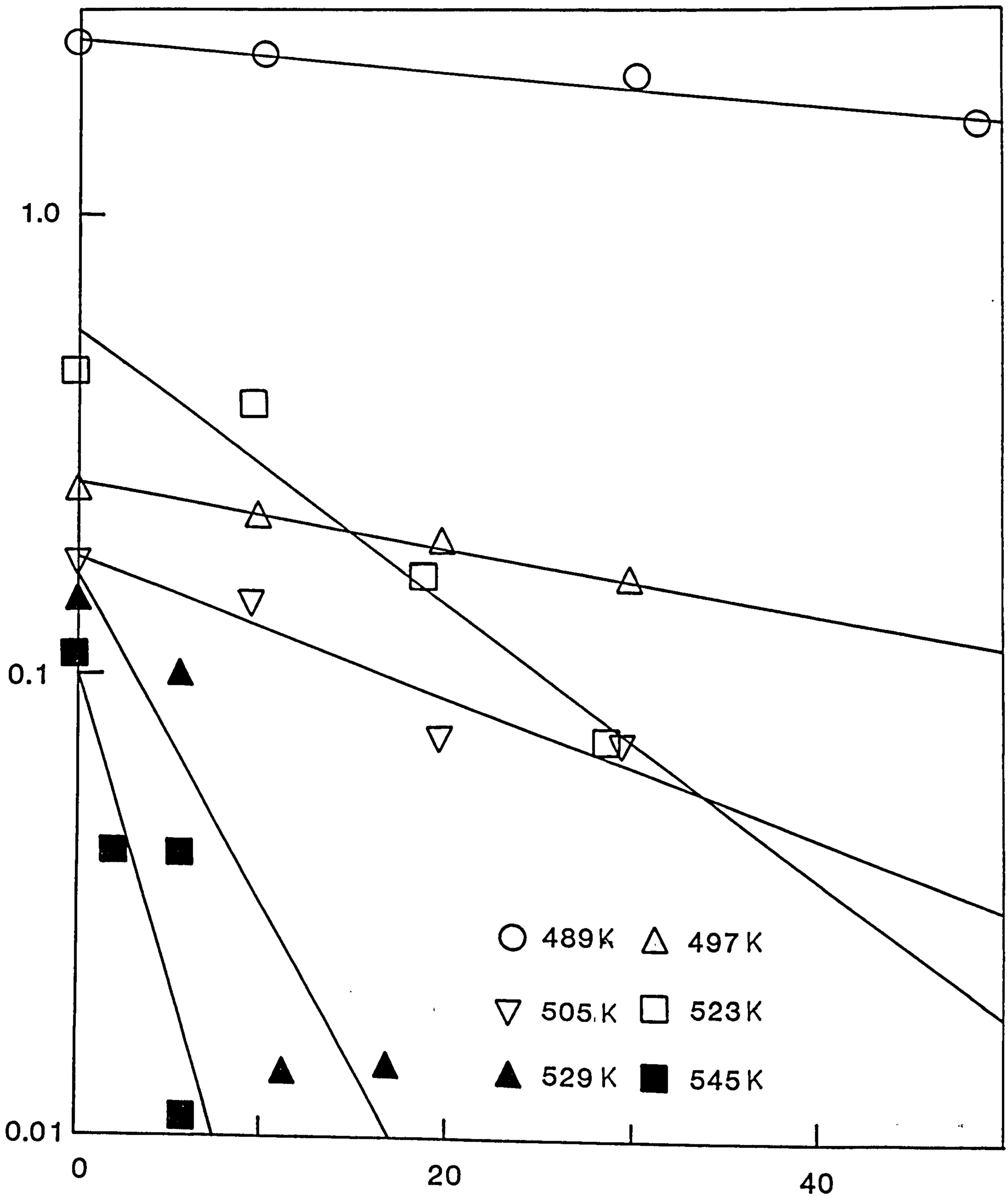

Figure (3.7) First order acetaldehyde formations in the pyrolysis of 0.23mb ^{i}propyl nitrate in 47.6mb oxygen and a 1b helium balance.

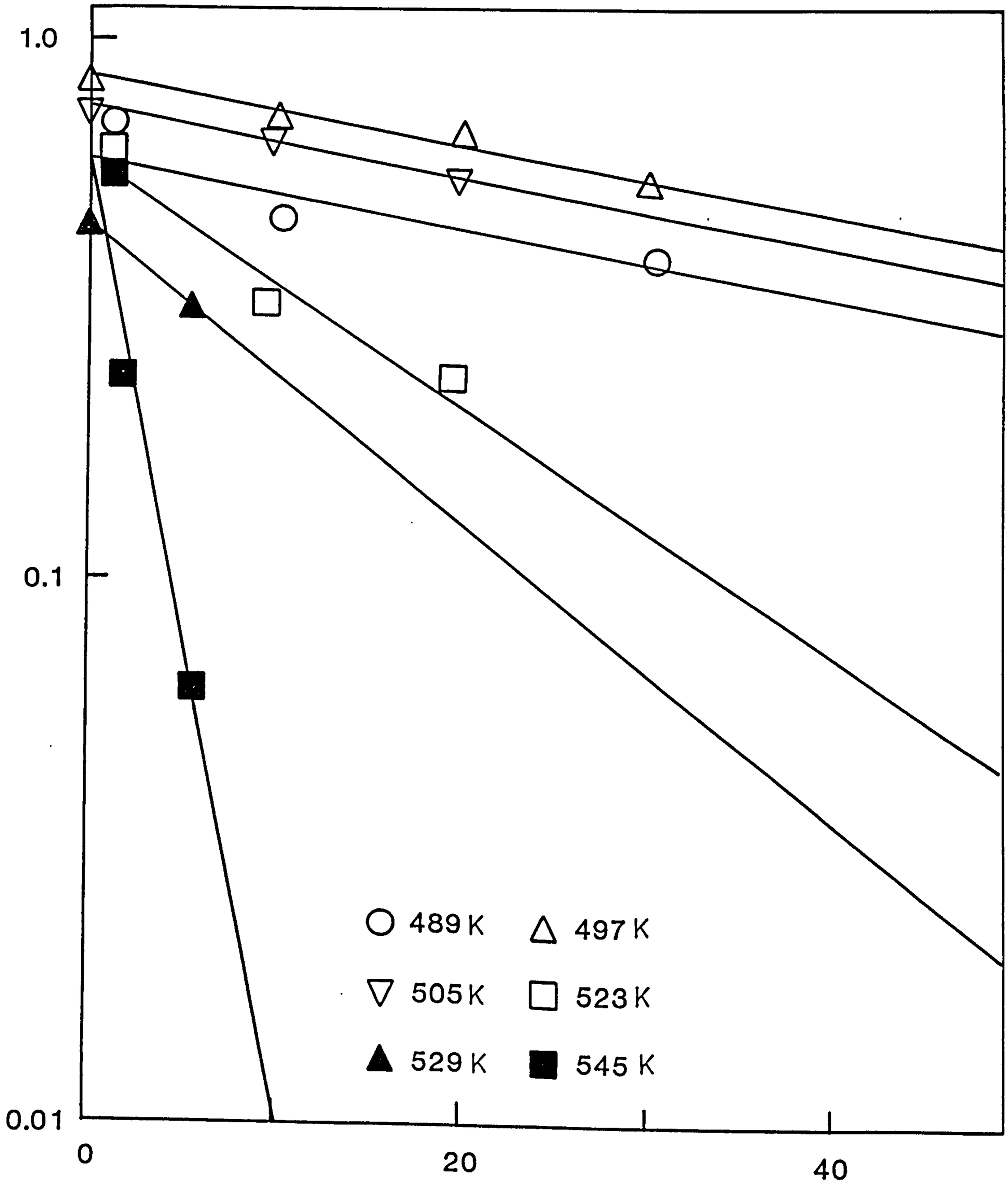

Figure (3.8) Arrhenius plot for the pyrolysis of ^{i}propyl nitrate.

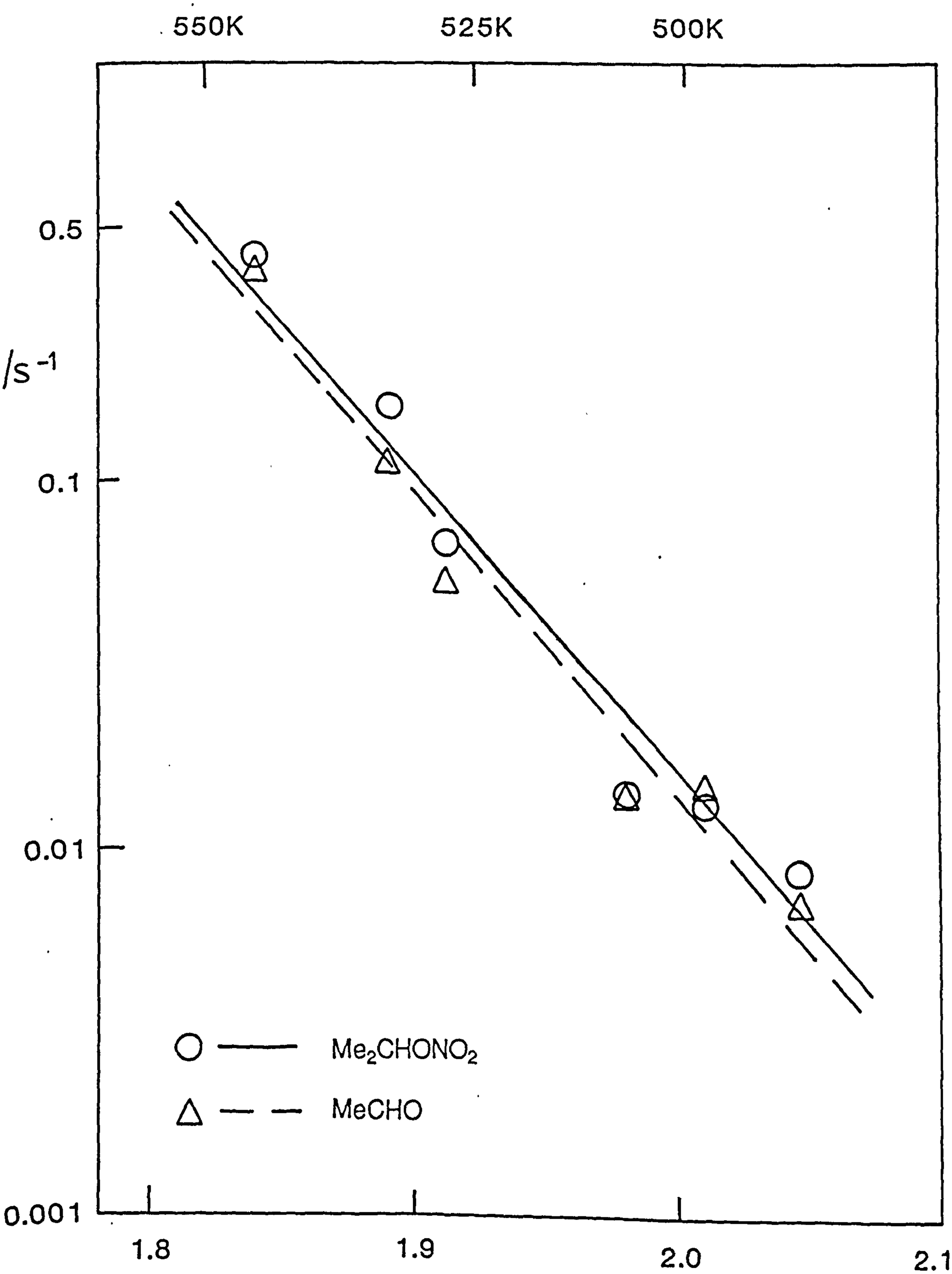

Table (3.5) Acetaldehyde formations in the pyrolysis of ^{i}propyl nitrate. Acetaldehyde absolute pressures in mb x 10^2. Values in parenthesis are changes in reaction time in seconds.

Temp.(K)					
489	5.0(0)	7.6(10.1)	8.6(30.3)	-	13.9(∞)
497	1.1(0)	2.0(10.0)	2.4(19.9)	3.1(29.9)	6.6(∞)
505	0.6(0)	0.7(9.8)	0.9(19.6)	-	2.0(∞)
523	4.9(0)	8.8(9.5)	9.9(18.9)	-	12.9(∞)
529	3.9(0)	4.9(5.6)	-	-	7.2(∞)
545	8.6(0)	16.5(1.8)	20.1(5.4)	-	21.5(∞)

Table (3.6) Acetone formations in the pyrolysis of ^{i}propyl nitrate. Acetone absolute pressures in mb x 10^2. Values in parenthesis are changes in reaction time in seconds.

Temp.(K)				
489	0.54(0)	0.27(10.1)	0.35(30.3)	1.1(48.5)
497	1.1(0)	0.79(10.0)	0.73(19.9)	0.62(29.9)
505	-	-	-	-
523	0.35(0)	0.56(9.5)	0.61(18.9)	0.41(28.4)
529	0.89(0)	0.67(5.6)	0.36(11.2)	0.53(16.8)
545	-	-	-	-

radical decomposition kinetics to give either acetaldehyde and the methyl radical or acetone and the hydrogen atom are indicated by Batt, who has studied the former process per se[19], and whose kinetic study of the methoxy radical decomposition reaction, to give formaldehyde and the hydrogen atom[72], offers a kinetic analogy for the latter process. Accordingly, the decomposition rate constants, at their high pressure limits, for these reactions are respectively 2.17×10^7 and 3855 s^{-1}, at 517K, which indicates that the ^{i}propoxy radical only decomposes to give acetaldehyde and the methyl radical in our study. Second, Balla[73] has studied the ^{i}propoxy radical reaction with excess oxygen, where the rate constant for this process

was measured to be 7.02 x 10^3 s^{-1} at 517K. The ^{i}propoxy radical decomposition kinetics to give acetaldehyde and the methyl radical, in our study, is approximately and competitively given then from our yield ratio and Balla's rate constant and calculates to 7.86 x 10^4 s^{-1}, in essentially 1 bar of helium. According to Batt, this rate constant is approximately two orders of magnitude lower than the high pressure limit value reported above.

(3.3.3) The copyrolysis of di-^{n}butyl peroxide and di-^{t}butyl peroxide.

The pyrolysis of di-^{n}butyl peroxide has been studied as a simple surrogate of 2-methoxyethyl nitrate and decomposes to provide the ^{n}butoxy radical.

$$^nC_4H_9O_2{}^nC_4H_9 \longrightarrow {}^nC_4H_9O\cdot + {}^nC_4H_9O\cdot$$

The efficacious ignition improver action of 2-methoxyethyl nitrate, compared to di-^{t}butyl peroxide or ^{i}propyl nitrate, was investigated from a study of the surrogate ^{n}butoxy radical reactivity, where, in contrast to the reactivities of the initial pyrolyte ^{t}butoxy and ^{i}propoxy radical products of these respective comparators, the possibility of an isomerization reaction has been identified[74].

Previously, the ^{n}butoxy radical reactivity has mainly been studied under pseudo atmospheric conditions, that include room temperature, where Carter et al.[74] have performed a smog chamber investigation of the photooxidation of ^{n}butane, nitrogen dioxide, air mixtures, where, apparently, the main products were formed via the isomerization of the ^{n}butoxy radical. Cox[75] and Niki[76] have independently tested this observation by studying the ^{n}butoxy radical reactivity in simpler environments. Cox has photolysed mixtures of

^{n}butane, nitrous acid and nitric oxide in an oxygen diluent, at 296K, and measured a variation in the relative ^{n}butoxy radical reaction rates by isomerization or with oxygen from 0.35, at 25% oxygen dilution, to 0.66, at essentially complete oxygen dilution. Niki has performed a similar study, except using ^{n}butyl nitrite, rather than the alkane, nitrous acid, nitric oxide system, as the ^{n}butoxy radical precursor, and measured this relative rate to be 0.23 in 700 torr of air at 298K. In both of these simplified studies, there was no evidence of the ^{n}butoxy radical decomposition reaction.

Heicklen[77] has photolysed ^{n}butyl nitrite, in oxygen, in the only temperature dependent study of the ^{n}butoxy radical reactivity, between 265 and 293K, and determined the competition kinetics of the reactions of this radical by isomerization or with oxygen. Accordingly, the ratio of these respective reaction rates was found to vary from 0.97 at 265K to 47.0 at 393K and, again, the ^{n}butoxy radical decomposition reaction was unobserved, even at the highest temperatures of this study. The V.L.P.P. of ^{n}butyl nitrite was studied by Golden[23], at 690K, where, at this elevated temperature, the ^{n}butoxy radical competitively reacted by isomerization and by decomposition, although no kinetic data was obtained.

These studies of the ^{n}butoxy radical reactivity emphasize the importance of the ^{n}butoxy radical isomerization reaction, particularly at room temperature, and suggest a basis for explaining the efficacious action of 2-methoxyethyl nitrate compared to the other considered ignition improvers. Accordingly, the pyrolysis of this material would initially give an alkoxy radical that isomerizes to a hydroxyalkyl radical that would be oxidized analogously to the initial fuel derived radicals. These ideas will be returned to later, but, on this basis, the pyrolysis of di-^{n}butyl peroxide was performed in the

absence of oxygen, where the unimolecular isomerization and decomposition reactions of the ^{n}butoxy radical were isolably investigated.

The ^{n}butoxy radical isomerization and decomposition reactions give radical products, and also formaldehyde in the latter case, and are consequently very difficult to observe, particularly as formaldehyde is insensitively detected by flame ionisation[78].

$$^{n}C_4H_9O\cdot \longrightarrow \cdot CH_2(CH_2)_3OH$$

$$^{n}C_4H_9O\cdot \longrightarrow CH_3CH(CH_2)OH$$

$$^{n}C_4H_9O\cdot \longrightarrow {}^{n}Pr\cdot + CH_2O$$

These ^{n}butoxy radical reactions were therefore investigated from the formation of more descendent products, derived from the initial ^{n}butoxy radical products, and the simplest situation involved limiting the number of descendents by trapping the initial ^{n}butoxy radical products to stable molecules. The methyl radical served as the trapping agent for this purpose in a study that is similar to the investigation of the 2-pentoxy radical isomerization reaction, performed by Berces[31], and mentioned in the introductory chapter.

We have copyrolysed di-^{n}butyl peroxide with excess di-^{n}butyl peroxide then, using the latter peroxide as the methyl radical source. Under these conditions, the possible isomerization and decomposition reactions of the ^{n}butoxy radical, that respectively give several hydroxyalkyl radicals and the ^{n}propyl radical, could be evidenced by the formations of several isomeric pentanols and several isomeric butanols, in the former case, and butane, propane and methane in the latter case.

$$\cdot CH_2(CH_2)_3OH + CH_3\cdot \longrightarrow {}^{n}C_5H_{11}OH$$

$$CH_3\dot{C}H(CH_2)_2OH + CH_3\cdot \longrightarrow Me_2CHCH_2CH_2OH$$

$$CH_3\dot{C}H(CH_2)_2OH + CH_3 \longrightarrow CH_2{=}CHCH_2CH_2OH + CH_4$$

$$CH_3\dot{C}H(CH_2)_2OH + CH_3\cdot \longrightarrow CH_3CH{=}CHCH_2OH + CH_4$$

$$^{n}Pr\cdot + CH_3\cdot \longrightarrow {}^{n}C_4H_{10}$$

$$^{n}Pr\cdot + CH_3\cdot \longrightarrow C_3H_6 + CH_4$$

The copyrolytic use of peroxide precursors for both the ^{n}butoxy and methyl radicals ensured, by the approximately generic temperature dependent productions of these radicals, that this study was free from any peculiarities of the copyrolysis situation.

The copyrolysis of 0.023 mb of di-^{n}butyl peroxide in a 14.1 fold excess of di-^{t}butyl peroxide and in a 1b balance helium balance was performed between 465 and 525K.

The copyrolysis of di-^{n}butyl and di-^{t}butyl peroxide was initially performed on a preliminary basis to investigate the possible occurrence of the ^{n}butoxy radical isomerization reaction via the formations of any alcoholic products. This preliminary study failed to identify these product formations, despite the use of a highly optimized g.c. system, and suggested that the ^{n}butoxy radical was either trapped by the methyl radical or underwent an exclusive decomposition reaction. The first of these possibilities was discounted by the non-observation of ^{n}butyl methyl ether and consequently the copyrolysis study was refocussed to study the di-^{n}butyl peroxide pyrolysis kinetics and to confirm the apparently exclusive ^{n}butoxy radical decomposition reaction. The confirmation of this latter

reaction was attempted pseudo competitively, against the known ^{t}butoxy radical decomposition reaction [28], in preference to a mass balance approach that, as mentioned in Chapter 2, is notoriously difficult in our flow reactor studies.

The copyrolysis of di-^{n}butyl and di-^{t}butyl peroxide occurred by first order kinetics for each peroxide and, accordingly, the decompositions of these peroxides are shown in figures (3.9) and (3.10) respectively. The copyrolysis kinetics of these processes are shown with their temperature dependencies in the Arrhenius plots of figure (3.11), where the scattered data owes to the protracted nature of this study. The pyrolysis of di-^{t}butyl peroxide occurred with an approximate activation energy of 32 kcal mol^{-1}, uncertain to about ± 5 kcal mol^{-1}. Correspondingly, the Arrhenius data for the pyrolysis of di-^{n}butyl peroxide is too scattered to derive any meaningful kinetic parameters for this process.

The ^{n}butoxy radical decomposition reaction to give the ^{n}propyl radical was competitively determined against the ^{t}butoxy radical decomposition reaction from the respective combined trapped adduct and disproportionate, ^{n}butane and propane, and exclusive acetone products of these radicals. The ^{n}butoxy radical fractional removal by decomposition, $\epsilon(^{n}BuO\cdot)_{d}$, is given against that of the ^{t}butoxy radical, $\epsilon(^{t}BuO\cdot)_{d}$, then by the ratio of the summed ^{n}butane and propane yields, $y(^{n}C_4H_{10}) + y(C_3H_6)$, against the acetone yield, $y(Me_2CO)$, allowing for both the copyrolytic di-^{n}butyl and di-^{t}butyl peroxide concentration ratio, 1:14.8, and also, strictly, a kinetic factor, that allows for any differences in the pyrolysis kinetics of these peroxides, although this is neglected here. The calibrated yields of these eventual ^{n}butoxy and ^{t}butoxy radical products are respectively given

Figure (3.9) First order di-^{n}butyl peroxide decompositions in the copyrolysis of 0.023mb di-^{n}butyl peroxide and 0.34mb di-^{t}butyl peroxide in a 1b helium balance.

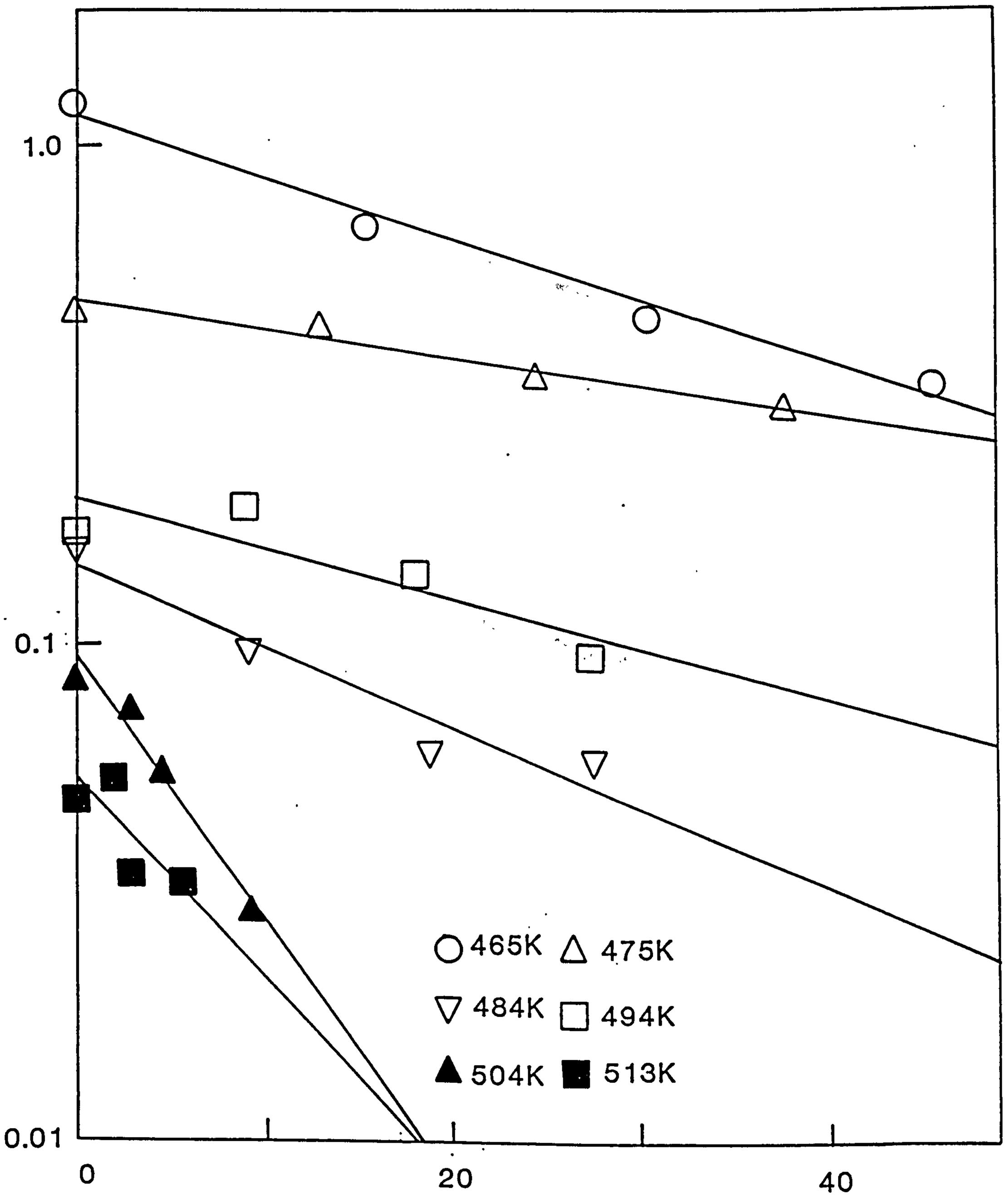

Figure (3.10) First order di-^{t}butyl peroxide decompositions in the copyrolysis of 0.023mb di-^{n}butyl and 0.34mb di-^{t}butyl peroxide in a 1b helium balance.

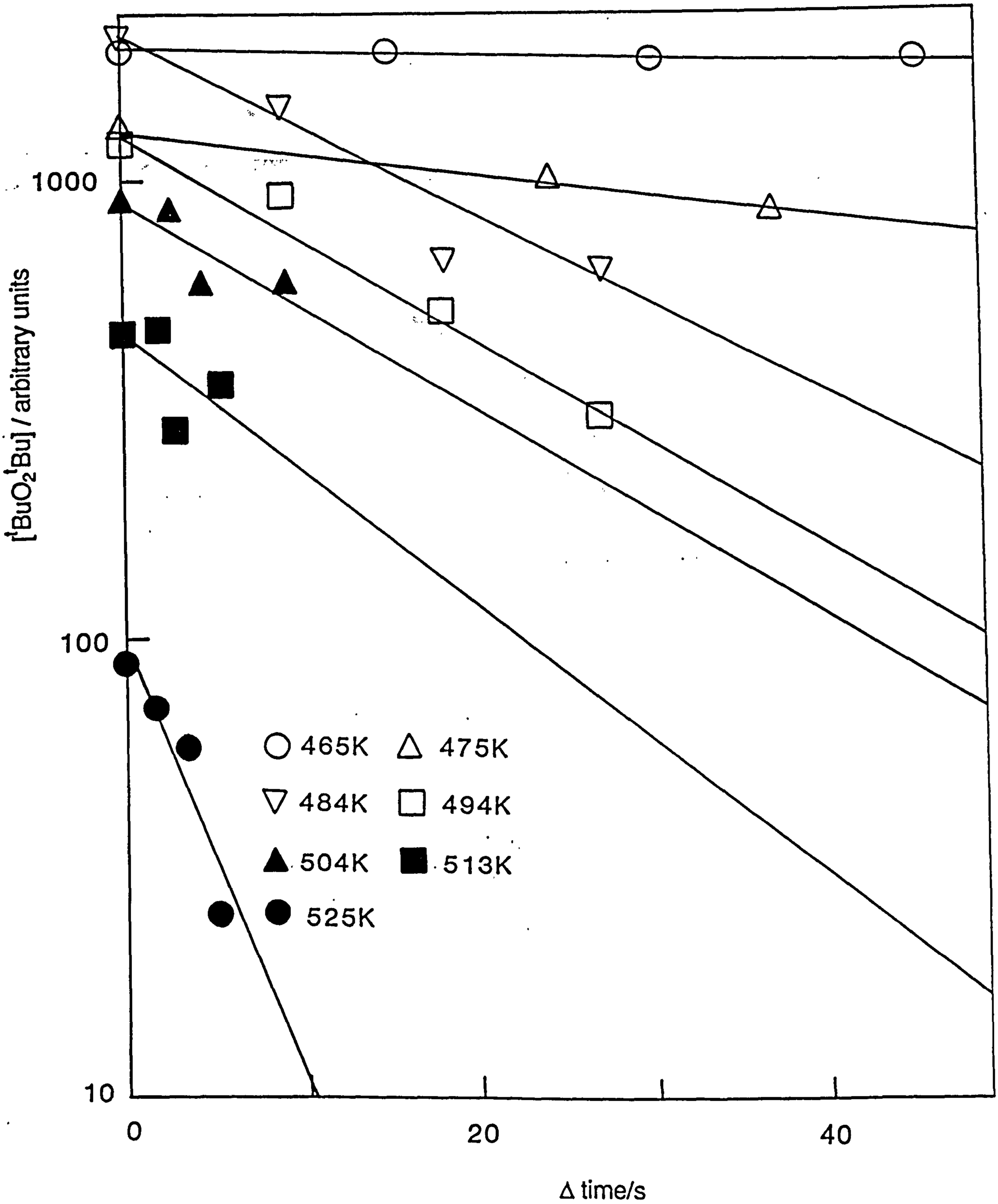

Figure (3.11) Arrhenius plot for the copyrolysis of di-^{n}butyl and di-^{t}butyl peroxides.

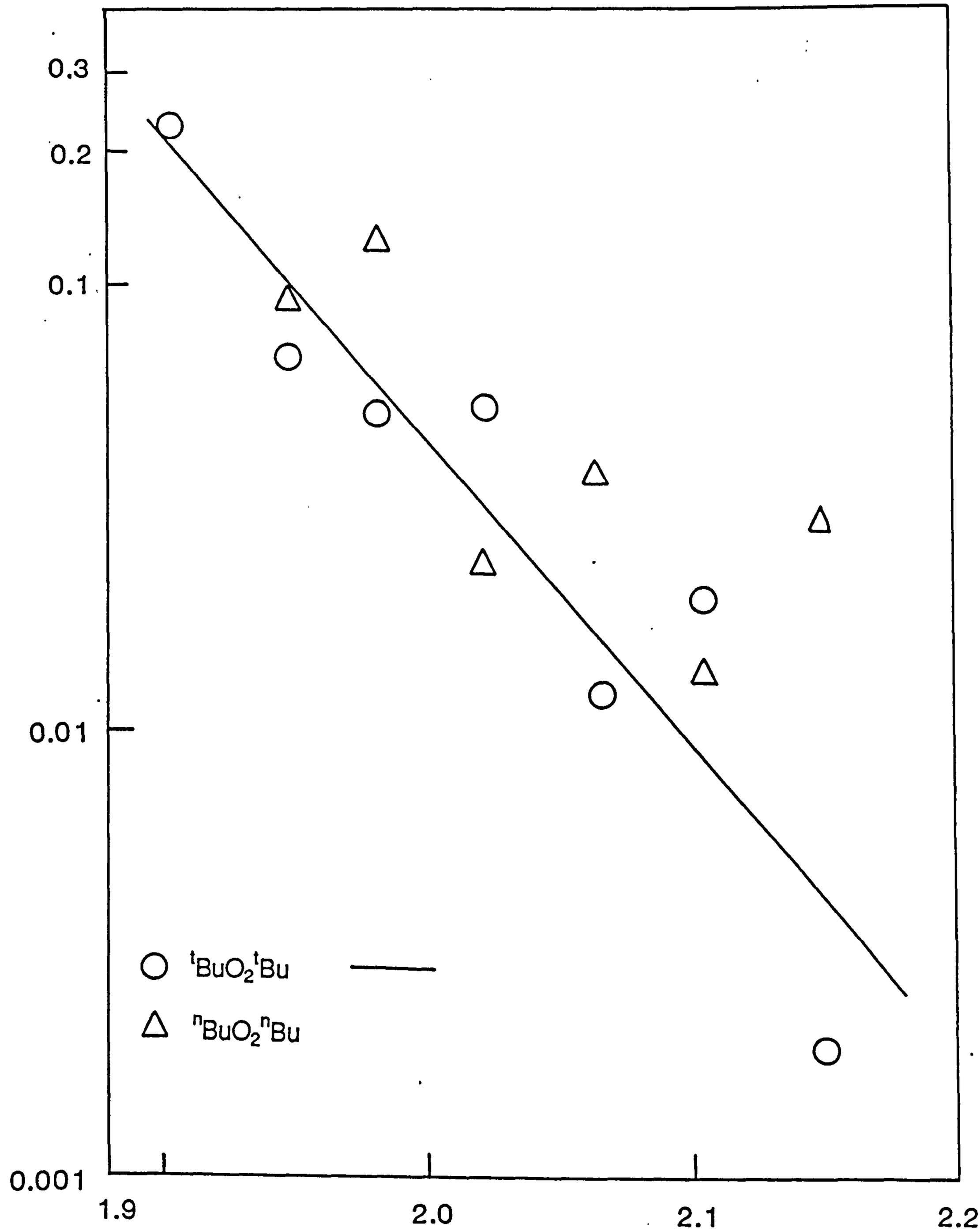

in tables (3.7) and (3.8) and the fractional removal of the ^{n}butoxy radical by decomposition is given by the expression below.

$$e(^{n}BuO\cdot)_{d} = \frac{y(^{n}C_4H_{10}) + y(C_3H_6)}{y(Me_2CO)} \times 14.8$$

The yield ratio values, $y(^{n}C_4H_{10}) + y(C_3H_6)/y(Me_2CO)$, were found, on average, to equal 1/5.1 at 465K, 1/15.8 at 475K, 1/19.5 at 484K, 1/13.6 at 494K, 1/14.5 at 513K and 1/13.2 at 525K and suggest an average value of 1/(13.6 ± 4.8) at, the average temperature, 493K. The value of $\epsilon(^{n}BuO\cdot)_{d}$, at this temperature then is 1.1 ± 0.6 and suggests that between half and, more likely, all of the pyrolyte ^{n}butoxy radicals react by decomposition. This conclusion can not be advanced by the non-observation of any alternative ^{n}butoxy radical reaction products, as both ^{n}butanol and ^{n}butyraldehyde were observed in this study. However, these oxygenates predominantly, or exclusively, occurred via their liquid formations in the bubbler contained di-^{n}butyl peroxide, according to an after-use purity check of this material.

The copyrolysis study of di-^{n}butyl peroxide and di-^{t}butyl peroxide suggests then that the ^{n}butoxy radical, under our experimental conditions, reacted, at least mainly, by decomposition and underwent no isomerization reaction.

Further studies of the ^{n}butoxy radical reactivity were therefore performed, except reverting to single pyrolyte and oxygen containing systems, where the reactions of this radical by decomposition or with oxygen were investigated. Two pyrolytes were employed, first, ^{n}butyl nitrite, that allowed a convenient gas chromatographic analysis of the ^{n}butoxy radical reaction products and, second, di-^{t}butyl peroxide, for the opportunity to measure the pyrolysis kinetics of this

Table (3.7) ^{n}Butane and propene formations in the copyrolysis of di-^{n}butyl and di-^{t}butyl peroxides. Data given in the form, mb ^{n}butane x 10^3, mb propene x 10^3. Values in parenthesis are changes in reaction time in seconds.

Temp.(K)			
465	3.1, 8.7(0)	10.8, 12.7(15.4)	8.9, 9.6(30.9)	7.5, 5.6(46.3)
475	-. 1.7(0)	-, 1.8(13.2)	1.4, 4.5(24.6)	2.3, 6.9(37.8)
484	1.8, 11.1(0)	3.1, 9.7(9.3)	9.9, 8.8(18.6)	5.9, 4.7(27.8)
494	7.9, 11.0(0)	6.4, 10.5(9.1)	11.7, 12.8(18.2)	15.9, 8.4(27.3)
504	-, 50.7(0)	-, 62.1(2.7)	-, 65.9(4.5)	-, 59.7(8.9)
513	7.0, 18.6(0)	5.3, 10.7(1.8)	4.6, 7.1(3.5)	9.1, 7.5(5.3)
525	20.5, 9.6(0)	23.9, 12.1(1.7)	16.3, 8.1(3.4)	21.9, 9.0(5.1)

Table (3.8) Acetone formations in the copyrolysis of di-^{n}butyl and di-^{t}butyl peroxides. Acetone absolute pressures in mb x 10^2. Values in parenthesis are changes in reaction time in seconds.

Temp.(K)				
465	4.6(0)	7.9(15.4)	13.4(30.9)	7.9(46.3)
475	4.8(0)	7.1(13.2)	12.1(24.6)	10.2(37.8)
484	15.8(0)	22.9(9.3)	27.1(18.6)	35.5(27.8)
494	19.4(0)	27.3(9.1)	25.1(18.2)	43.6(27.3)
504	19.1(0)	17.5(2.7)	24.6(4.5)	26.3(8.9)
513	23.0(0)	23.2(1.8)	23.3(3.5)	23.9(5.3)
525	38.8(0)	37.4(1.7)	39.6(3.4)	41.4(5.1)

material. The latter study will be subsequently described.

(3.3.4) The pyrolysis of di-^{n}butyl peroxide.

The pyrolysis of 0.031 mb of di-^{n}butyl peroxide, 38.5 mb oxygen in a 1b helium balance was performed between 462 and 503K.

The first order pyrolysis kinetics of di-^{n}butyl peroxide, at the four temperatures of the study, are shown in figure (3.12), and their Arrhenius variation is shown in figure (3.13), where the equation for the plotted data is given below.

$\log_{10}(k/s^{-1}) = 14.25 \pm 1.44 - (34.1 \pm 3.2)$ kcal mol^{-1}/RT ln 10

The pyrolysis of di-^{n}butyl peroxide has been performed on two previous occasions. First, Pryor[79], in an early investigation, has polymerized styrene, using di-^{n}butyl peroxide as an initiator, and, from the measured polymerization rates at 333 and 353K, determined an approximate Arrhenius equation for this peroxide pyrolysis that is given below.

$\log_{10}(k/s^{-1}) = 14.1 - 34.3$ kcal mol^{-1}/RT ln 10

Second, Rigny[16], in a flow reactor study, has pyrolysed small amounts, ca. 100 ppm, of di-^{n}butyl peroxide in about 400 mb oxygen where, owing to the significant ^{n}butoxy radical reaction with oxygen, hydrogen peroxide was a main product of the pyrolysis.

$$^{n}C_4H_9O_2{}^{n}C_4H_9 \longrightarrow {}^{n}C_4H_9O\cdot + {}^{n}C_4H_9O\cdot$$

$$^{n}C_4H_9O\cdot + O_2 \longrightarrow {}^{n}C_3H_7CHO + HO_2\cdot$$

$$HO_2\cdot + HO_2\cdot + M \longrightarrow H_2O_2 + O_2 + M$$

The di-^{n}butyl peroxide pyrolysis kinetics were determined from the kinetic formations of this peroxide product and are represented in the Arrhenius equation that is given below.

Figure (3.12) First order di-^{n}butyl peroxide decompositions in the pyrolysis of 0.031mb di-^{n}butyl peroxide in 38.5mb oxygen and a 1b helium balance.

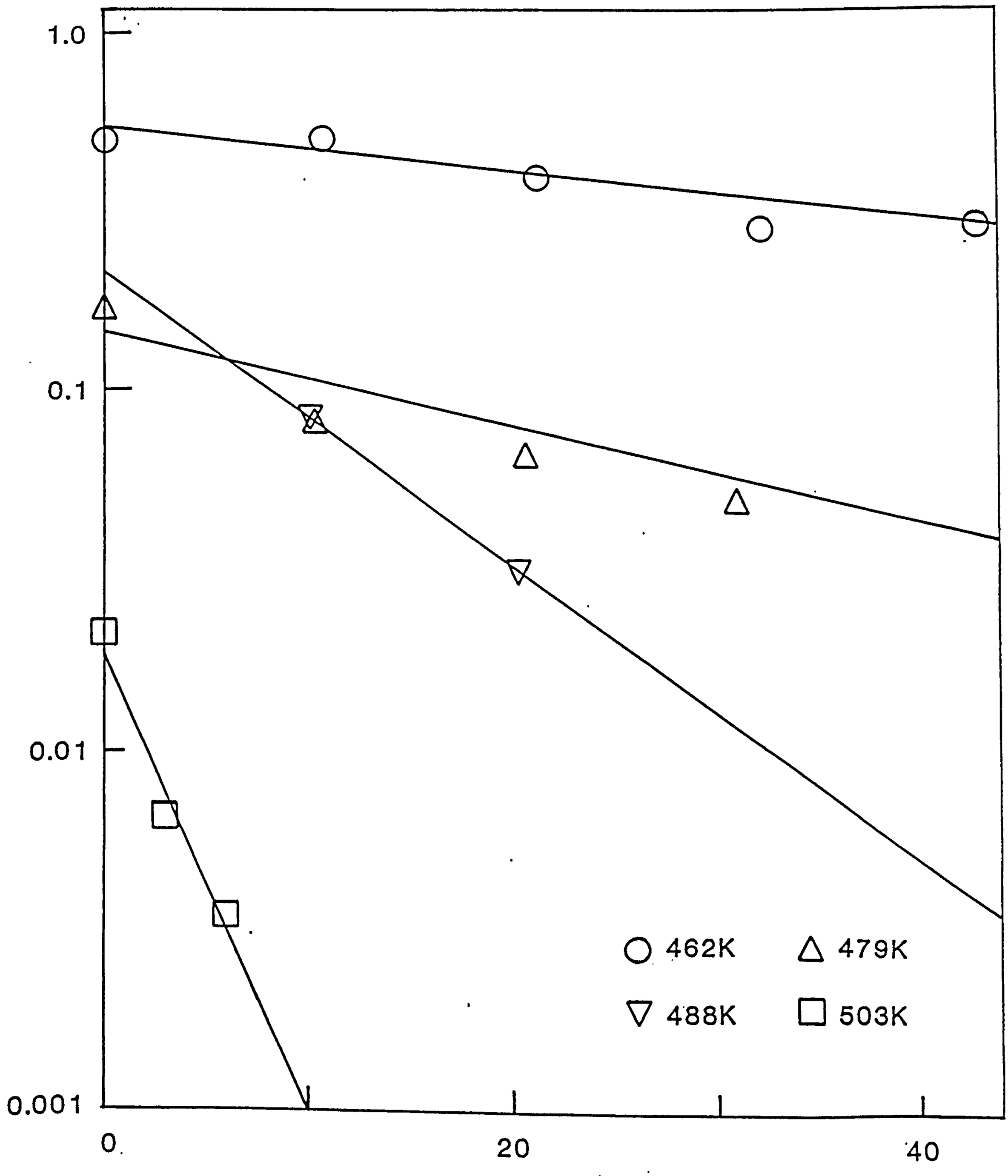

Figure (3.13) Arrhenius plot for the pyrolysis of di-^{n}butyl peroxide.

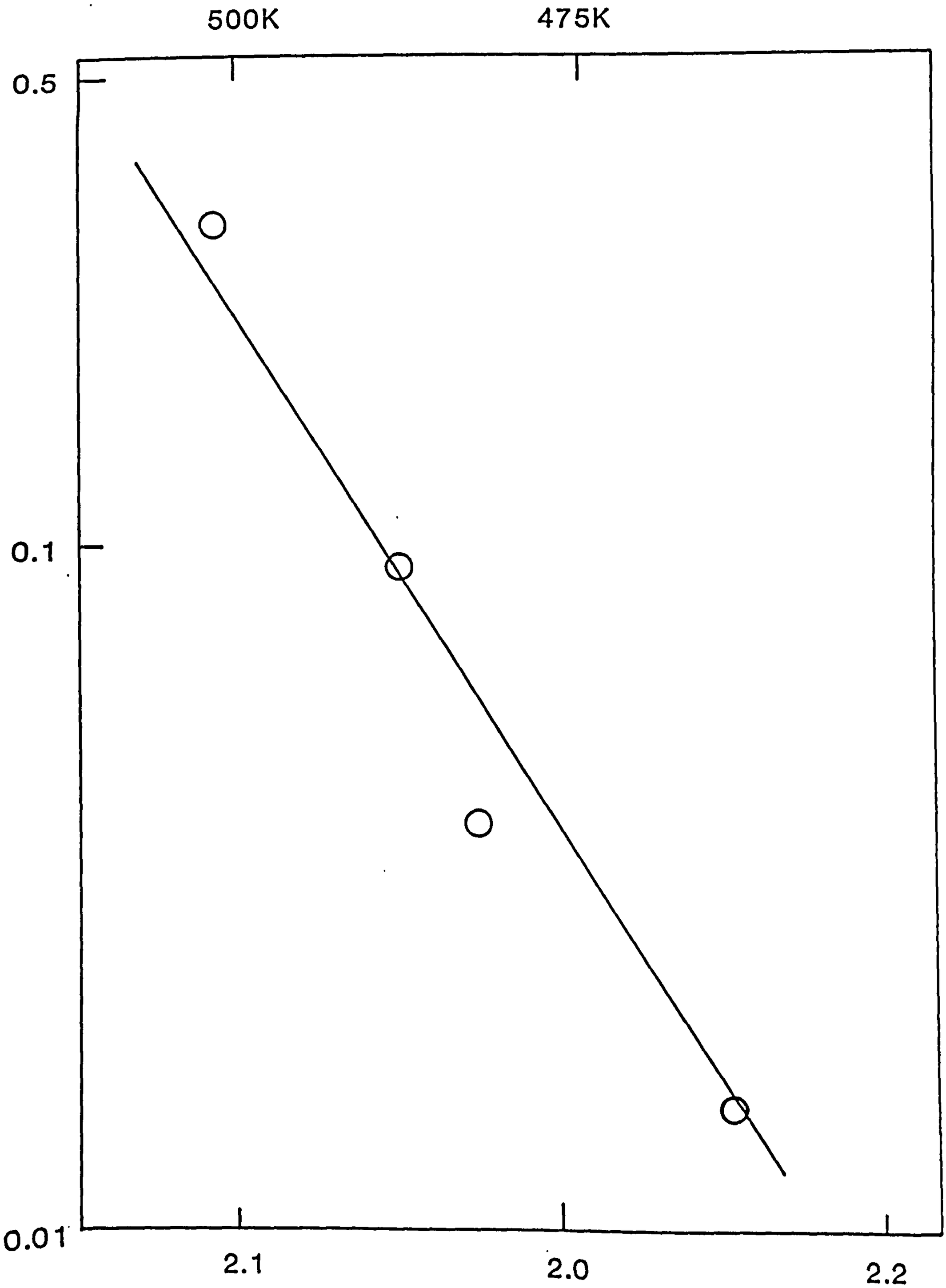

$\log_{10}(k/s^{-1}) = 16.02 \pm 0.49 - (38.3 \pm 2.6)$ kcal mol^{-1}/RT ln 10

The di-^{n}butyl peroxide pyrolysis study performed here is clearly in good kinetic agreement then with the previous kinetic studies of this process.

(3.3.5) The pyrolysis of ^{n}butyl nitrite.

The pyrolysis of 1.39 mb ^{n}butyl nitrite, 38.5 mb oxygen in a 1b helium balance was performed between 490 and 554K.

The pyrolysis of ^{n}butyl nitrite in oxygen occurs to allow the ^{n}butoxy radical to react either by decomposition or with oxygen.

$$^{n}BuONO \longrightarrow {}^{n}BuO\cdot + NO$$

$$^{n}BuO\cdot \longrightarrow {}^{n}Pr\cdot + CH_2O$$

$$^{n}BuO\cdot + O_2 \longrightarrow {}^{n}PrCHO + HO_2\cdot$$

The pyrolysis of ^{n}butyl nitrite was initially performed to determine the ^{n}butyl nitrite decay and ^{n}butyraldehyde formation kinetics and these first order processes are respectively shown in figures (3.14) and (3.15). Figure (3.15) is also footnoted with the estimated ^{n}butyraldehyde concentration values at complete reaction. Figure (3.16) is an Arrhenius plot of these data, where the significance of the broken line will be explained shortly, where the equations for (a) the ^{n}butyl nitrite decompositions and (b) the ^{n}butyraldehyde formations were obtained by a linear regression analysis and are given below.

(a) $\log_{10}(k/s^{-1}) = 8.41 \pm 0.44 - (22.5 \pm 1.1)$ kcal mol^{-1}/RT ln 10

(b) $\log_{10}(k/s^{-1}) = 2.96 \pm 0.58 - (10.1 \pm 1.4)$ kcal mol^{-1}/RT ln 10

Figure (3.14) First order ^{n}butyl nitrite decompositions in the pyrolysis of 1.39mb ^{n}butyl nitrite in 38.5mb oxygen and a 1b helium balance.

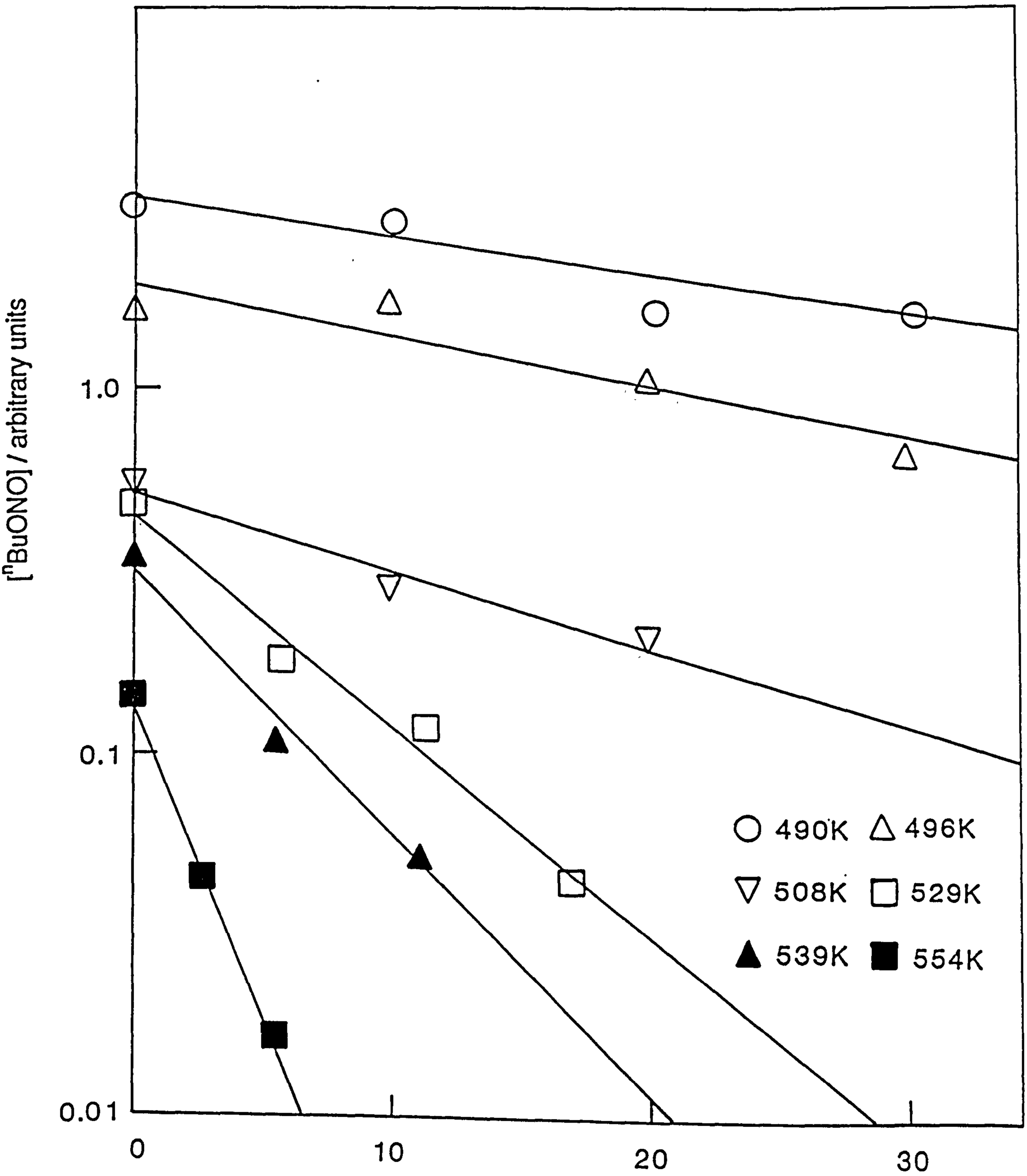

Figure (3.15) First order ^{n}butyraldehyde decompositions in the pyrolysis of 1.39mb ^{n}butyl nitrite in 38.5mb oxygen and a 1b helium balance

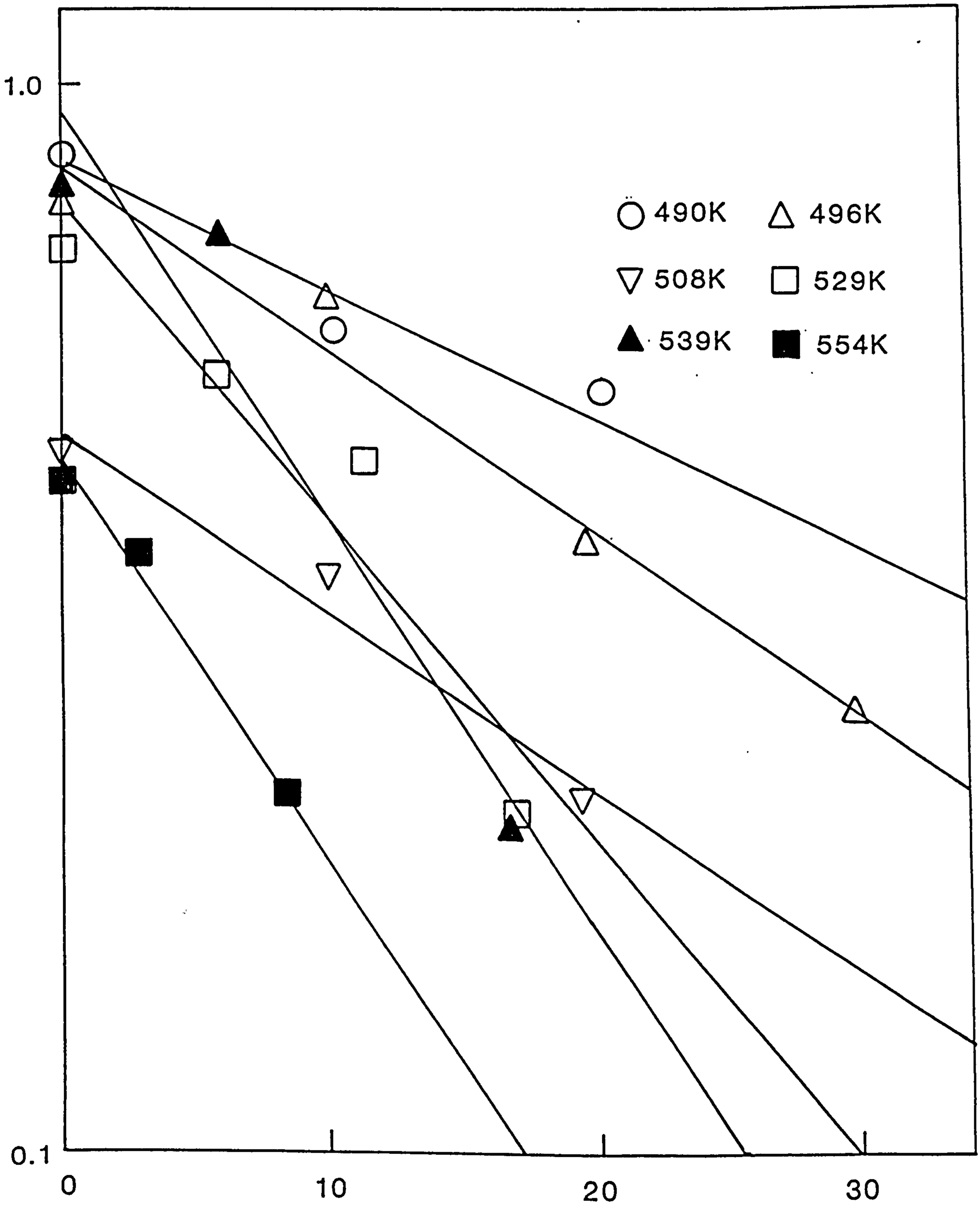

Values of $[^{n}PrCHO]_\infty$ / arbitrary units

33 (490K), 25 (496K), 30 (508K), 30 (529K), 20 (539K), 20 (554K)

Figure (3.16) Arrhenius plot for the pyrolysis of ^{n}butyl nitrite.

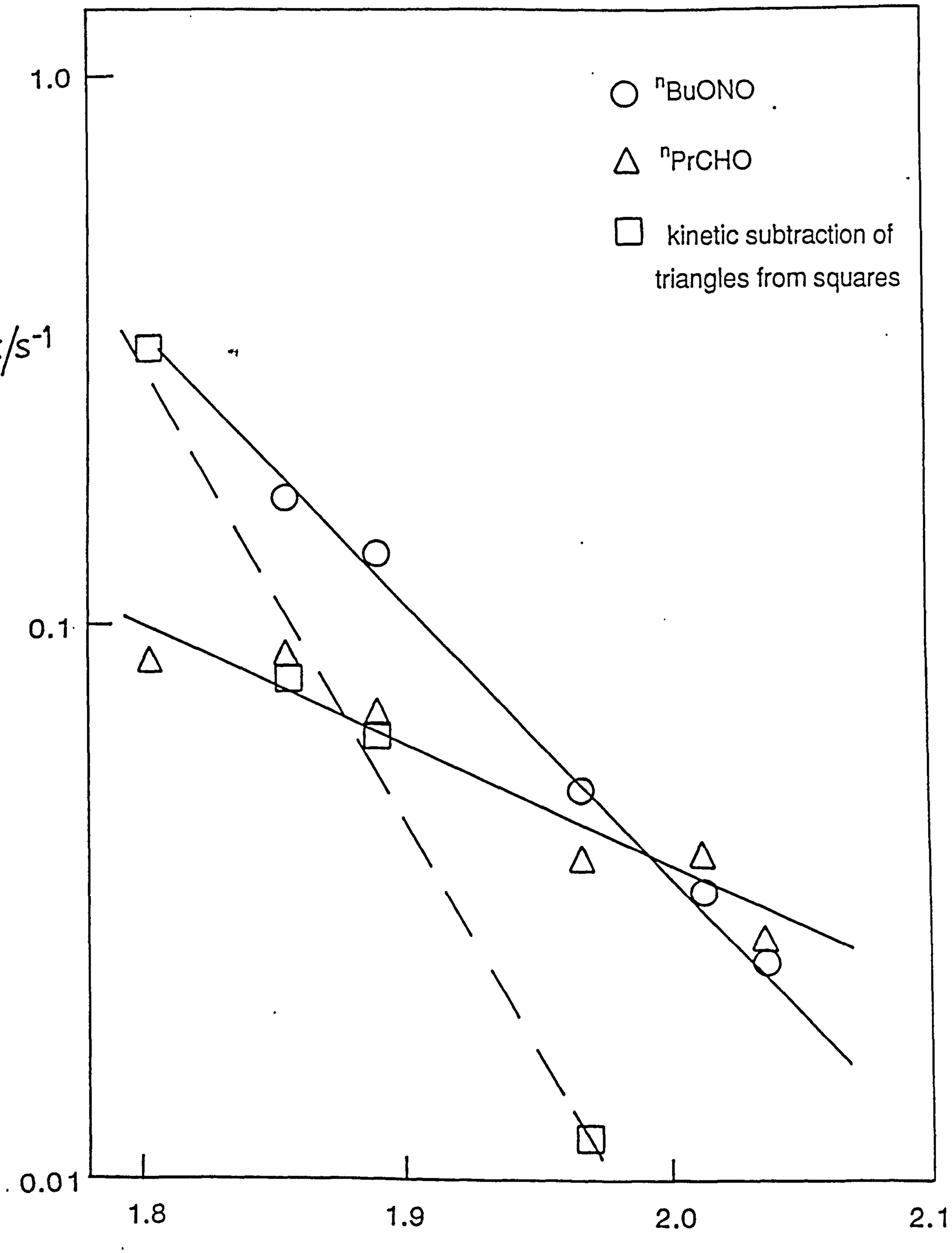

The pyrolysis of ^{n}butyl nitrite occurs then with unexpectedly low Arrhenius parameters that suggest a failure to isolate the pyrolytic homolysis of the ^{n}BuO–NO bond. Consequently an ^{n}butyl nitrite homolysis to give, in parallel, radical and molecular products is suggested.

$$^{n}BuONO \longrightarrow {}^{n}BuO\cdot + NO$$

$$^{n}BuONO \longrightarrow {}^{n}PrCHO + HNO$$

Accordingly, the ^{n}butyl nitrite pyrolysis kinetics, to give radical products, can be determined by a kinetic subtraction of the aldehyde formation from the total nitrite decomposition. The broken line in figure (3.16) shows the result of this process and determines the ^{n}butyl nitrite homolysis, to give radical products, to have approximate Arrhenius parameters of $A \sim 10^{14.5}$ s^{-1} and $E \sim 38$ kcal mol^{-1}. These Arrhenius parameters are supported in the literature[23] and consequently support the double nitrite decomposition idea and, implicitly, also suggest that the ^{n}butoxy radical reacts, predominently at least, by decomposition rather than with oxygen.

The pyrolysis of ^{n}butyl nitrite has been studied on two previous occasions, the first by Steacie[80], in a manometric study between 444 and 485K, where an approximate activation energy of 36 kcal mol^{-1} was reported for this process. Second, Golden[23] has performed the V.L.P.P. of ^{n}butyl nitrite between 590 and 750K, where a R.R.K.M. treatment of the pyrolysis data gave the high pressure limit Arrhenius parametefs for this pyrolysis to be $A = 10^{16.5}$ s^{-1} and $E = 41.0$ kcal mol^{-1}.

The ^{n}butyraldehyde formation may occur either homogenously or heterogenously and in the former case there are two possibilities.

First, a sensitized decomposition of the nitrite that follows the secondary attack of the nitrite α(C–H) bond and, second, a four centre elimination of the aldehyde.

$$^{n}BuONO + X\cdot \longrightarrow {}^{n}PrCHONO + XH$$

$$^{n}PrCHONO \longrightarrow {}^{n}PrCHO\cdot + NO$$

$$^{n}BuONO \longrightarrow {}^{n}PrCHO + HNO$$

The first of these homogenous possibilities appears unlikely from the apparent non–observation, despite the absence of an extensive search, of any cyclic ether secondary products that could, expectedly, be formed in competition with a sensitized ^{n}butyraldehyde formation. The second of these possibilities has been thermochemically considered in comparison with an analogous and hypothetical elimination from ^{i}propyl nitrate.

$$^{n}BuONO \longrightarrow {}^{n}PrCHO + HNO \qquad (a)$$

$$Me_2CHONO_2 \longrightarrow Me_2CO + HNO_2 \qquad (b)$$

We find then that $\Delta H^{o}_{300K}(a) = +38.2$ kcal mol^{-1} and $\Delta H^{o}_{300K}(b) = -23.4$ kcal mol^{-1} [68] and, accordingly, the elimination is less likely from ^{n}butyl nitrate than from ^{i}propyl nitrate, and, therefore, the non–observation of a molecular elimination from the nitrate appears to mitigate against this process in the nitrite case. The pyrolysis of ^{n}butyl nitrite is suggested then to occur with some direct heterogenous ^{n}butyraldehyde formation and this suggestion is supported by a similar pyrolysis study, by Batt[19], except of ^{i}propyl nitrite, where an analogous heterogenous elimination of acetone was reported.

(3.3.6) The pyrolysis of 2-^{n}butoxyethyl nitrate.

The pyrolysis of 2-^{n}butoxyethyl nitrate in oxygen and a 1b helium balance was performed between 483 and 541K, where, to obtain a linear Arrhenius plot for this process, three partial pressures of both the nitrate and oxygen were employed, despite the apparently ubiquitous first order decays of this material.

The pyrolysis of 2-^{n}butoxyethyl nitrate was intially performed using 0.0946 mb 2-^{n}butoxyethyl nitrate and 47.6 mb oxygen, where the nitrate absolute pressure was subsequently reduced to 0.017 and then to 0.0026 mb, at a fixed nitrate to oxygen stoicheometry of 1:500. Figures (3.17) to (3.19) show the first order nitrate decays under these respective conditions and figure (3.20) provides the Arrhenius plots of the nitrate decay kinetics over all of the studied conditions of composition and temperature. The pyrolysis of the largest and intermediate nitrate partial pressures provide curved Arrhenius plots that are consistent with some secondary nitrate decomposition, that is more prevalent at the lower temperatures of the study and therefore not heterogenous in origin. This idea is also supported by the observed increase in the kinetic stability of the nitrate, under isothermal conditions, in the intermediate compared to the largest nitrate partial pressure system. The pyrolysis of 0.0026 mb of 2-^{n}butoxyethyl nitrate provided nitrate decays that could only be measured at the lower end of the stated temperature range due to the difficulties in analysing such small amounts of this material. Fortunately, the measured kinetic decays of the lowest and intermediate nitrate partial pressures, excluding the lowest temperature datum, provide a colinear Arrhenius plot that is shown as the straight line in figure (3.20) and has the following equation.

Figure (3.17) First order 2-^{n}butoxyethyl nitrate decompositions in the pyrolysis of 0.094mb 2-^{n}butoxyethyl nitrate in 1.3mb oxygen and a 1b helium balance.

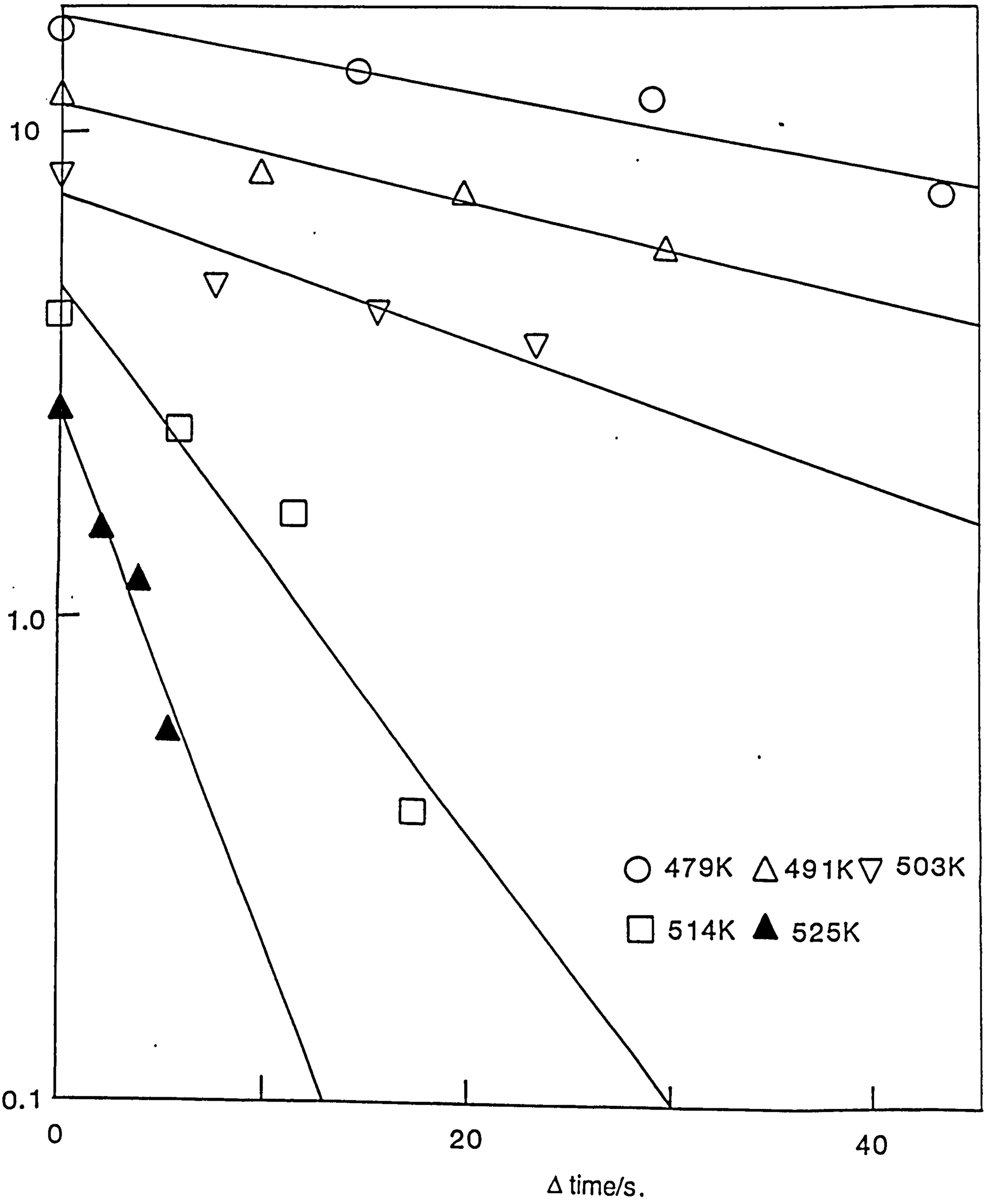

Figure (3.18) First order 2-^{n}butoxyethyl nitrate decompositions in the pyrolysis of 0.017mb 2-^{n}butoxyethyl nitrate in 1.3mb oxygen and a 1b helium balance.

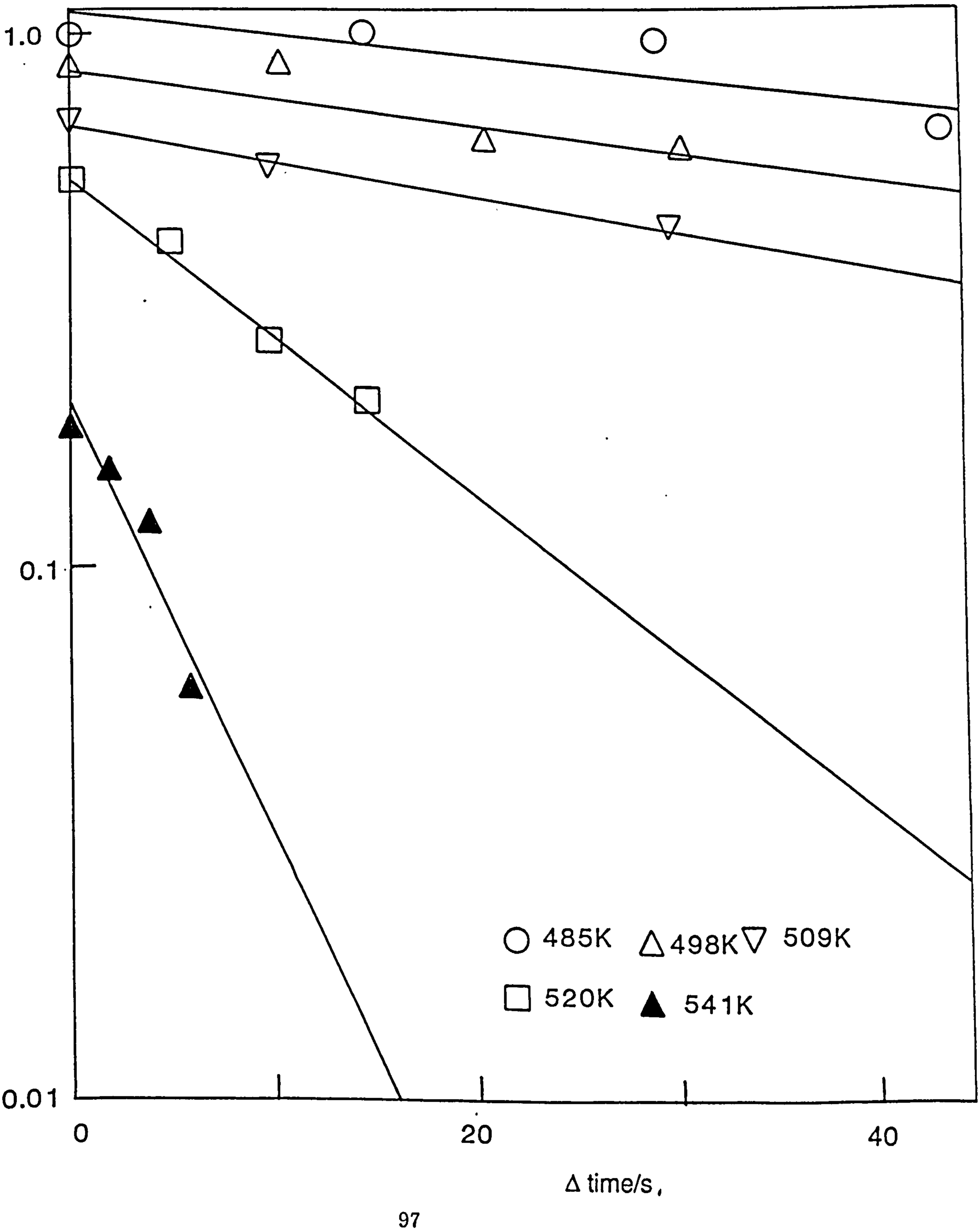

Figure (3.19) First order 2-^{n}butoxyethyl nitrate deompositions in the pyrolysis of 0.0026mb 2-^{n}butoxyethyl nitrate in 1.3mb oxygen and a 1b helium balance.

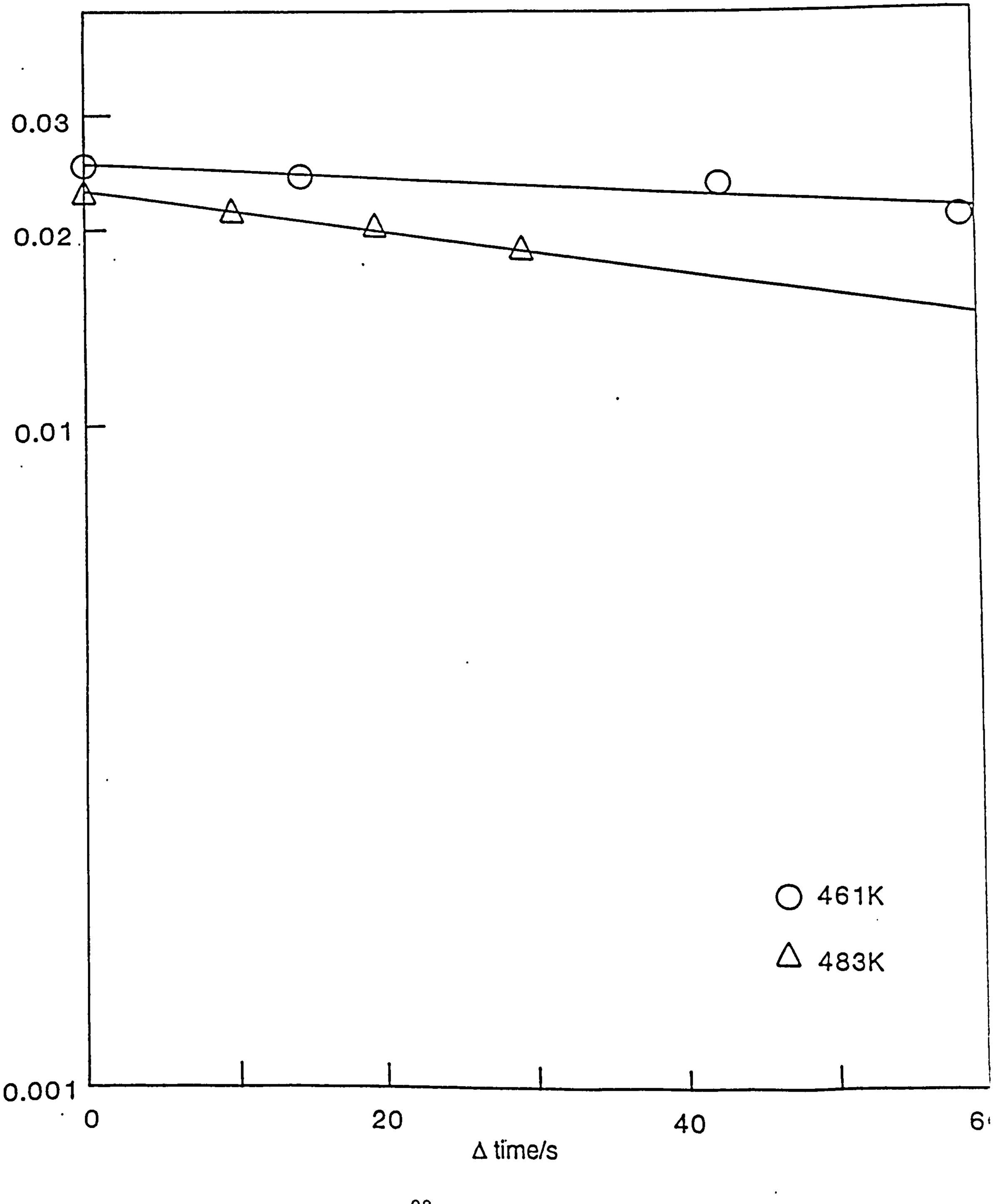

Figure (3.20) Arrhenius plot for the pyrolysis of 2-^{n}butoxyethyl nitrate.

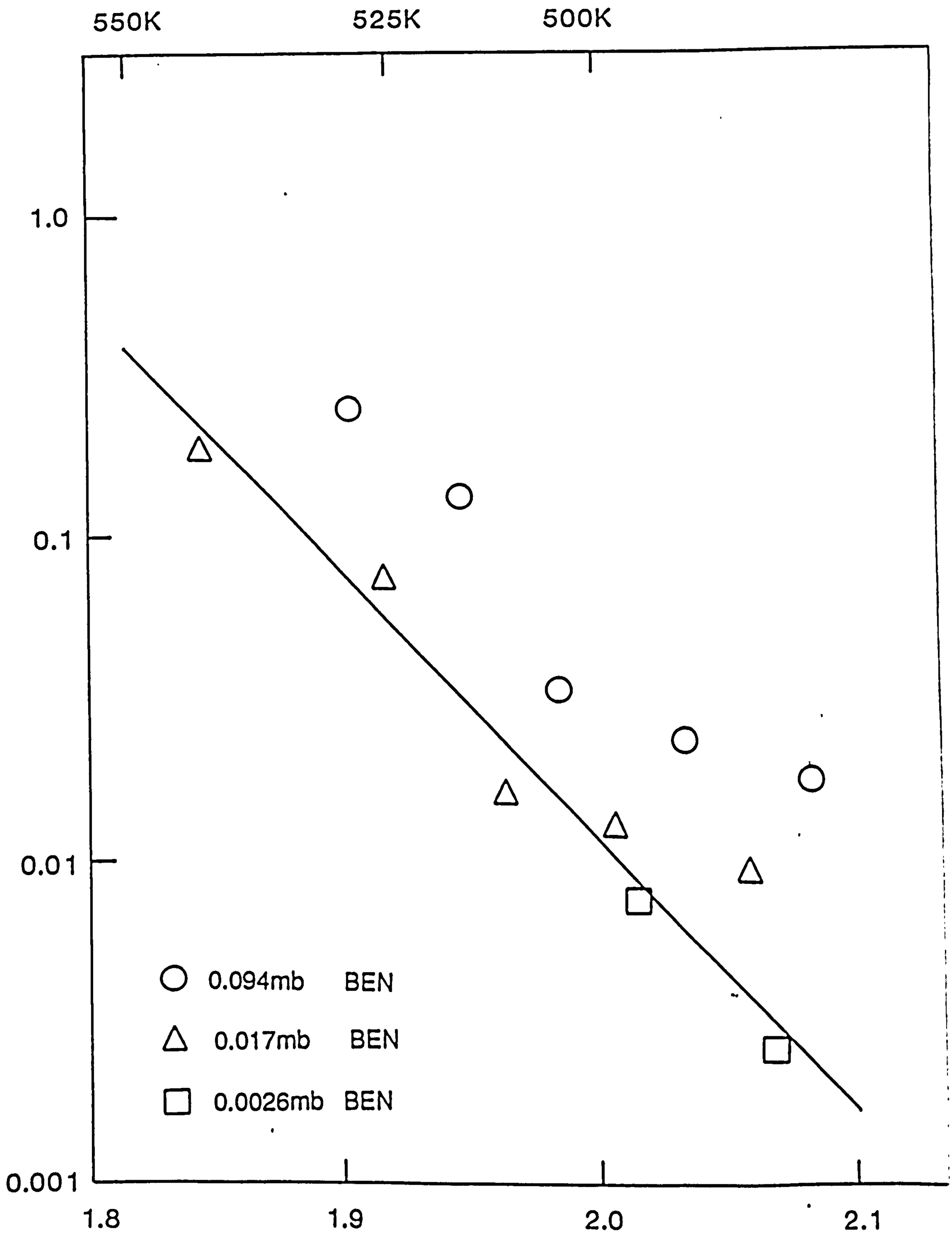

$\log_{10}(k/s^{-1}) = 15.01 \pm 1.39 - (38.9 \pm 3.2)$ kcal mol^{-1}/RT ln 10

The pyrolysis of 2-^{n}butoxyethyl nitrate has not been previously studied. Pritchard[81], however, has measured the pyrolysis kinetics of another long chain nitrate, ^{i}octyl nitrate, between 471 and 517K, and reported the following Arrhenius equation, that is parametrically similar to the comparable equation for the pyrolysis of 2-^{n}butoxyethyl nitrate.

$\log_{10}(k/s^{-1}) = 15.4 - 37.5$ kcal mol^{-1}/RT ln 10

The pyrolysis complications of 2-^{n}butoxyethyl nitrate have been considered to attempt to understand the secondary mechanism operative in this pyrolysis. First, the nitrate is considered to be inert towards both the peroxy radical intermediates and the pyrolyte nitrogen dioxide, by analogy with the reactivities of the many previous and ^{i}propyl nitrate pyrolytes respectively. Second, the initial pyrolyte ^{n}butoxyethoxy radical reactivity was investigated in a failed search for the conjugate alcohol and aldehyde of this radical. The ^{n}butoxyethoxy radical is considered then, by analogy with the previously studied alkoxy radicals, to react by decomposition to give, here, the ^{n}butoxymethyl radical.

$$^{n}C_4H_9OCH_2CH_2ONO_2 \longrightarrow {}^{n}C_4H_9OCH_2CH_2O\cdot + NO_2$$
$$^{n}C_4H_9OCH_2CH_2O\cdot \longrightarrow {}^{n}C_4H_9OCH_2\cdot\ (R\cdot) + CH_2O$$

Subsequently, the ^{n}butoxymethyl radical (R·) is expected to oxygenate, either with or without prior decomposition, to provide for the first step in the classical peroxy radical isomerisation and decomposition mechanism[37], that is invoked here to account for the pyrolysis complications of this study. The 2-^{n}butoxyethyl nitrate undergoes a secondary decomposition then, following the suggested

attack of the hydroxy radical, generated in the above mechanism, on this material.

$^{n}C_4H_9OCH_2\cdot + O_2 \longrightarrow RO_2\cdot$

$^{n}C_4H_9OCH_2\cdot \longrightarrow {}^{n}C_4H_9\cdot\ (R\cdot') + CH_2O$

$R\cdot' + O_2 \longrightarrow R'O_2\cdot$

$RO_2\cdot \quad \text{or} \quad R'O_2\cdot \longrightarrow \cdot QO_2H$

$\cdot QO_2H \longrightarrow \text{Product} + \cdot OH$

$\cdot QO_2H + O_2 \longrightarrow \cdot O_2QO_2H$

$\cdot O_2QO_2H \longrightarrow \text{Product} + \cdot OH$

$^{n}BuOCH_2CH_2ONO_2 + \cdot OH \longrightarrow \cdot Q'ONO_2 + H_2O$

$\cdot Q'ONO_2 \longrightarrow Q'O + NO_2$

(3.3.7) The pyrolysis of ^{t}butyl hydroperoxide.

The pyrolysis of ^{t}butyl hydroperoxide in oxygen was performed in excess helium, where, despite an extensive decomposition of this material, no kinetic decays were observed. The pyrolysis was repeated under conditions that, in comparison with the initial pyrolysis, were varied between a lower temperature, a more cooled sampling probe and a removed fecralloy sheet. The pyrolysis, however, remained complicated, and, apparently, these difficulties originate from a surface decomposition of the hydroperoxide.

The previous pyrolysis studies of hydroperoxides have generally failed to isolate the homolyses of these materials that, instead, decomposed by extensive surface or secondary processes[7]. Two studies, however, have surmounted these difficulties. First, Benson[82] has performed the V.L.P.P. of ^{t}butyl hydroperoxide and reported the Arrhenius equation for this process to be $\log_{10}(k/s^{-1}) = 15.6 \pm 0.5$ –

42.2 kcal mol^{-1}/RT ln 10. Second, Rigny[83], more recently, has performed the independent pyrolyses of 1-heptyl and 2-heptyl hydroperoxides in mixtures of hydrogen and oxygen. The 1-heptyl and 2-heptyl hydroperoxide pyrolyses occurred by first order kinetics under these mixture conditions, where the pyrolyte hydroxy radical was converted to the hydroperoxy radical. The hydroperoxy radical kinetic formations were measured between 523 and 633K and provided the following Arrhenius equations for the pyrolyses of (a) 1-heptyl and (b) 2-heptyl hydroperoxide.

(a) $\log_{10}(k/s^{-1}) = 16.0 \pm 0.1 - (43.5 \pm 1.0)$ kcal mol^{-1}/RT ln 10

(b) $\log_{10}(k/s^{-1}) = 15.8 \pm 0.2 - (41.5 \pm 1.0)$ kcal mol^{-1}/RT ln 10

(3.4) CONCLUSIONS

The low temperature pyrolyses of a variety of ignition improvers have been performed under first order conditions, of low pyrolyte concentrations and oxygen presence, where the pyrolysis kinetics of these materials were measured and the chemistries of the initial pyrolyte alkoxy radicals were investigated. Table (3.9) summarises the measured pyrolysis kinetics of these ignition improvers by recording the Arrhenius parameters for the decompositions of these materials. Table (3.9) also includes the thermochemical kinetic activation energies, E, for the ignition improver homolyses, that have been estimated, in each case, by the following procedure.

(1) The standard heat of pyrolysis at 300K, ΔH_{300K}, was calculated using group additivity rules[68]. (2) The standard heat of pyrolysis at the mean temperature, T, of the study, ΔH_T, was calculated from the result of (1), using the group additivity value of the average heat

capacity change between this temperature and 300K[68]. (3) E is then given by ΔH_T^o - RT. Table (3.9) generally shows a good agreement between these experimental and thermochemical kinetic activation energies and thereby confirms our low temperature pyrolyses to have successfully isolated the weakest bond homolysis of the studied ignition improvers.

The pyrolyses of a range of ignition improvers, that were autoignition studied by Kirsch and Selby, under low temperature conditions allow the relative autoignition performances of this improver range to be understood from both the pyrolysis kinetics and initial pyrolyte alkoxy radical chemistries of these materials.

The low temperature pyrolyses of these ignition improvers suggest that, in the studies of Kirsch and Selby, the decompositions of these materials are, in the initial autoignition condition, possibly and certainly complete at, respectively, 650 and 760K. The ignition improver order of effectiveness is, however, equivalent at both of these temperatures and is, therefore, independent of the pyrolysis kinetic differences between these materials. The pyrolysis kinetics of the ignition improvers are not, however, unimportant on this account but are, in each case, sufficiently rapid to maintain that the behavioural differences between these materials owe to the respective chemistries of the radical fragments they decompose to provide.

The low temperature ignition improver pyrolysis studies have investigated the chemistries of the initial pyrolyte alkoxy radicals, where the decomposition reaction, to provide an alkyl radical, was ubiquitously found. These pyrolyte alkoxy radicals are then, at autoignition temperatures, certain to react, perhaps exclusively, by decomposition, and the behavioural ignition improver differences can

Table (3.9) Summary of Arrhenius parameters for the pyrolyses of ignition improvers in oxygen

Ignition Improver	$\log_{10}(A/s^{-1})_{expt}$	$E/kcal\ mol^{-1}{}_{expt}$	Average Temp. of study/K	$\Delta H^{o}_{300}/kcal\ mol^{-1}$	$E/kcal\ mol^{-1}{}_{calc.}$
$^{t}BuO_2{}^{t}Bu$	15.03 ± 0.69	36.1 ± 1.5	487	39.2	38.2
$^{t}BuO_2Cu$	14.74 ± 0.87	34.3 ± 1.9	471	-	-
$^{n}BuO_2{}^{n}Bu$	14.25 ± 1.44	34.1 ± 3.2	483	37.9	36.9
$^{n}BuONO$	~ 14.5	~ 38	522	42.1	41.1
Me_2CHONO_2	14.56 ± 1.69	37.4 ± 4.0	517	43.0	42.0
$^{n}BuOCH_2CH_2$- $-ONO_2$	15.01 ± 1.39	38.9 ± 3.2	512	42.3	41.2

be understood, here, from the oxidation differences between these double pyrolyte alkyl radical products.

Alkyl radicals oxidize to give products that depend on the original radical structure and those that are four or more carbon atoms long will, under autoignition conditions, oxidize by the peroxy radical isomerization and decomposition mechanism[37], to give the hydroxy radical. Accordingly, the pyrolyses of the studied ignition improvers provide, after the double decomposition of the pyrolyte and daughter alkoxy radicals, alkyl radicals that can, in the unique case of 2-^{n}butoxyethyl nitrate, be oxidized to give the hydroxy radical. The 2-methoxyethyl nitrate surrogates and both di-^{t}butyl peroxide and ^{i}propyl nitrate provide, correspondingly, ^{n}propyl and methyl radicals that would oxidize to give self reacting peroxy radicals rather than the aforeformed hydroxy radical. Evidently, the pyrolysis of 2-^{n}butoxyethyl nitrate, in oxygen, uniquely provides the hydroxy radical, from the unparalleled non-Arrhenius pyrolysis kinetics of this material, and these pyrolysis studies understand the following activity order of the considered ignition improvers.

BEN > MEN

DTBP

IPN

CHAPTER 4 THE EFFECTS OF NITROGEN OXIDES ON HYDROCARBON AUTOIGNITION

(4.1) INTRODUCTION

This chapter concerns a study of the independent effects of nitrogen dioxide and nitric oxide on hydrocarbon autoignition, performed using the Thornton rapid compression machine (r.c.m.), where the lower oxide was examined as a considered product of the higher oxide effected autoignitions. Two similar studies have previously been performed at Thornton and both investigated the ignition improving behaviour of organic nitrates. First[84], an earlier r.c.m. study showed that 800 ppm of ^{i}propyl nitrate was about twice as effective as an equivalent nitrogen dioxide mole fraction in reducing the ignition delay of a primary reference fuel (P.R.F.), composed of 70% ^{i}octane and 30% ^{n}heptane, in a 10% oxygen containing gas mixture at 650K. Second[85], a research diesel engine study showed that up to 500 ppm aspirated nitrogen dioxide continually shortened the ignition delay of a 41 cetane number fuel, nitrogen dioxide, air mixture at ~ 750K. Subsequently, 2-^{n}butoxy-ethyl nitrate was added to this fuel and an addition of only 50 ppm caused these fuel, air mixtures to autoignite with the same delay as that caused by the 500 ppm nitrogen dioxide addition. These earlier studies suggest then that the ignition improving activity of an organic nitrate derives mainly from the alkoxy rather than the nitrogen dioxide moiety of this material.

The autoignition studies of this chapter will allow the studied effects, by Kirsch and Selby, of organic nitrates on hydrocarbon autoignition to be understood from the role of the nitrogen dioxide produced in the pyrolysis of these materials. The concluding chapter will combine the behavioural ignition improver understandings, based on both the low temperature pyrolyses of these materials and on these autoignition studies, to understand this behaviour of a wide variety of materials that include organic nitrates, peroxides and nitrites.

(4.2) EXPERIMENTAL

The effects of nitrogen dioxide and nitric oxide on hydrocarbon autoignition have been studied using a primary reference fuel, a blend of 90% ^{i}octane and 10% ^{n}heptane with a research octane number (R.O.N.) of 90, chosen for its well characterized autoignitability. The autoignition experiments were conducted using the Thornton r.c.m., under premixed rather than diesel injection conditions, that was described in Chapter 2.

The autoignitions of R.O.N. 90, oxygen, nitrogen oxide, diluent mixtures, that varied only in the nitrogen oxide mole fraction in the total mixture, have been characterized and were prepared in the r.c.m. cell according to the following procedure. (1) The cell was evacuated and then filled to 1b with a flowing mixture of 20% oxygen in a variety of diluents that included carbon dioxide, nitrogen or argon, or bimixtures thereof, according to the desired end of compression temperature (e.o.c.t.). (2) 25 mg of R.O.N. 90 were syringe injected into the septum capped cell. This provided cell mixtures that were always 1.64% in R.O.N. 90 at a stoicheiometry

with oxygen of 0.7. A cell wall temperature of 373K ensured the evaporation of the R.O.N. 90 fuel before the cell mixture was compressed. No mixing time delays were required between the mixture preparation and compression. (3) Nitrogen dioxide was included in the cell mixtures by the gaseous syringe injection of a room temperature equilibrium mixture of two thirds dinitrogen tetroxide and one third nitrogen dioxide rather than as a flow component at stage (1), where condensation losses may have occurred. The injected equilibrium mixture of nitrogen dioxide and dinitrogen tetroxide adjusted under the cell conditions to give entirely nitrogen dioxide at a concentration of 100 ppm per 25.7 μl of the injected mixture. (4) Nitric oxide was included in the cell mixtures as a flow component of stage (1).

The nitric oxide introduction was potentially complicated by the termolecular oxidation of this gas to nitrogen dioxide.

$$NO + NO + O_2 \longrightarrow NO_2 + NO_2$$

Accordingly, the nitric oxide lifetime was calculated, under the cell conditions, where the pseudo second order rate constant for this reaction is 3.17×10^2 M^{-1} s^{-1} [86]. The lifetime of the maximum mole fraction, 800 ppm, of nitric oxide then is 5.8 hours and affirms the negligence of this oxidation reaction.

The autoignitions of the diluted R.O.N. 90, oxygen containing mixtures, both per se and nitrogen oxide included, were studied under fixed conditions of fuel to oxygen stoicheiometry (0.7), oxygen mole fraction (0.2), cell precompression temperature and pressure (373K and 1b respectively) and compression ratio (9.6:1). The autoignition variations of the R.O.N. 90 containing mixtures were studied then according to only the e.o.c.t. and the nitrogen oxide

mole fraction in the overall mixture as the fixed conditions all invariably contributed to the character of these processes[87].

Finally, a significant number of the observed autoignitions in this study were non-uniform in nature. These autoignitions are a known artefact of r.c.m. experiments[87] and are believed to be caused by scavenged cell wall particles that subsequently become hot spots in the compressed gas charge. Non-uniform autoignitions were recognized from their uniform counter-parts by their marked autoignition ease and were discarded from this study.

(4.3) RESULTS

The autoignition characteristics of 1.64% R.O.N. 90, 20% oxygen, 1b diluent balance mixtures were initially reproduced, without any nitrogen oxide inclusion, against a previous study[87], to both validate the experimental method and to provide a comparator for the autoignition characteristics of the R.O.N. 90, oxygen, nitrogen oxide, diluent mixtures. The autoignitions of all of the R.O.N. 90 containing mixtures were pre-conditioned by a rapid elevation of the mixture temperature and were manometrically followed with time. The ignition delay measurement from this pressure-time record, as the defining autoignition characteristic, and the variety of autoignition phenomena observed under these conditions, were described in Chapter 1.

The autoignition characteristics of the 1.64% R.O.N. 90, 20% oxygen, 1b diluent balance mixtures are shown as the solid line of figure (4.1), which is a pseudo Arrhenius plot of the total measured ignition delay versus the e.o.c.t., that was simply calculated from the e.o.c.p. using the ideal gas law. These measured ignition delays are in agreement with the previous study, in all cases, to ± 10%.

Figure (4.1) Ignition delay of 1.64% R.O.N. 90, 20% oxygen, various nitrogen dioxide mole fraction, 1b diluent balance mixtures versus reciprocal temperature.

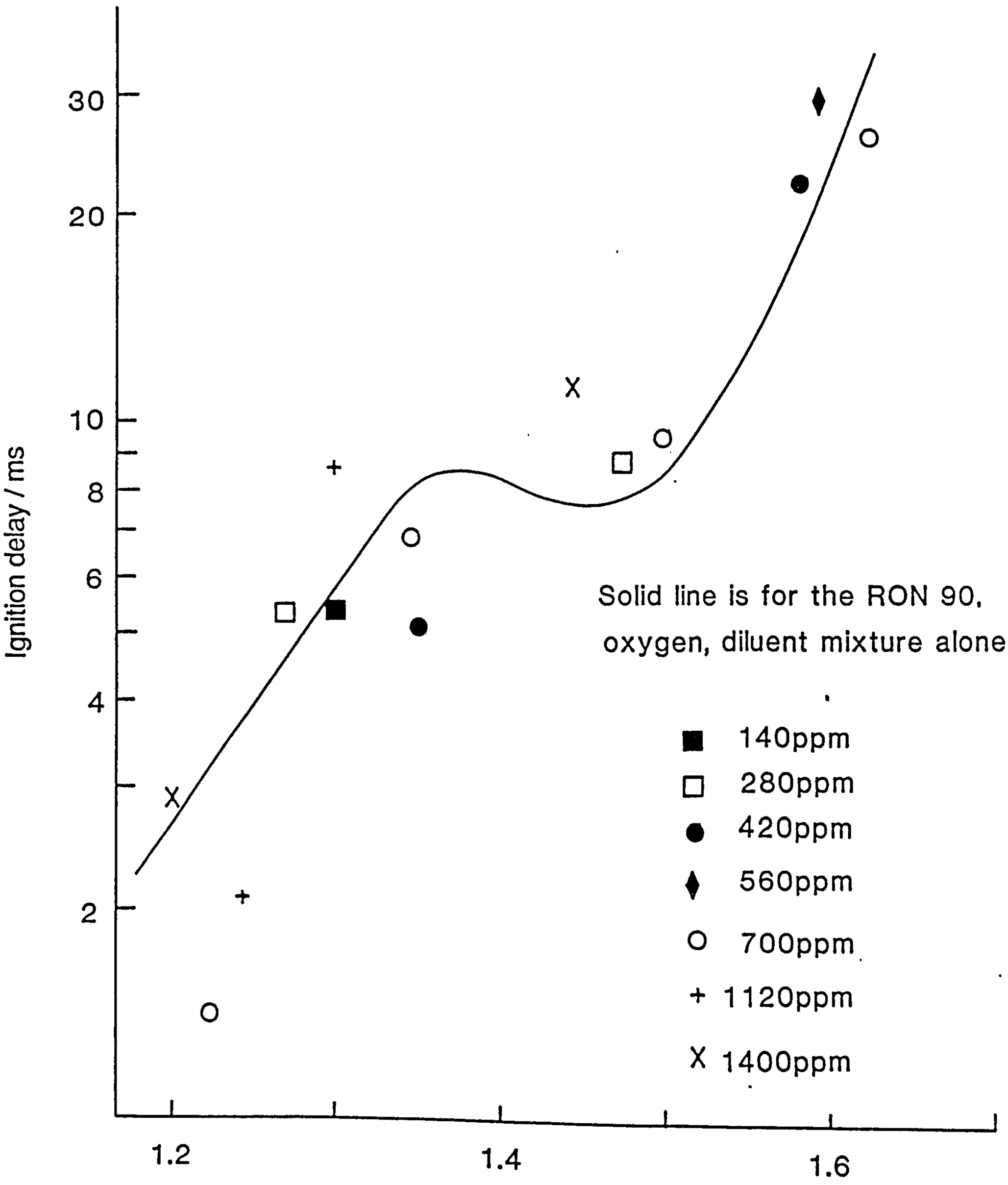

The autoignitions of the R.O.N. 90, oxygen, diluent mixtures were found to occur through an intermediate cool flame between 660 and 725K. Below 660K, the cool flame was indiscernible from the rapidly proceeding hot ignition, and above 725K, there was no cool flame occurrence at all.

The autoignition characteristics of 1.64% R.O.N. 90, 20% oxygen, nitrogen dioxide, 1b diluent balance mixtures, that included various nitrogen dioxide mole fractions, up to 1400 ppm, were subsequently studied and the measured ignition delays of these mixtures are also shown in figure (4.1).

The ignition delays of these R.O.N. 90 containing mixtures, that included nitrogen dioxide, and the R.O.N. 90 containing comparator mixtures, that absented this oxide, are best compared over a temperature range by recourse to the fractional parameter, $\Delta t/t = (t'-t)/t$, where t' and t are the respective ignition delays of these mixtures. Figure (4.2) is a plot of the fractional ignition delay of the R.O.N. 90 and nitrogen dioxide containing mixtures versus the nitrogen dioxide mole fraction of inclusion at four mean e.o.c.t.'s, each of variation ± 15K. At both 623 and 667K, the fractional ignition delays of the modified mixtures increase in monotonic sympathy with the nitrogen dioxide mole fraction of inclusion, although qualitatively, these comparative variations are less at the higher than the lower temperature. At both 762 and 812K, the R.O.N. 90 and nitrogen dioxide containing mixtures, that included only small nitrogen dioxide mole fractions, autoignite with negative fractional ignition delays that vary less than proportionately with the nitrogen dioxide mole fraction of inclusion. Consequently, increasing nitrogen dioxide inclusions in these mixtures eventually produced

Figure (4.2) Fractional ignition delays of mixtures of 1.64% R.O.N. 90, 20% oxygen, various nitrogen dioxide mole fraction, 1b diluent balance mixtures versus nitrogen dioxide mole fraction.

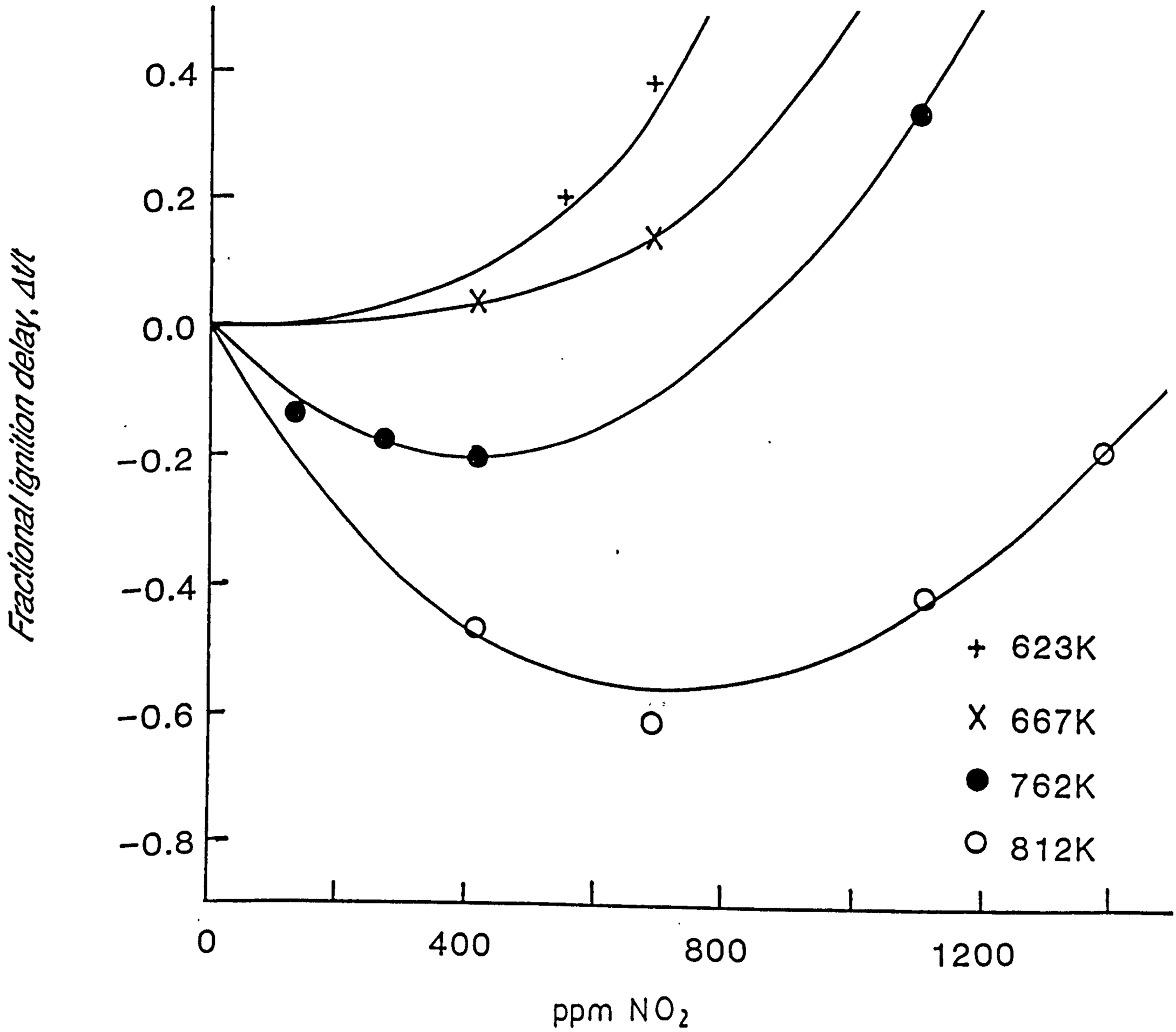

no further fractional decrease in the modified ignition delay and actually caused this quantity to increase. At 762 and 812K then, the modified mixtures show fractional ignition delays with optima shortenings on including various nitrogen dioxide mole fractions and, additionally, the corresponding optima nitrogen dioxide mole fractions increase in sympathy with temperature.

Finally, it was found that the R.O.N. 90, oxygen, nitrogen dioxide, diluent mixtures always autoignited, even with the smallest nitrogen dioxide mole fraction of addition, of 140 ppm, in a single stage with, unlike the R.O.N. 90 containing comparator mixtures, no cool flame occurrence.

The autoignition characteristics of 1.64% R.O.N. 90, 20% oxygen, nitric oxide, 1b diluent balance mixtures, that included various nitric oxide mole fractions, up to 800 ppm, have also been studied. Figure (4.3) is a pseudo Arrhenius plot of the ignition delays of these R.O.N. 90 and nitric oxide containing mixtures between 645 and 860K, where the solid line again represents the autoignition characteristics of the R.O.N. 90 containing comparator mixtures.

Figure (4.4) shows the more useful fraction ignition delay variations of the R.O.N. 90 and nitric oxide containing mixtures, versus the nitric oxide mole fraction of inclusion at four mean temperatures, each of variation ca. ± 5K. Despite the considerable scatter shown in figure (4.4), that probably owes to the inaccuracies in including the nitric oxide in these mixtures, the modified ignition delays qualitatively show the same variations with both temperature and nitrogen oxide mole fraction of inclusion as observed in the R.O.N. 90 and nitrogen dioxide containing mixtures.

Figure (4.3) Ignition delay of 1.64% R.O.N. 90, 20% oxygen, various nitric oxide mole fraction, 1b diluent balance mixtures versus reciprocal temperature.

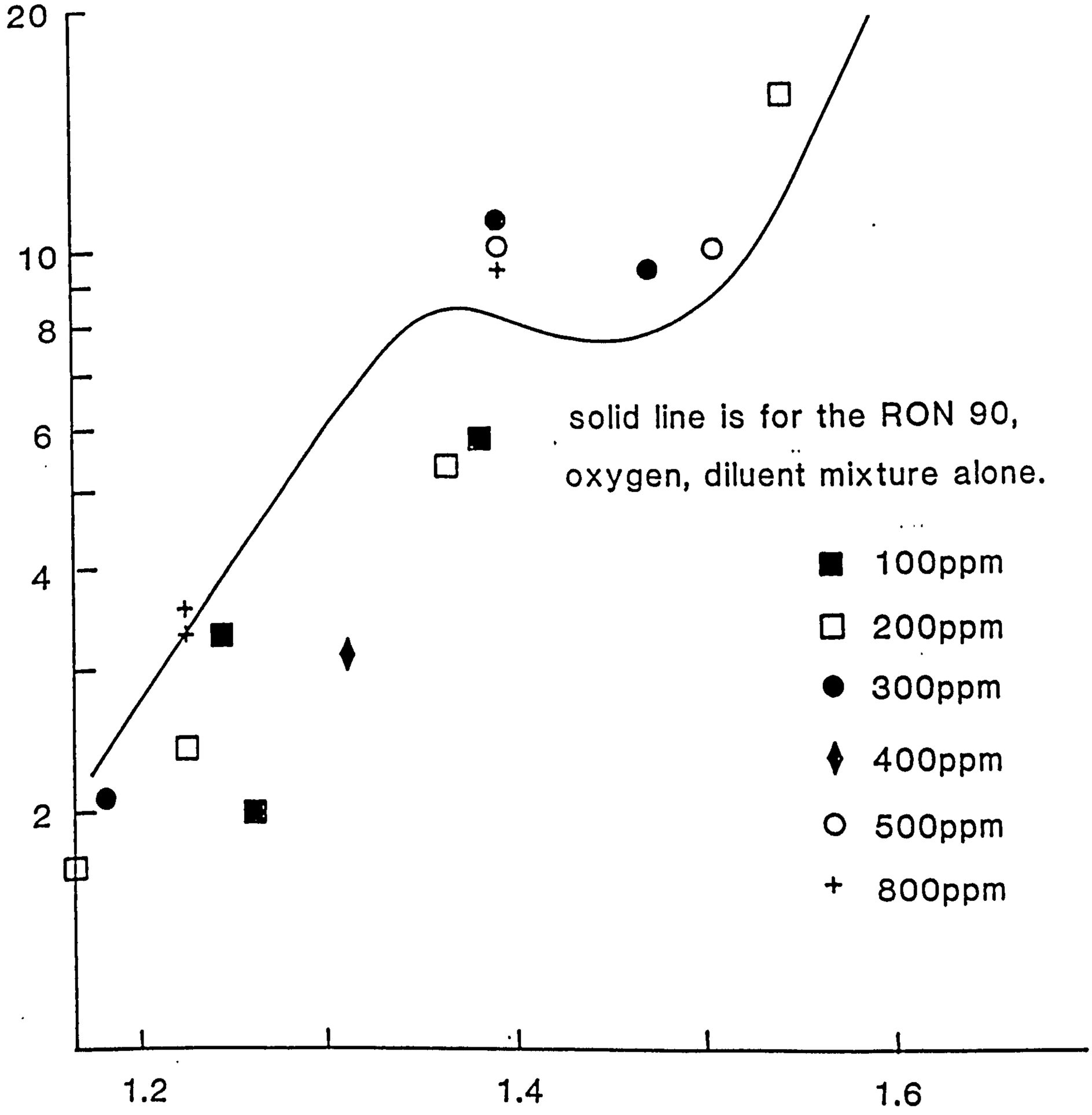

Figure (4.4) Fractional ignition delays of 1.64% R.O.N. 90, 20% oxygen, various nitric oxide mole fraction, 1b diluent balance mixtures versus nitric oxide mole fraction.

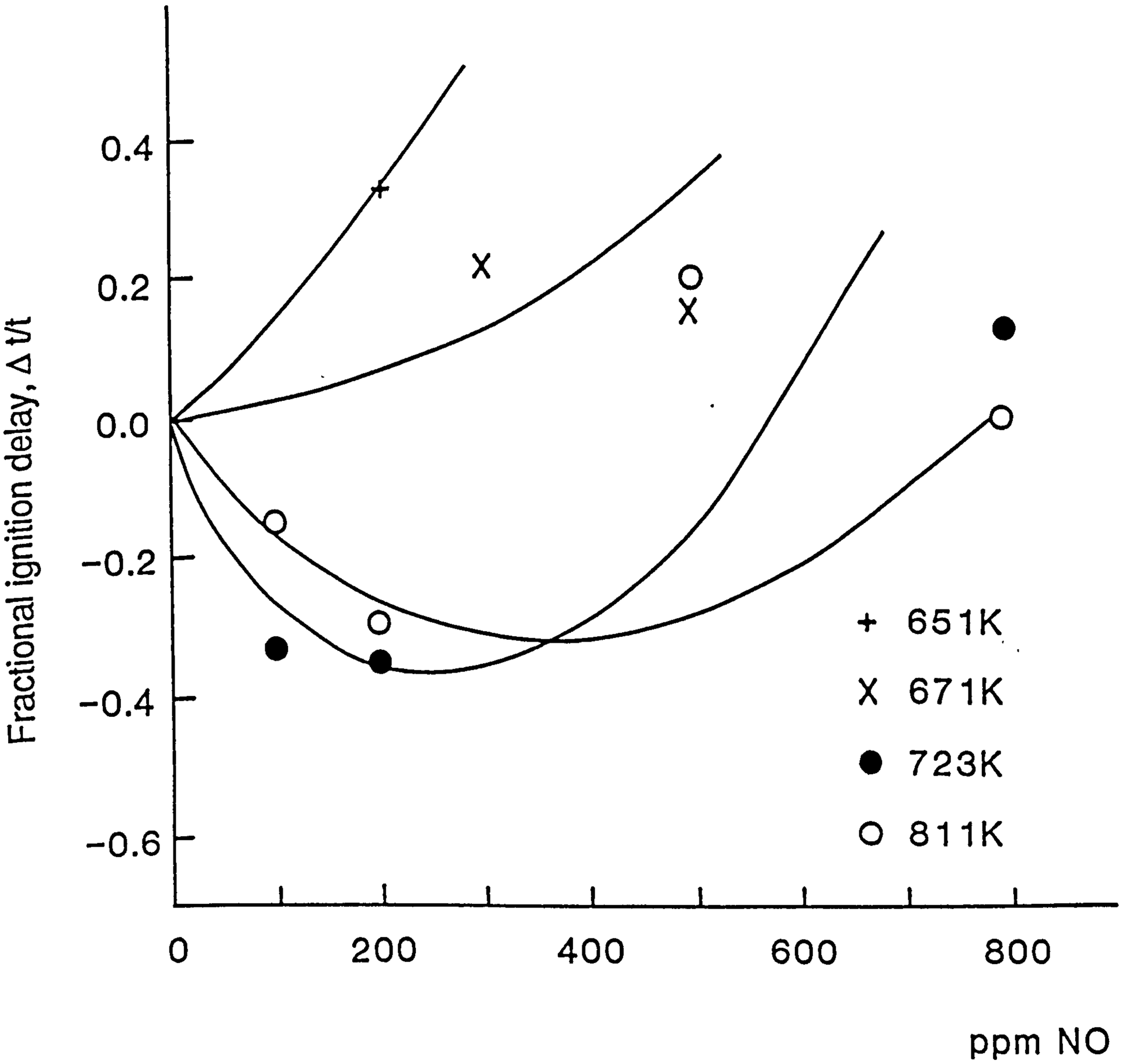

Figure (4.5) quantitatively compares the autoignition effects of various nitrogen dioxide or nitric oxide inclusions in 1.64% R.O.N 90, 20% oxygen, nitrogen oxide, 1b diluent balance mixtures, at both ca. 670 and ca. 810K. The figure shows that the lower nitrogen oxide containing mixtures always autoignite with longer ignition delays than their comparable higher oxide counterparts, regardless of the comparative lengthening or shortening ignition delay effects of these nitrogen oxide inclusions.

Finally, the autoignitions of the R.O.N. 90 and nitric oxide containing mixtures always occurred, analogously to the R.O.N. 90 and nitrogen dioxide containing mixtures, without an intermediate cool flame.

(4.4) DISCUSSION

(4.4.1) Chemical kinetic modelling.

The experimental autoignition study of the R.O.N. 90, oxygen, nitrogen dioxide, diluent mixtures was theoretically extended, using the Cox and Cole[34] hydrocarbon autoignition model, to attempt to identify the essential nitrogen dioxide chemistry in this system. The Cox and Cole model was chosen for this purpose owing to its original r.c.m. basis, using the Thornton r.c.m., of the autoignitions of R.O.N. 90, oxygen, diluent mixtures.

The Cox and Cole model was extended by the addition of various nitrogen dioxide reactions, assuming that no modifications were required to this model per se. The modified model was

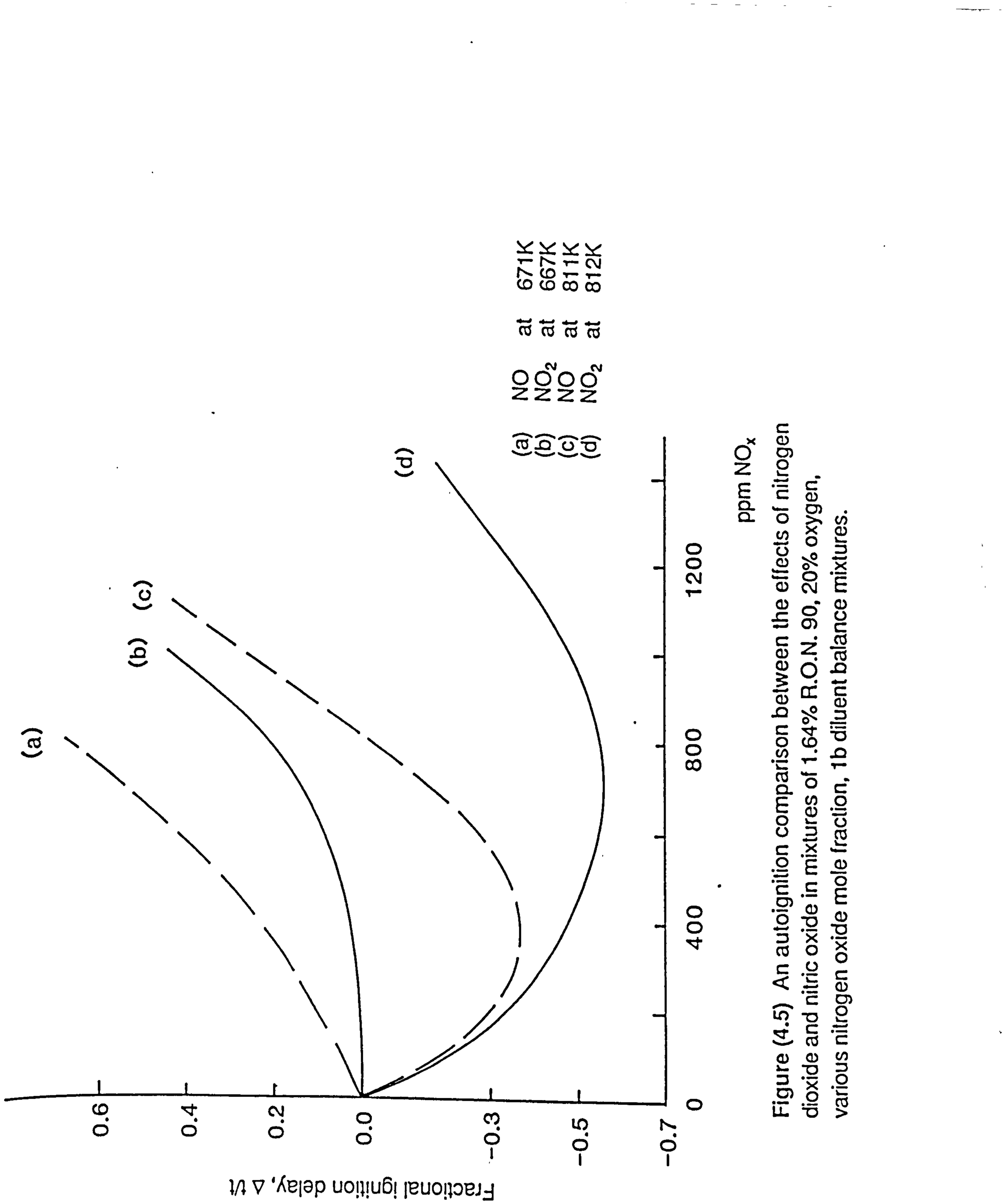

Figure (4.5) An autoignition comparison between the effects of nitrogen dioxide and nitric oxide in mixtures of 1.64% R.O.N. 90, 20% oxygen, various nitrogen oxide mole fraction, 1b diluent balance mixtures.

numerically integrated, according to various initial conditions of concentration, stoicheiometry and temperature, to give a theoretical ignition delay for comparison with the experimental ignition delay, obtained under identical initial conditions. The numerical integration was performed using a mainframe computer and a predictor-corrector integration program, described by Prothero[88]. The degree of correlation between the experimental and theoretical ignition delays, over a wide range of conditions, served to test the validities of the various nitrogen dioxide chemistries included in the model.

Initially, the Cox and Cole model was modified by the addition of a very simple nitrogen dioxide chemistry, that was qualitatively consistent with the observed phenomena. In this simple case, the nitrogen dioxide affects only the initiation and termination, and not the branching processes in the autoignition mechanism. Accordingly, the Cox and Cole model was extended by adding the H-abstraction reactions of nitrogen dioxide with both the fuel and the intermediate aldehyde product, which increases the initiation, together with the addition reactions of nitrogen dioxide with both the alkyl and alkyl peroxy radical intermediates, to give assumed stable products, which increases the termination in the mechanism. The qualitative accounts

$$RH + NO_2 \longrightarrow R\cdot + HNO_2$$

$$RCHO + NO_2 \longrightarrow R\cdot + HNO_2$$

$$R\cdot + NO_2 \longrightarrow \text{Products}$$

$$RO_2\cdot + NO_2 \longrightarrow \text{Products}$$

for the ignition delay variations of the R.O.N. 90 and nitrogen dioxide containing mixtures with both temperature and the nitrogen

dioxide mole fraction of inclusion are respectively given by the different temperature dependencies of these initiation and termination reactions and by the logarithmic (for the initiation) and linear (for the termination) effects of these reaction rates on the ignition delay[89].

In using this modified autoignition model, the kinetic parameters for the nitrogen dioxide reactions were taken as fairly free variables, as these reactions have hardly been isolated for kinetic study. The pre-exponential factors for the abstraction and termination reactions were considered to be in the range 10^8–10^{10} M^{-1} s^{-1}, as suggested by thermochemical kinetics[68]. The activation energies of the termination reactions were assumed to be zero[68] and the activation energies for the abstraction reactions were judged to be within the range 15–25 kcal mol^{-1}, depending on the strength of the carbon–hydrogen bond that is broken, as indicated by the limited and often old data available[90–92].

This modified autoignition model failed, however, despite a thorough variation of the nitrogen dioxide reaction rate parameters within the aforementioned ranges, to reproduce both the observed temperature dependent and the optima ignition delay effects of nitrogen dioxide in the R.O.N. 90 and nitrogen dioxide containing mixtures. This second deficiency appeared to arise from a nitrogen dioxide removal to nitrous acid, an assumed stable product in the model, that denies the reacted nitrogen dioxide the opportunity to recycle by the nitrous acid branching agent decomposing to give nitrogen monoxide, followed by the fast reaction of this oxide with the hydroperoxy radical.

$$HNO_2 + M \longrightarrow \cdot OH + NO + M$$

$$HO_2\cdot + NO \longrightarrow \cdot OH + NO_2$$

This recycling was therefore added to the modified autoignition mechanism, where the nitrous acid decomposition was assumed to occur with hydrogen peroxide decomposition kinetics, and where the reaction between nitrogen monoxide and the hydroperoxy radical was included with well known[93], and therefore invariably treated reaction kinetics.

Remodelling the autoignition study with these additions failed to remedy the aforementioned difficulties and consequently the original model was reverted to, except the Arrhenius parameters of the nitrogen dioxide reactions were allowed to take on values outside their previously prescribed ranges. Under these conditions, the observed autoignition effects of both temperature and nitrogen dioxide mole fraction on the R.O.N. 90 and nitrogen dioxide containing mixtures were qualitatively reproduced in the model. The most satisfactory versions of these models employed rather large pre-exponential factors for the nitrogen dioxide reactions, where it was necessary to assume the instant recycling of nitrogen dioxide. Even these models were, however, quantitatively unsatisfactory in reproducing the above observations, and, typically, over reproduced the autoignition effect of temperature. Accordingly, a typical nitrogen dioxide chemistry, by which the Cox and Cole model was modified, is given below.

				$\log_{10}(A/M^{-1}\ s^{-1})$	E/kcal mol^{-1}
RH + NO_2	⟶	R· + NO_2		10.90	21.5
RCHO + NO_2	⟶	R· + NO_2		10.90	16.0
R· + NO_2	⟶	NO_2		10.76	0
R· + NO_2	⟶	$N0_2$		8.48	0

The over-response of the modelled ignition delay to temperature, despite a thorough kinetic variation of the model, is shown, typically, in figure (4.6), which fully compares the modelled and experimental fractional ignition delays of the R.O.N. 90, oxygen, nitrogen dioxide, diluent mixtures. Consequently it was felt that the initial assumptions of both a nitrogen dioxide chemistry addition to the Cox and Cole model without any changes per se and an independence of the nitrogen dioxide addition to the branching processes of the autoignition mechanism should be questioned.

Consider then the attack of the R.O.N. 90 fuel by nitrogen dioxide. The fuel is predominantly ^{i}octane, which offers fifteen primary hydrogens, two secondary hydrogens and one tertiary hydrogen atom for abstraction. Data for nitrogen dioxide H-abstractions are hardly available, however, it is implied that the H-abstraction reactions of the hydroperoxy radical from ^{i}octane, which is more reactive than nitrogen dioxide in this regard, would produce predominently tertiary alkyl radicals at temperatures less than 920K[94]. In comparison, the H-abstraction reactions of the hydroxy radical from ^{i}octane provide, according to Walker's estimates[95], mainly primary alkyl radicals at 750K. Figure (4.7) shows the predominant oxidation mechanisms of ^{i}octane then, at the representative temperature of 750K, following the H-abstraction from the hydrocarbon by (i) NO_2 (ii) $\cdot OH$, where the favoured peroxy radical isomerizations in these oxidations were calculated from estimates given by Baldwin[39].

Compared to the primary alkyl radical, the tertiary alkyl radical is unable to oxidize to either an aldehyde or a carbonyl hydroperoxide. The tertiary alkyl radical then is unable to produce a branching agent either directly, by oxidation to a hydroperoxide, or

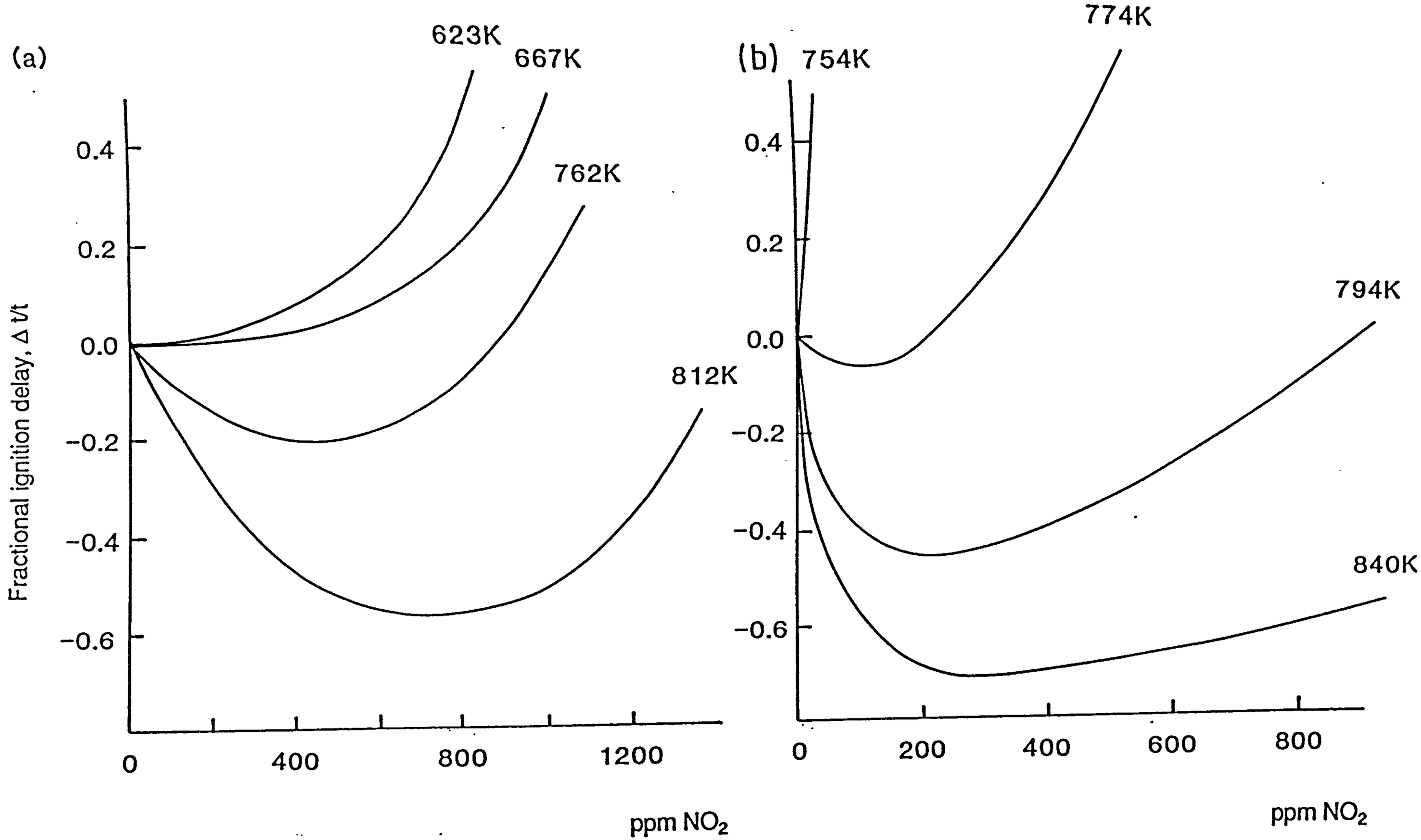

Figure (4.6) An autoignition comparison between (a) the experimental and (b) the theoretical effects of small nitrogen dioxide inclusions in mixtures of 1.64% R.O.N. 90, 20% oxygen, various nitrogen dioxide mole fraction, 1b diluent balance mixtures.

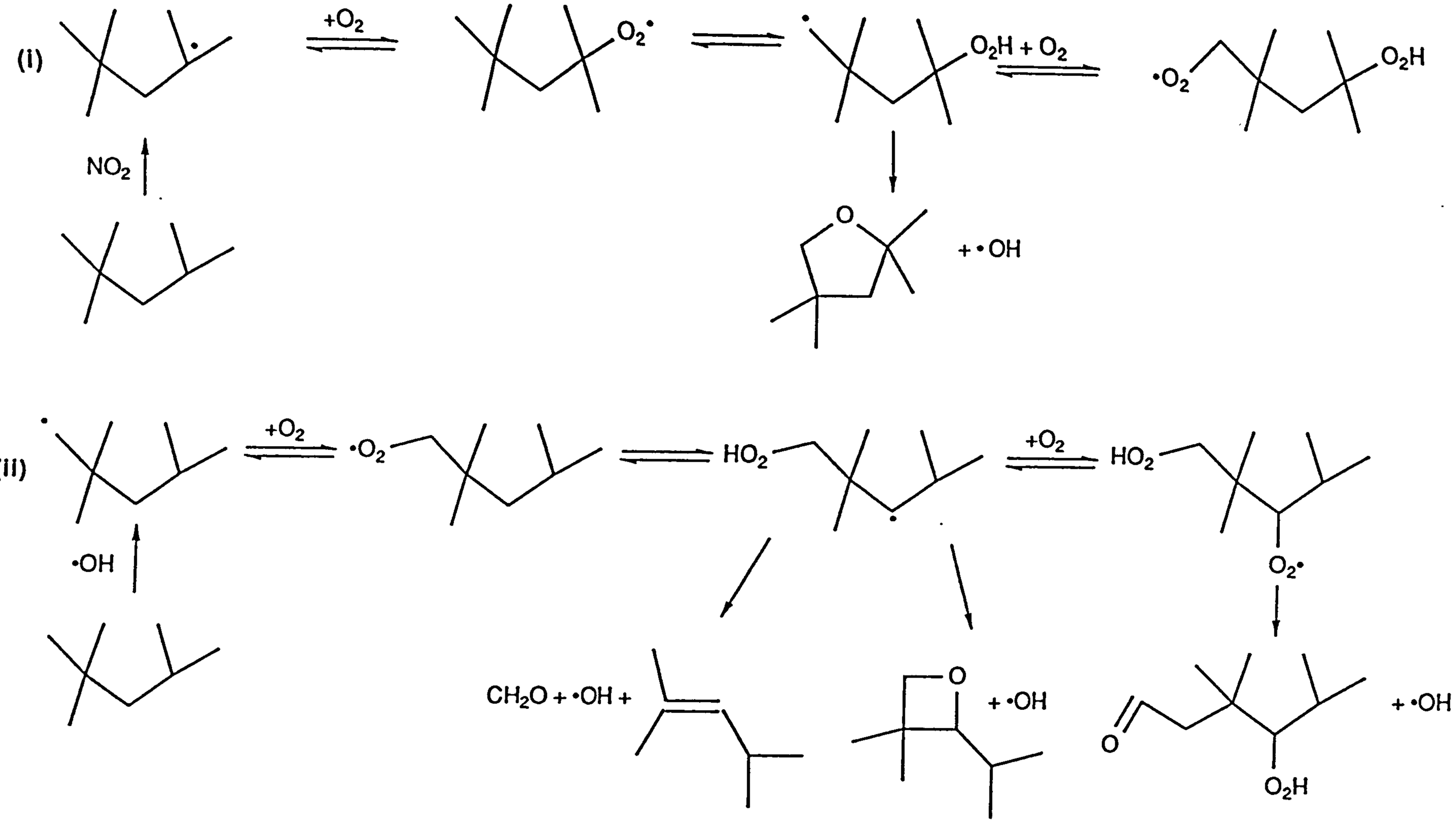

Figure (4.7) The oxidation of ^{i}octane at 750K initiated by (i) NO_2 (ii) •OH

indirectly, by oxidation to an aldehyde. It is therefore possible that, if during the ignition delay, a significant amount of the fuel removal owes to reaction with nitrogen dioxide, then the branching, as well as initiation and termination effects of nitrogen dioxide should be explicitly incorporated into the modified autoignition model. This could account for the difficulties of the modelling exercise and it would be desirable, at a further time, to test this hypothesis by modifying the Cox and Cole model accordingly.

The theoretical difficulties encountered in attempting to understand the effects of nitrogen dioxide on hydrocarbon autoignition permit only qualitative remarks to be made concerning the analogous nitric oxide study. The autoignition effects of nitric oxide were found to be remarkably similar to those of nitrogen dioxide. It is postulated that these similarities owe not to the analogous reactivities of these oxides, and their products, but to an autoignition conversion of the lower to the higher oxide.

Accordingly, nitric oxide is expected to be a poorer initiator than nitrogen dioxide on the basis of the respective 49 and 78 kcal mol^{-1} endothermicities of the H-abstraction reactions of these oxides[68]. Additionally, the termination products of these oxides, nitrosoalkanes for nitric oxide and nitroalkanes for nitrogen dioxide, have markedly different stabilities. Nitrosoalkanes are known to have a similar stability to alkyl nitrates[96], which rapidly decompose in r.c.m. experiments at post-cool flame temperatures, whereas nitroalkanes are known to decompose only slowly under similar conditions[96].

The nitric oxide to nitrogen dioxide conversion is postulated to occur by the reaction of the lower oxide with either an alkyl peroxy

or a hydroperoxy radical.

$$NO + RO_2\cdot \longrightarrow NO_2 + RO\cdot$$

$$NO + HO_2\cdot \longrightarrow NO + \cdot OH$$

Qualitatively, this interpretation accounts, at high temperatures, for the lesser autoignition effect of nitric oxide compared to nitrogen dioxide, assuming an inefficient conversion of the lower to the higher oxide. At low temperatures, however, where nitric oxide is more inhibiting than nitrogen dioxide, this interpretation is deficient and requires further consideration.

(4.4.2) The role of nitrogen dioxide in the behaviour of organic nitrates as ignition improvers.

As mentioned earlier, we are now able to advance our behavioural understanding of organic nitrate ignition improvers from our study of the isolated effects of nitrogen dioxide on hydrocarbon autoignition. This action of organic nitrates stems from their decompositions to provide, in all cases, a bimixture of an alkoxy radical and nitrogen dioxide. By comparing the autoignition effects of nitrogen dioxide, studied here, with those of a variety of organic nitrates, studied by Kirsch and Selby, the relative contribution of the nitrogen dioxide moiety to the total action of these organic nitrates can be assessed.

This comparison is made in figure (4.8), which plots the fractional ignition delay effects of these materials versus their mole fraction ratios compared to the fuel at (a) 650 (b) 760K. The data for the organic nitrates is reproduced from figure (1.2) of Chapter 1 and the autoignition effects of nitrogen dioxide at 650K have been

Figure (4.8) An autoignition comparison between the effects of small inclusions of a variety of organic nitrates and nitrogen dioxide in mixtures of a P.R.F., oxygen and a diluent at (a) 650K (b) 760K.

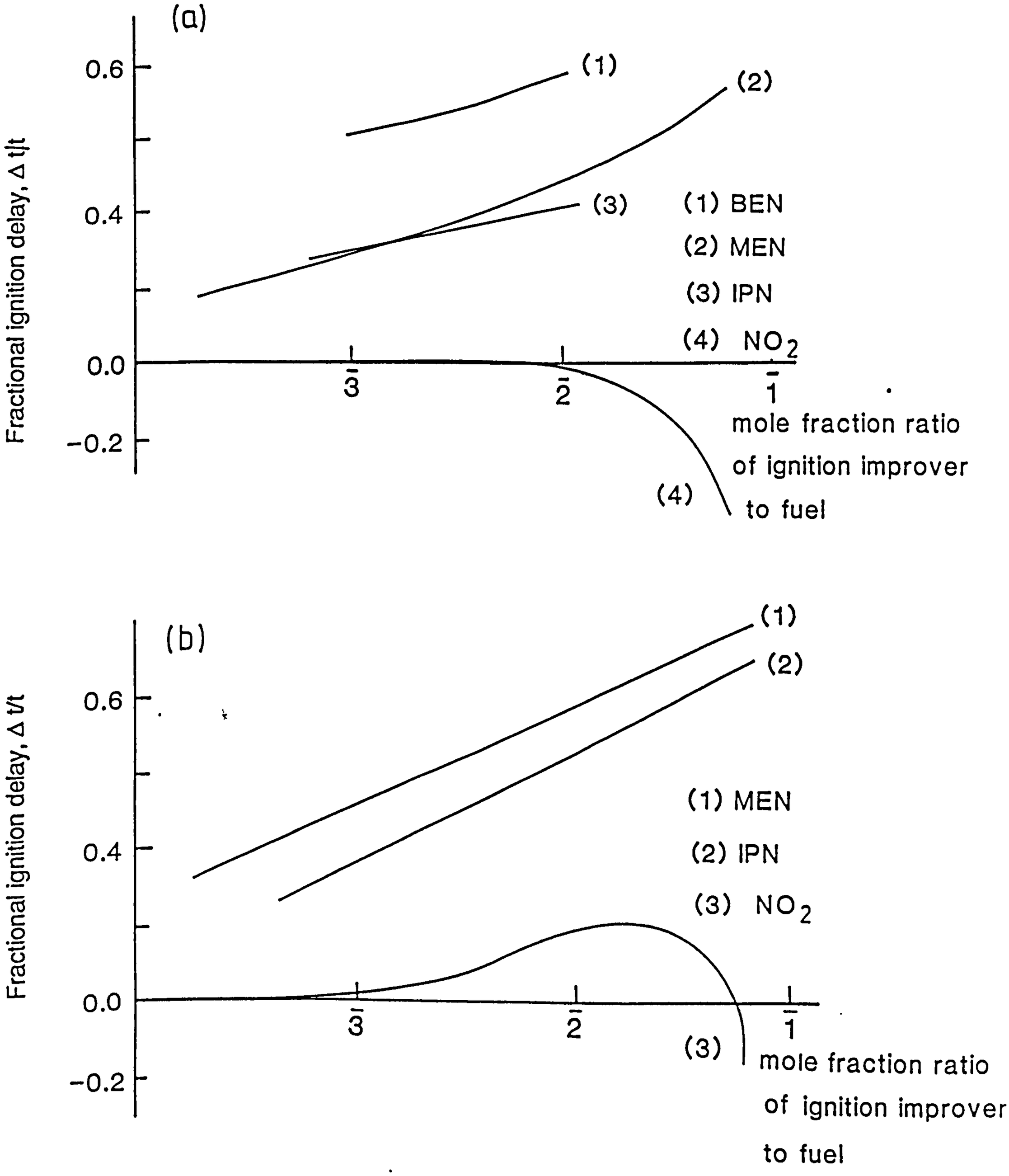

estimated by an interpolation of this study between 623 and 667K. Also note that the fractional ignition delay reduction is a valid comparator between these ignition improvers because it designifies the use of slightly different fuels amongst the three studies.

Figure (4.8) shows that nitrogen dioxide, at 650K, is strongly ignition inhibiting, at all mole fraction ratios compared to the fuel, and the action of organic nitrates as ignition improvers stems solely, therefore, from the initial pyrolyte alkoxy radicals produced from these materials. Additionally, the ignition improver effects of the organic nitrates and nitrogen dioxide vary logarithmically and approximately linearly with their respective mole fractions compared to the fuel and, consequently, the low temperature performance of organic nitrate ignition improvers could be limited, in principle, by the nitrogen dioxide content of these materials. In practice then the use of organic nitrate ignition improvers is desired in small amounts where, taking a fractional ignition delay halving as a desirable nitrate effect, only $\sim 10^{-4}$ mole % of 2-^{n}butoxyethyl nitrate, the most effective nitrate, in the fuel and $\sim 2.5 \times 10^{-2}$ mole % of ^{i}propyl nitrate, the least effective nitrate, in the fuel, would be required to meet this remit. At 760K, nitrogen dioxide acts as a weak ignition improver at small mole fractions, and as a strong ignition inhibitor at large mole fractions. Under the practical conditions just enunciated, the organic nitrates act as ignition improvers, mainly and marginally through the respective alkoxy radical and nitrogen dioxide decomposition fragments of these materials. Accordingly, a fractional ignition delay halving can be effected by the inclusion of either 10^{-3} mole % of 2-methoxyethyl nitrate or 3×10^{-3} mole % of ^{i}propyl nitrate in the fuel, where, respectively, only 5 and 16% of the actions of these materials owe to the pyrolyte nitrogen dioxide.

The organic nitrates have been discussed then as ignition improvers at temperatures that are representative of a cold engine, where their performances are critical, and derives mainly from the initial alkoxy radical decomposition fragments of these materials.

(4.5) CONCLUSIONS

(1) The autoignitions of 1.64% R.O.N. 90, 20% oxygen, nitrogen oxide, 1b diluent balance mixtures, that included either nitrogen dioxide or nitric oxide, have been studied. At temperatures $\lesssim$ 700K, the fractional ignition delays of these mixtures increased in sympathy with the mole fraction of these inclusions. Above this temperature, these mixtures autoignited through optimally shortened fractional delays, that were associated with optima included nitrogen oxide mole fractions. Furthermore, both these fractionally expressed optima shortenings and their associated optima included nitrogen oxide mole fractions increased with temperature.

(2) Below 700K, the autoignitions of the R.O.N. 90 and nitrogen oxide containing mixtures were more inhibited by nitric oxide inclusions than by equivalent nitrogen dioxide inclusions. Above this temperature, nitrogen oxide inclusions sensitized the autoignitions of these mixtures and, additionally, nitrogen dioxide was more effective in this regard than nitric oxide.

(3) The R.O.N. 90, oxygen, nitrogen oxide, diluent mixtures that contained even the smallest nitrogen dioxide or nitric oxide mole fractions, of respectively 100 and 140 ppm, autoignited without the intermediate cool flames observed in the autoignitions of the R.O.N.

90, oxygen, diluent mixtures.

(4) The autoignitions of the R.O.N. 90, oxygen, nitrogen dioxide, diluent mixtures were theoretically investigated in an attempt to identify the essential nitrogen dioxide chemistry in this autoignition system. The Cox and Cole autoignition model was variously modified for this purpose, without any changes per se, by the addition of nitrogen dioxide chemistries that variously failed to provide a satisfactory reproduction of the experimental ignition delay variations with both temperature and the nitrogen dioxide mole fraction of inclusion. The Cox and Cole model was therefore considered to require explicit modification, for this purpose, to discriminate between the particular oxidations of a fuel derived radical that was initiated by either nitrogen dioxide or the hydroxy radical.

(5) Organic nitrates behave as practical ignition improvers, under critical low temperature conditions of $< \sim 750K$, essentially through the initial pyrolyte alkoxy radicals produced in the decompositions of these materials, the copyrolyte nitrogen dioxide is considered to be inert.

CHAPTER 5 A SPECTROKINETIC STUDY OF A HYDROPEROXYALKYL RADICAL

(5.1) INTRODUCTION

Hydroperoxyalkyl radicals are considered to be important generalized hydrocarbon autoignition intermediates, as mentioned in Chapter 1, but, paradoxically, the pre-flame chemistry of this species is poorly understood. This deficiency owes, partly, to the indirect nature of most of the previous hydroperoxyalkyl radical studies[97], where the oxidation products of alkanes of carbon number four or greater were determined, that only gave mechanistic and not kinetic information regarding this radical species. More recently, Baldwin[39] has studied the slow oxidation of neopentane between 653 and 793K and provided the only reliable indirect Arrhenius measurements concerning the decomposition reaction of a hydroperoxyalkyl radical, the hydroperoxyneopentyl radical, which provides 2,2-dimethyl oxetane and the hydroxy radical.

$$\cdot CH_2CMe_2CH_2O_2H \longrightarrow \text{ 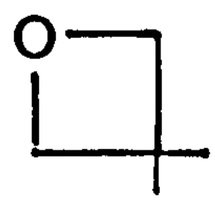 } + \cdot OH$$

Accordingly, the Arrhenius equation found for the hydroperoxy-neopentyl radical decomposition reaction is given below

$$\log_{10}(k/s^{-1}) = 15.04 - 15 \text{ kcal mol}^{-1}/RT \ln 10$$

Another recent study, by Niki[98], involved the photolysis of ethyl nitrite, nitric oxide, methyl hydroperoxide, synthetic air room temperature mixtures, where a Fourier Transform Infra-Red

spectroscopic product analysis revealed the exclusive hydroperoxy–methyl radical reaction by decomposition. The chemistry

$$\cdot CH_2O_2H \longrightarrow CH_2O + \cdot OH$$

of hydroperoxyalkyl radicals is, additionally, malunderstood owing to the limited number of direct attempts to study this species. Accordingly, Ravishankara[99] has performed the pulsed photolysis of methyl hydroperoxide, between 203 and 433K, that indirectly generated the hydroperoxymethyl radical via the hydroxy radical.

$$CH_3O_2H + h\upsilon \longrightarrow CH_3O\cdot + \cdot OH$$

$$CH_3O_2H + \cdot OH \longrightarrow \cdot CH_2O_2H + H_2O$$

$$CH_3O_2H + \cdot OH \longrightarrow CH_3O_2\cdot + H_2O$$

Ravishankara, in parallel, also cophotolysed methyl hydroperoxide with a precursor that provided a cophotolyte and isotopically labelled hydroxy radical that underwent a L.I.F. observed reaction with the hydroperoxide. Typically the cophotolyte was a labelled water such as dideutero water.

$$D_2O + h\upsilon \longrightarrow D\cdot + \cdot OD$$

$$CH_3O_2H + \cdot OD \longrightarrow \cdot CH_2O_2H + DHO$$

$$CH_3O_2H + \cdot OD \longrightarrow CH_3O_2\cdot + DHO$$

These (co)photolysis experiments apparently suggested that the labelled hydroxy radical was more reactive than its unlabelled isotomer and Ravishankara invoked, to account for this apparence, an essentially instantaneous decomposition reaction of the hydroperoxy–methyl radical to give formaldehyde and the hydroxy radical.

$$\cdot CH_2O_2H \longrightarrow CH_2O + \cdot OH$$

In the cophotolysis then the labelled and unlabelled hydroxy radical removals by H–abstraction from both the methyl and hydroxy groups of the hydroperoxide were, respectively, both and only latterly optically visible. The essentially instantaneous hydroperoxymethyl radical decomposition reaction was invoked then on the basis of the dark reaction channel of the unlabelled hydroxy radical with methyl hydroperoxide. The hydroperoxymethyl radical decomposition reaction was subsequently investigated under intended "real time" conditions, where the photolysis of methyl hydroperoxide was performed at 205K and the hydroxy radical removal was followed at very short reaction times, up to only ca. 1 μs. However, even under these conditions, the hydroperoxymethyl radical decomposition reaction remained essentially instantaneous, although a simple computer modelling exercise determined the corresponding upper lifetime limit for this radical to be 20 μs at 205K and in 50 torr of helium.

The previously attempted direct hydroperoxyalkyl radical study, despite its significance, related to the atypical one carbon member of this species as a hydrocarbon autoignition intermediate. This chapter, however, concerns a direct spectroscopic and kinetic study of a more typical intermediate, the α–hydroperoxyisobutyl radical, $\cdot CH_2CMe_2O_2H$. The α–hydroperoxyisobutyl radical was generated by pulse radiolysis from ^{t}butyl hydroperoxide and characterized by ultra–violet (u.v.) absorption spectroscopy. The α–hydroperoxy–isobutyl radical was, subsequently, spectrokinetically studied, between 298 and 398K, where the possible self, decomposition and isomerization reactions of this radical were investigated. The possible α–hydroperoxyisobutyl decomposition and isomerization reactions

respectively give the hydroxy or hydroperoxy radicals and the ^{t}butyl peroxy radical.

$$\cdot CH_2CMe_2O_2H + \cdot CH_2CMe_2O_2H \longrightarrow \text{Products}$$

$$\cdot CH_2CMe_2O_2H \longrightarrow + \cdot OH +$$ 

$$\cdot CH_2CMe_2O_2H \longrightarrow + HO_2\cdot +$$ 

$$\cdot CH_2CMe_2O_2H \longrightarrow {}^tBuO_2\cdot$$

The hydroperoxyisobutyl radical decomposition reaction to give the hydroxy radical has a related interest concerning the Cox and Cole autoignition model[34], where this reaction is generically featured as an important process. Our spectrokinetic study of a hydro-peroxyalkyl radical provides an opportunity then, despite the relatively low temperatures involved, to test the Cox and Cole model on this basis.

(5.2) EXPERIMENTAL

The pulse radiolysis/kinetic absorption technique was fully described in Chapter 2. The radiolysis cell was electrically heated in this study, by a variac supplied cell wound heating tape, up to about 400K. The ^{t}butyl hydroperoxide precursor of the α-hydroperoxy-isobutyl radical was obtained as an aqueous solution and purified before use by vacuum distillation.

(5.2.1) Radical generation.

The pulse radiolysis process is highly energetic and, consequently, the generation of chemical intermediates by this means is often indiscriminate. The direct radiolysis of ^{t}butyl hydroperoxide was considered to be highly undesirable for several according reasons, that include the variety of attendant radiolysis fragments, the occurrence of ionic chemistry and, additionally, the relatively low yield of direct radiolysis fragments. The radiolysis of ^{t}butyl hydroperoxide in a large argon excess, where the radical production owes mainly to the argon sensitized decomposition of ^{t}butyl hydroperoxide, circumvents the last two of these difficulties.

$$Ar + 2MeV\ e^{-} \longrightarrow Ar^{*} + e^{-}$$

$$^{t}BuO_2H + Ar^{*} \longrightarrow Radicals + Ar$$

The argon sensitized ^{t}butyl hydroperoxide decomposition does not, however, circumvent the first of these difficulties and this process may occur with various hydroperoxide constituent bond cleavages, that, on a bond strength basis, are expected to mainly give the ^{t}butoxy and hydroxy radicals.

$$^{t}BuO_2H + Ar^{*} \longrightarrow {}^{t}BuO\cdot + \cdot OH + Ar$$

On this basis, the target α-hydroperoxyisobutyl radical would be a minor product of the argon sensitized ^{t}butyl hydroperoxide decomposition reaction and, consequently, the physical generation of this target radical was eschewed for a cleaner chemical process. Accordingly, the metastable argon atoms were converted to a less reactive intermediate that reacts with the hydroperoxide to give the

α–hydroperoxyisobutyl radical with high selectivity. Both fluorine and chlorine atoms were used for this purpose and were respectively generated in the argon sensitized decompositions of sulphur hexafluoride and methyl chloride. The radiolysis of ^{t}butyl

$$SF_6 + Ar^* \longrightarrow SF_5\cdot + F\cdot + Ar$$

$$CH_3Cl + Ar^* \longrightarrow CH_3\cdot + Cl\cdot + Ar$$

hydroperoxide in both a sulphur hexafluoride and argon or methyl chloride and argon containing system ensured that the observed spectral and kinetic α–hydroperoxyisobutyl radical features were inperculiar to a particular experimental system.

The ^{t}butyl hydroperoxide, sulphur hexafluoride or methyl chloride, argon mixture compositions were chosen to favour the α–hydroperoxyisobutyl radical generations in these systems in two respects. First, the radiolysis mixtures contained a large excess of sulphur hexafluoride or methyl chloride over the hydroperoxide to ensure an insignificant homolytic decomposition compared to chemical reaction of ^{t}butyl hydroperoxide. Second, these mixtures contained a large excess of argon over sulphur hexafluoride or methyl chloride to ensure large halogen atom yields in these radiolysis systems. The radiolysis of ^{t}butyl hydroperoxide, sulphur hexafluoride or methyl chloride, argon mixtures was aimed then to provide the following radical generations from ^{t}butyl hydroperoxide, where the rections that pertain to the methyl chloride containing system are shown in parenthesis

$$Ar + 2Mev\ e^- \longrightarrow Ar^* + e^-$$

$$Ar^* + SF_6 \longrightarrow Ar + SF_5\cdot + F\cdot$$

$$(Ar^* + CH_3Cl \longrightarrow Ar + CH_3\cdot + Cl\cdot)$$

$$^tBuO_2H + F\cdot \longrightarrow \cdot CH_2CMe_2O_2H + HF$$

$$^tBuO_2H + F\cdot \longrightarrow {}^tBuO_2\cdot + HF$$

$$(^tBuO_2H + Cl\cdot \longrightarrow \cdot CH_2CMe_2O_2H + HCl)$$

$$(^tBuO_2H + Cl\cdot \longrightarrow {}^tBuO_2\cdot + HCl)$$

Finally the radiolytic α–hydroperoxyisobutyl radical generations were complicated, even using optimized radiolyte compositions, by the cogenerations of radical side products. Accordingly, in the sulphur hexafluoride containing system both the sulphur pentafluoride and the ^{t}butyl peroxy radicals were cogenerated, although this former cogenerate, with assumed spectral and kinetic similarities between hydroperoxyalkyl and alkyl radicals, was expected to have both spectroscopic resolution[100] and kinetic inertness[101] towards the α–hydroperoxyisobutyl radical. Neither of these innocuities were, however, expected to apply to the cogenerate ^{t}butyl peroxy radical. In the methyl chloride containing system, both the methyl and ^{t}butyl peroxy radicals were cogenerated with the α–hydroperoxyisobutyl radical and the spectroscopic and kinetic implications of both of these radicals on the corresponding α–hydroperoxyisobutyl radical studies required consideration.

(5.2.2) Calibrations.

(i) Halogen atom yields in the radiolysis of both ^{t}butyl hydroperoxide, sulphur hexafluoride or methyl chloride, argon room temperature mixtures.

The fluorine and chlorine atom yields in the radiolysis of both ^{t}butyl hydroperoxide, sulphur hexafluoride or methyl chloride, argon mixtures were respectively determined in the radiolysis of both sulphur hexafluoride and argon or methyl chloride and argon mixtures, that contained the same halogenate amounts and mole fractions as subsequently used in the ^{t}butyl hydroperoxide containing mixtures. The determination of these halogen atom yields was a purely physical measurement, owing to the essentially instantaneous argon sensitized sulphur hexafluoride or methyl chloride decompositions, that are discussed later, and were therefore obtained in halogen atom initial concentration rather than absolute number terms.

The radiolysis of 50 mb sulphur hexafluoride, 1b argon balance mixtures was performed in the presence of a trace of methane, where the fluorine atoms were conveniently converted to the u.v. absorbing methyl radical.

$$CH_4 + F\cdot \longrightarrow CH_3\cdot + HF$$

To extend the essentially instantaneous intermediate formation from the fluorine atoms to the methyl radicals required the presence of a minimum amount of methane. Owing to the retrospectivity of the calibration compared to the α-hydroperoxyisobutyl radical

spectroscopic and kinetic study, the amount of calibrant methane used was equivalent to the ^{t}butyl hydroperoxide amount used in the α–hydroperoxyisobutyl radical study.

The initial fluorine atom concentration was calibrated then from the measured initial methyl radical absorbance. The methyl radical has a prominent and sharp u.v. absorption, associated with a vibronic transition, centred at 216.4 nm[102], where the Beer–Lambert law is obeyed[103]. The initial methyl radical absorbance at 216.4 nm, A_o, with a spectral bandwidth of 0.8 nm, where the vibronic transition R and P+Q rotational branches are unresolved[102], and concentration, $[Me\cdot]_o$, are related then by the following equation, where β is the molar decadic absorbance of this radical and ℓ is the pathlength.

$$A_o = \beta[Me\cdot]_o\ell$$

Absorbance measurements at low wavelength can be complicated by light scattering and this artefactual effect of the optical system, including the radiolyte filled cell, has been assessed. Accordingly, this system transmitance was filtered at the monochromator entrance, by a filter that fully transmits only beyond 260 nm, and was measured at 216.4 nm. Despite an optimization of the optical system, the filtered transmitance, I_s, remained significant compared to the unfiltered transmitance, I_o, and implies an attenuation of the 216.4 nm methyl radical absorbance.

The radiolysis of 1mb methane, 50mb sulphur hexafluoride and 1b argon balance mixtures was optically observed and the true initial methyl radical absorbance, A_t, was determined from the observed corresponding absorbance, A_o, after a correction for the scattered fraction of the analysing light, I_s/I_o, according to the equation given below

$$A_t = \log_{10} \frac{10^{A_o}}{1 + (1-10^{A_o}) \frac{I_s}{I_o}}$$

The calibration method used to determine the true initial methyl radical absorbance was then as follows. (1) The radiolysis cell was filled with the 1mb methane, 50mb sulphur hexafluoride, 1b argon balance room temperature mixture. (2) The mixture absorbance was measured, with minimized light scattering, using the aforementioned filter and an 80 cm pathlength optical system. (3) The 1mb methane, 50mb sulphur hexafluoride, 1b argon mixture was radiolysed, at full dose, and the observed initial methyl radical absorbance was measured at 216.4 nm. This method was repeated, using a fresh calibration mixture, except with a 40 cm pathlength. The measured initial methyl radical absorbances and corresponding scattered light fractions were, respectively, 0.73 and 0.14, with a 80 cm pathlength, and 0.46 and 0.12, with a 40 cm pathlength. Figure (5.1) is a Beer–Lambert plot of these observed absorbances versus pathlength, and also includes the analogous absorbance measured with a 120 cm pathlength. As measured earlier the methyl radical absorbance obeys the Beer–Lambert law, and the curvature shown in these absorbance–pathlength data was a scattered light phenomenon. These observed initial methyl radical absorbances were corrected for the scattered light effect, using the previous equation, and the true initial methyl radical absorbances at 40 and 80 cm pathlengths are also plotted in figure (5.1). The slope of the line through these true absorbances is $\beta[Me\cdot]_o$ and equals 1.42×10^{-2} cm^{-1}. Taking the methyl radical molar decadic absorbance to be 1.06×10^4 M^{-1} cm^{-1}, an average of two recent values by Pilling[58], gives the initial methyl radical concentration to be 1.34×10^{-6} M. The radiolysis of 1mb

Figure (5.1) Initial maximum methyl radical absorbance at 216.4nm against pathlength following the full dose radiolysis of 1mb methane, 50mb sulphur hexafluoride, 1b argon balance room temperature mixtures.

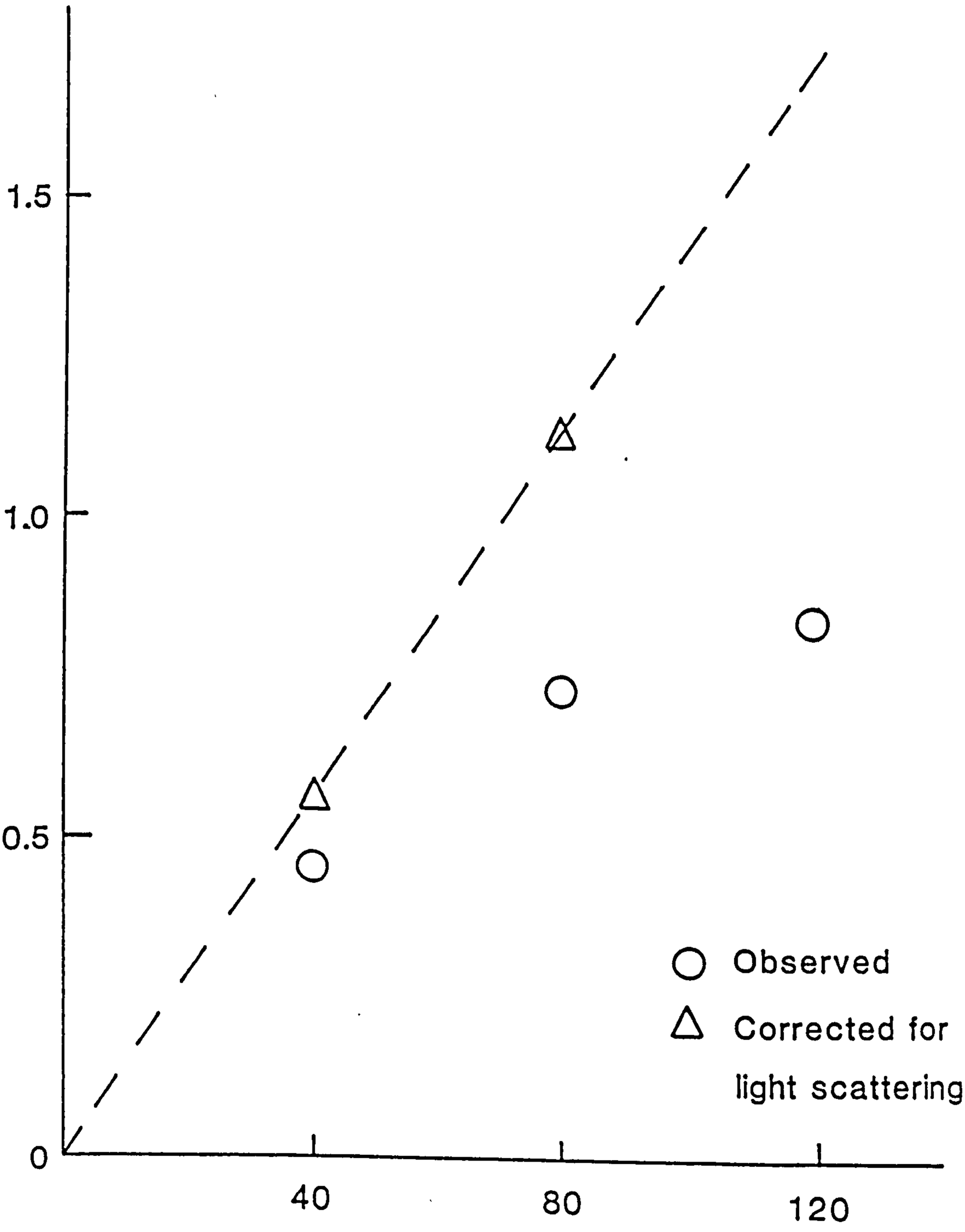

^{t}butyl hydroperoxide, 50mb sulphur hexafluoride, 1b argon balance mixtures provides an initial fluorine atom concentration then of 1.34×10^{-6} M.

The radiolysis of 20mb methyl chloride, 1b argon balance mixtures was calibrated for the initial radiolyte chlorine atom concentration from the initial absorbance of the coradiolyte methyl radical. These absorbance measurements were attemptedly made in the absence of any light scattering by varying the radiolysis dose at a fixed 120 cm pathlength. Figure (5.2) is a plot of this initial methyl radical absorbance at 216.4 nm versus the radiolysis does and shows a curvature that is associated with the scattered light difficulty. The initial methyl radical absorbances associated with the < half dose radiolysis of the methyl chloride, argon mixtures are sufficiently low, however, to be uncompromised by this difficulty and linearly relate to the radiolysis dose according to the line drawn through these data in figure (5.2). The slope of the line in figure (5.2) is the true initial methyl radical absorbance produced in the full dose radiolysis of these calibration mixtures. Again using the methyl radical molar decadic absorbance of 1.06×10^{4} M^{-1} cm^{-1}, together with the 120 cm pathlength, gives the initial methyl radical concentration to be 4.83×10^{-7} M. The radiolysis of 1mb ^{t}butyl hydroperoxide, 20mb methyl chloride, 1b argon balance mixtures provides an initial chlorine atom concentration then of 4.83×10^{-7} M.

(ii) Hydroxy radical absorbance in the radiolysis of both ^{t}butyl hydroperoxide, sulphur hexafluoride or methyl chloride, argon room temperature mixtures.

The hydroxy radical was observed in the radiolysis of both

Figure (5.2) Initial maximum methyl radical absorbance at 216.4nm against the variable dose radiolysis of 20mb methyl chloride, 1b argon balance room temperature mixtures. Pathlength = 120cm.

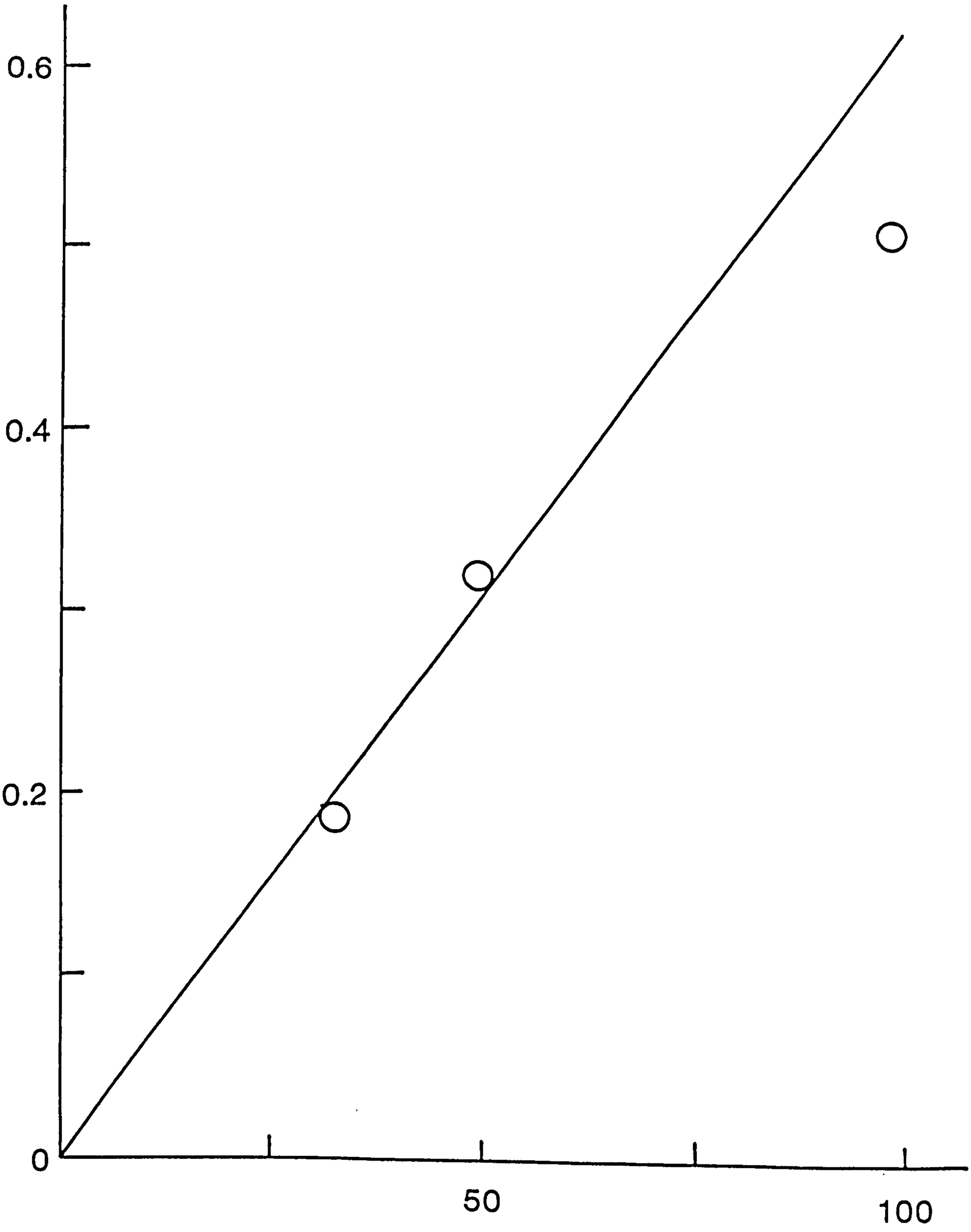

^{t}butyl hydroperoxide, sulphur hexafluoride or methyl chloride, argon mixtures by the u.v. absorption of this species at ca. 309 nm. The u.v. absorption spectrum of the hydroxy radical is shown in figure (5.3), at a recorded scan rate of 1nm min^{-1} and with a spectral band pass of 0.04 nm, and consists of a fully characterized rovibrational structure[104]. The hydroxy radical absorbance was monitored in this study at the "309 feature", a series of unresolved rotational lines, using a spectral band pass of 0.08 nm.

The hydroxy radical absorbance observed in the radiolysis of both ^{t}butyl hydroperoxide, sulphur hexafluoride or methyl chloride, argon mixtures was concentration calibrated in the radiolysis of 1mb water vapour, 50mb sulphur hexafluoride, 1b argon balance mixtures. The radiolysis of this system promptly generates the hydroxy radical, in the fluorine atom reaction with water vapour, at an initial concentration equivalent to the 1.34×10^{-6} M pre-calibrated initial fluorine atom concentration.

$$\cdot F + H_2O \longrightarrow HF + \cdot OH$$

The initial "309 feature" absorbance in the full dose radiolysis of 1mb water vapour, 50mb sulphur hexafluoride, 1b argon balance mixtures is shown versus pathlength in the Beer-Lambert plot of figure (5.4a). These absorbance measurements were made without any light scattering and the curvature shown in figure (5.4a) is ascribed to a non Beer-Lambert law behaviour of the hydroxy radical absorber. Consequently, a modified Beer-Lambert law has been applied to this absorbance, A_o', and is given below, where γ and n are respectively the molar decadic absorbance and non Beer-Lambert law power of this hydroxy radical absorbance.

$$A_o' = \gamma[\cdot OH]_o \ell^n$$

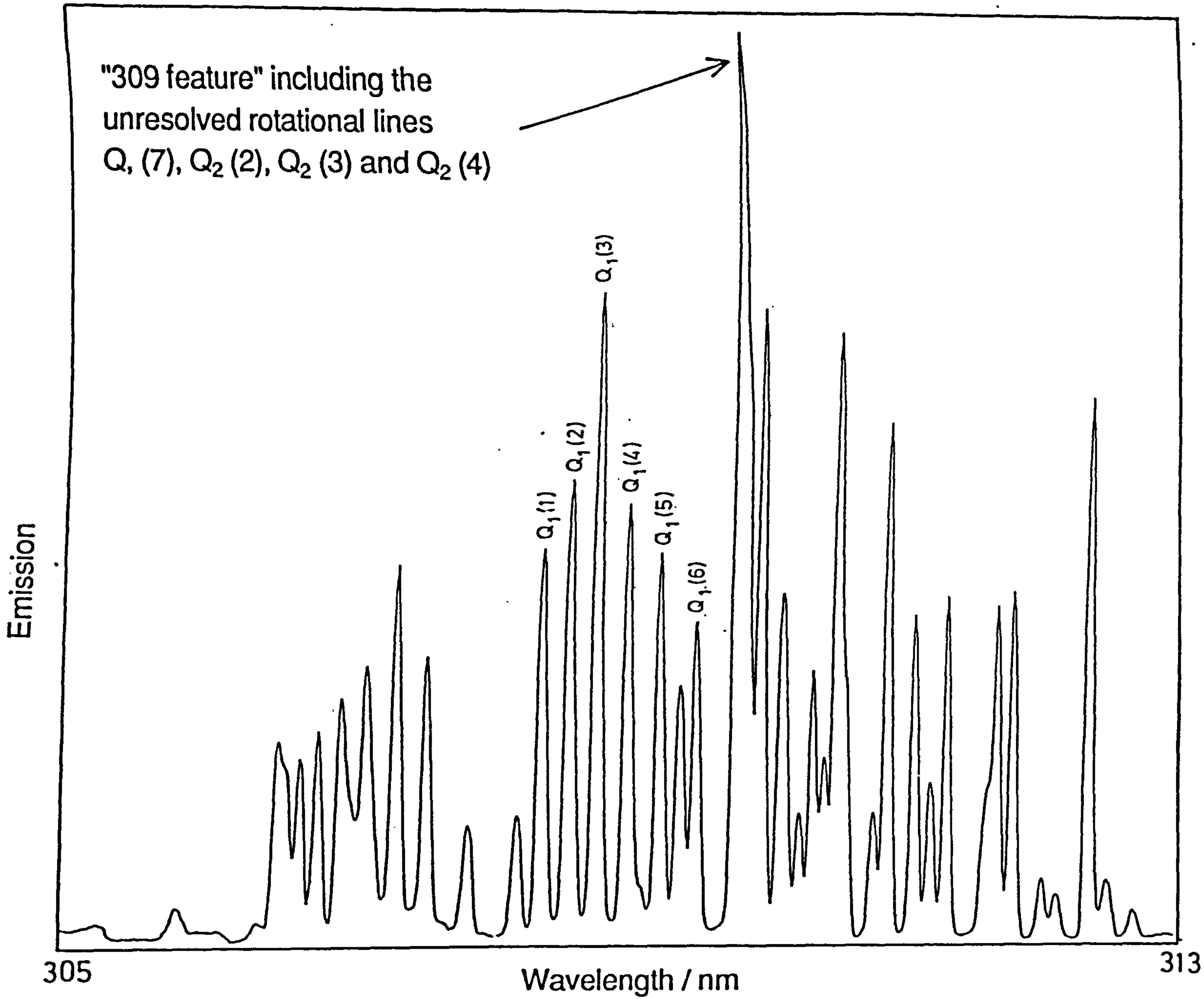

Figure (5.3) Emission spectrum of hydroxy radicals produced by the microwave discharge of argon, water vapour mixtures.

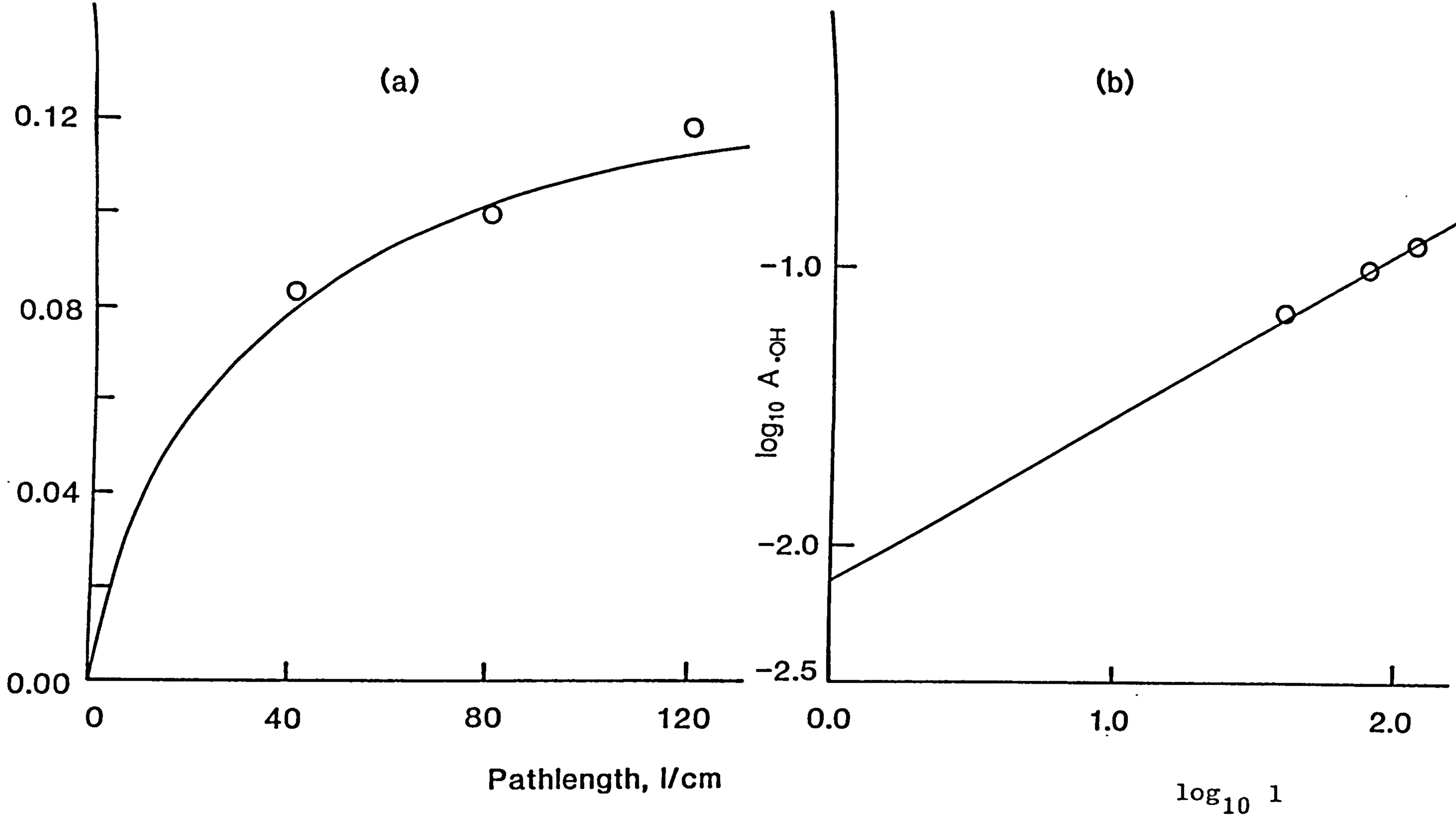

Figure (5.4) Initial maximum hydroxy radical "309 feature" absorbance versus pathlength following the full dose radiolysis of 1mb water, 50mb sulphur hexafluoride, 1b argon balance mixtures as (a) a Beer-Lambert plot (b) a log log Beer-Lambert plot.

Accordingly, figure (5.4b) is a log–log plot of the initial hydroxy radical absorbance versus pathlength and the slope and intercept of this plot are respectively n and $\log_{10}[\cdot OH]_o$ and equal 0.65, formerly, and –2.27, latterly. The initial hydroxy radical concentration of 1.04 x 10^{-6} M gives the molar decadic absorbance of this radical to be 3990 M^{-1} cm^{-1}.

(5.3) RESULTS AND DISCUSSION

(5.3.1) U.V. absorption spectrum of the α–hydroperoxyisobutyl radical.

The radiolysis of both ^{t}butyl hydroperoxide, sulphur hexafluoride or methyl chloride, argon mixtures promptly provides an organic radical pool that includes the α–hydroperoxyisobutyl and ^{t}butyl peroxy radicals. The absorbance of the radiolyte mixture was followed during both the formation and loss of these (hydro)peroxy radicals and is governed by both the spectroscopic and kinetic properties of these radicals. A spectroscopic study of the α–hydroperoxyisobutyl radical was most simply performed then by resolving the spectroscopic and kinetic features of these sytems, by ensuring an excessive formation compared to loss rate of this radical.

The α–hydroperoxyisobutyl radical formation rate was determined, at the used radiolysis mixture compositions, by the rate of the hydroperoxide–halogen atom reaction that was varied according to the hydroperoxide amount in the radiolysis mixture. The radiolyte maximum absorbance was monitored then at 240 nm, where the ^{t}butyl peroxy radical absorbs most strongly[105], according to the amount of hydroperoxide included in the ^{t}butyl hyroperoxide, 50mb sulphur

hexafluoride, 1b argon balance room temperature mixtures. The full radiolysis dose and a 120 cm cell pathlength were used throughout the spectroscopic part of the α–hydroperoxyisobutyl radical study. These absorbance measurements were also made, on account of the broad band nature of the ^{t}butyl peroxy radical absorption spectrum, with the monochromator exit slit set wide to 1 mm, where the spectral band pass was 0.8 nm. Figure (5.5) is a plot of the radiolyte maximum absorbance at 240 nm versus the amount of hydroperoxide in the ^{t}butyl hydroperoxide, 50mb sulphur hexafluoride, 1b argon balance radiolysis mixtures. Figure (5.5) shows that the inclusion of 1mb ^{t}butyl hydroperoxide in the radiolysis mixtures, judged by the plateaued maximum absorbance reached at this hydroperoxide amount, ensured that the (hydro)peroxy radical formations were prompt (complete within ca. 1 μs) and occurred with insignificant colosses.

The spectroscopic part of the α–hydroperoxyisobutyl radical study was continued then using fixed 1mb ^{t}butyl hydroperoxide, 50mb sulphur hexafluoride, 1b argon balance radiolysis mixtures. Figure (5.6) shows the analogous plot to figure (5.5) for the ^{t}butyl hydroperoxide, 20mb methyl chloride, 1b argon balance room temperature radiolysis system and shows, analogously, that the inclusion of 1mb ^{t}butyl hydroperoxide in the halogenate, argon coradiolytes satisfies the desired α–hydroperoxyisobutyl (and, coincidentally, ^{t}butyl peroxy) radical preparation(s) for the desired spectroscopic study. The spectroscopic part of the α–hydroperoxisobutyl radical study was, analogously, continued then using fixed 1mb ^{t}butyl hydroperoxide, 20mb methyl chloride, 1b argon balance radiolysis mixtures.

The radiolysis of 1mb ^{t}butyl hydroperoxide, 50mb sulphur hexafluoride, 1b argon balance room temperature mixtures provides

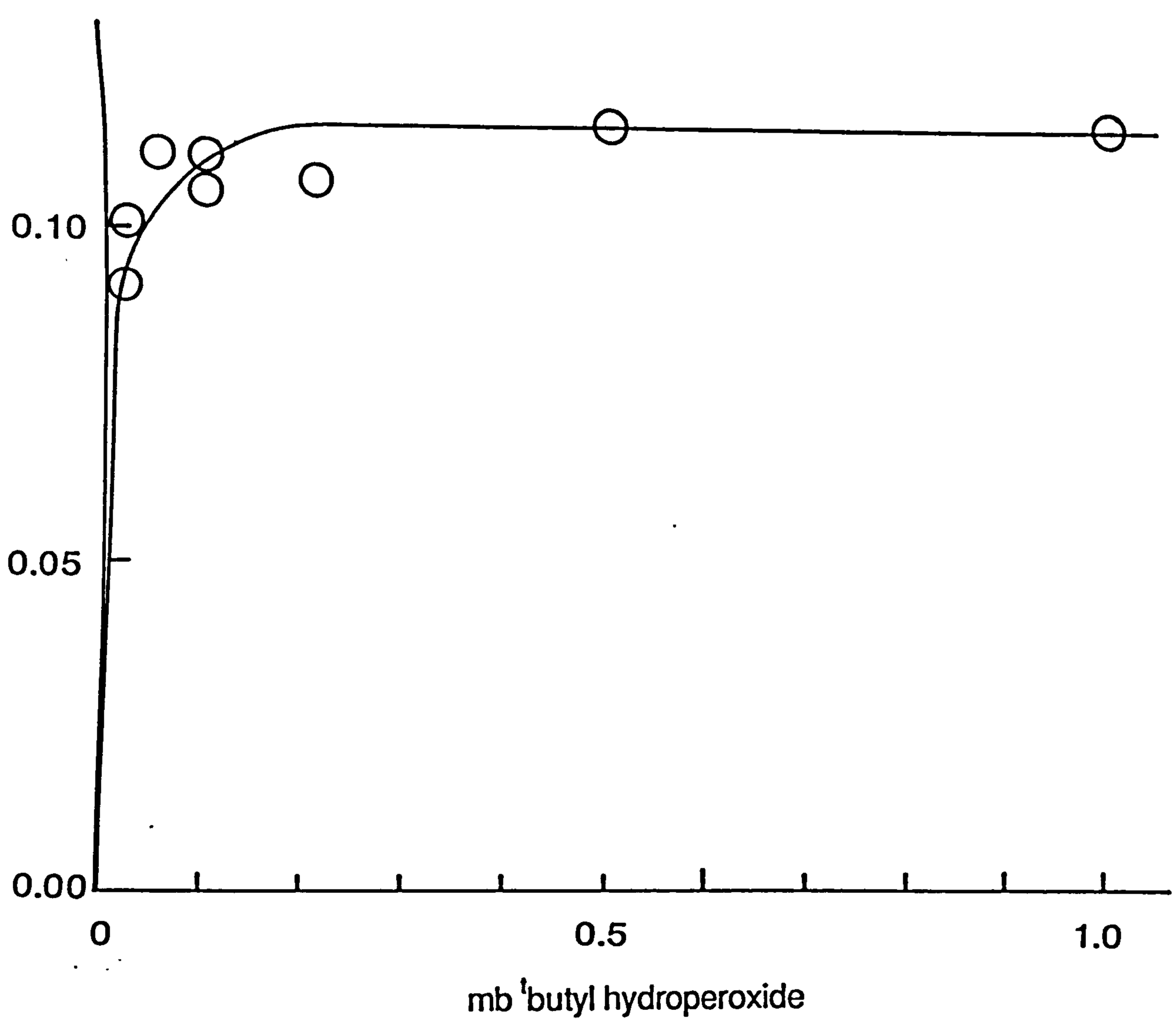

Figure (5.5) Initial maximum absorbance at 240nm following the radiolysis of various tbutyl hydroperoxide absolute pressure, 50mb sulphur hexafluoride, 1b argon balance room temperature mixtures versus tbutyl hydroperoxide absolute pressure. Full dose radiolysis. Pathlength = 120cm.

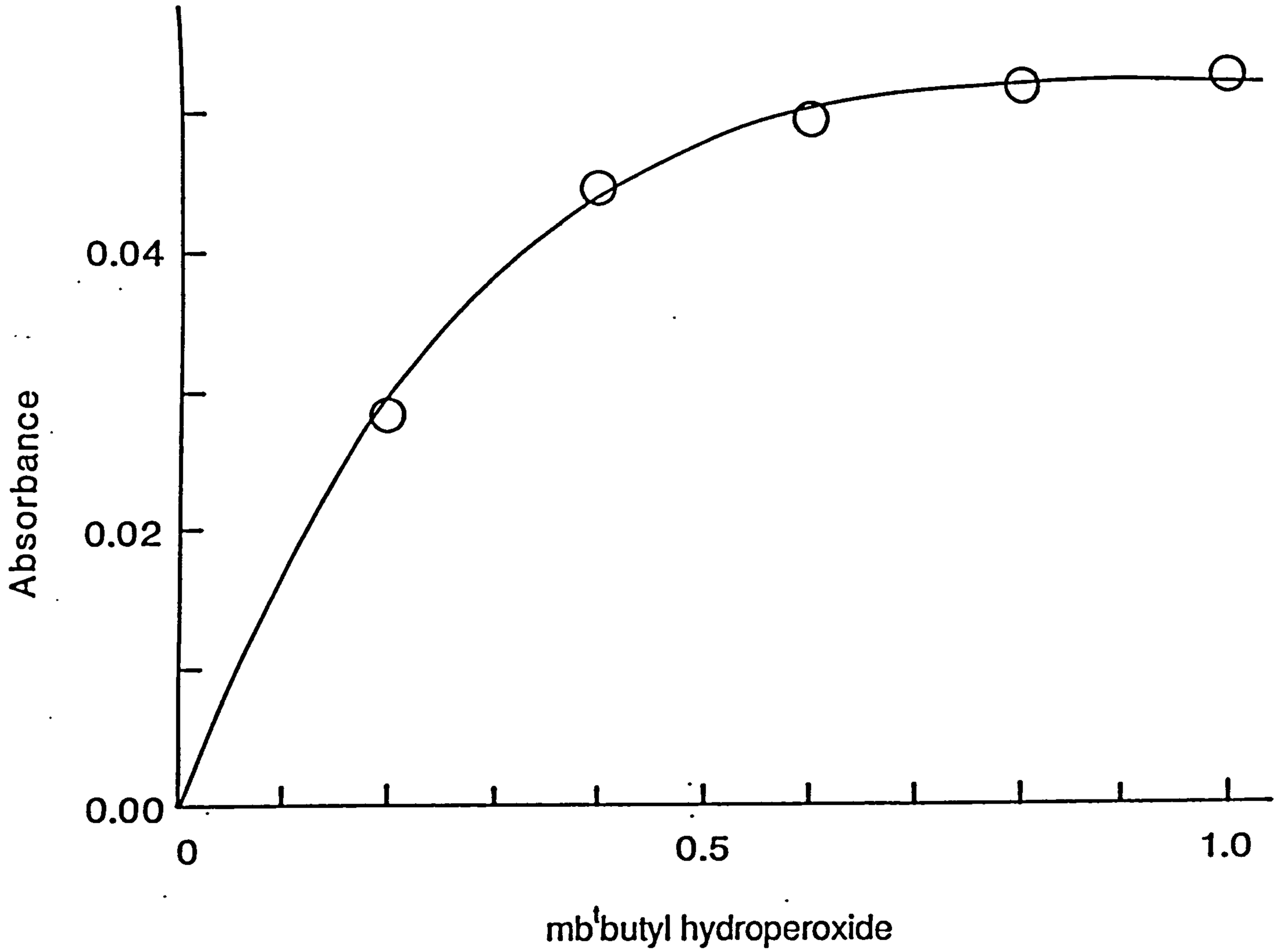

Figure (5.6) Initial maximum absorbance at 240nm following the radiolysis of various ^{t}butyl hydroperoxide absolute pressure, 20mb methyl chloride, 1b argon balance room temperature mixtures versus ^{t}butyl hydroperoxide absolute pressure. Full dose radiolysis. Pathlength = 120cm.

prompt and calibration related amounts of the α–hydroperoxyisobutyl and ^{t}butyl peroxy radicals. The ^{t}butyl hydroperoxide–fluorine atom reaction has not been previously studied, although fluorine atom H–abstraction reactions are known to occur with no activation energy[106]. Accordingly, the ^{t}butyl hydroperoxide–fluorine atom reaction provides the α–hydroperoxyisobutyl and ^{t}butyl peroxy radicals in a statistical 9:1 ratio.

Figure (5.7) shows a typical absorbance–time profile, here at 240 nm, following the radiolysis of a 1mb ^{t}butyl hydroperoxide,50mb sulphur hexafluoride, 1b argon balance room temperature mixture, where the absorbance promptly rises and subsequently decays to a plateau. Figure (5.8) shows both the u.v. absorption spectra, between 210 and 290 nm, of the maximum and long–time absorbances, defined latterly as the plateau absorbance at a
400 μs reaction time, derived from the typified profiles of figure (5.7). The α–hydroperoxyisobutyl radical u.v. absorption spectrum will now be derived from the related maximum absorption spectrum and the nature of the long–time absorbance will subsequently be discussed.

Concerning the α–hydroperoxyisobutyl radical spectrum, the maximum absorbance owed to a α–hydroperoxyisobutyl and ^{t}butyl peroxy radical prompt population that differed absolutely, though not relatively, to that previously indicated. This arose from an inference, to be later discussed, that some of the fluorine atoms are directly converted to the hydroxy radical. Accordingly, the average maximum absorbance of the hydroxy radical "309 feature" was 0.022. The hydroxy radical concentration, that was promptly and directly derived from the fluorine atoms, was on average then, using the hydroxy radical molar decadic absorbance and non Beer–Law power of 3990

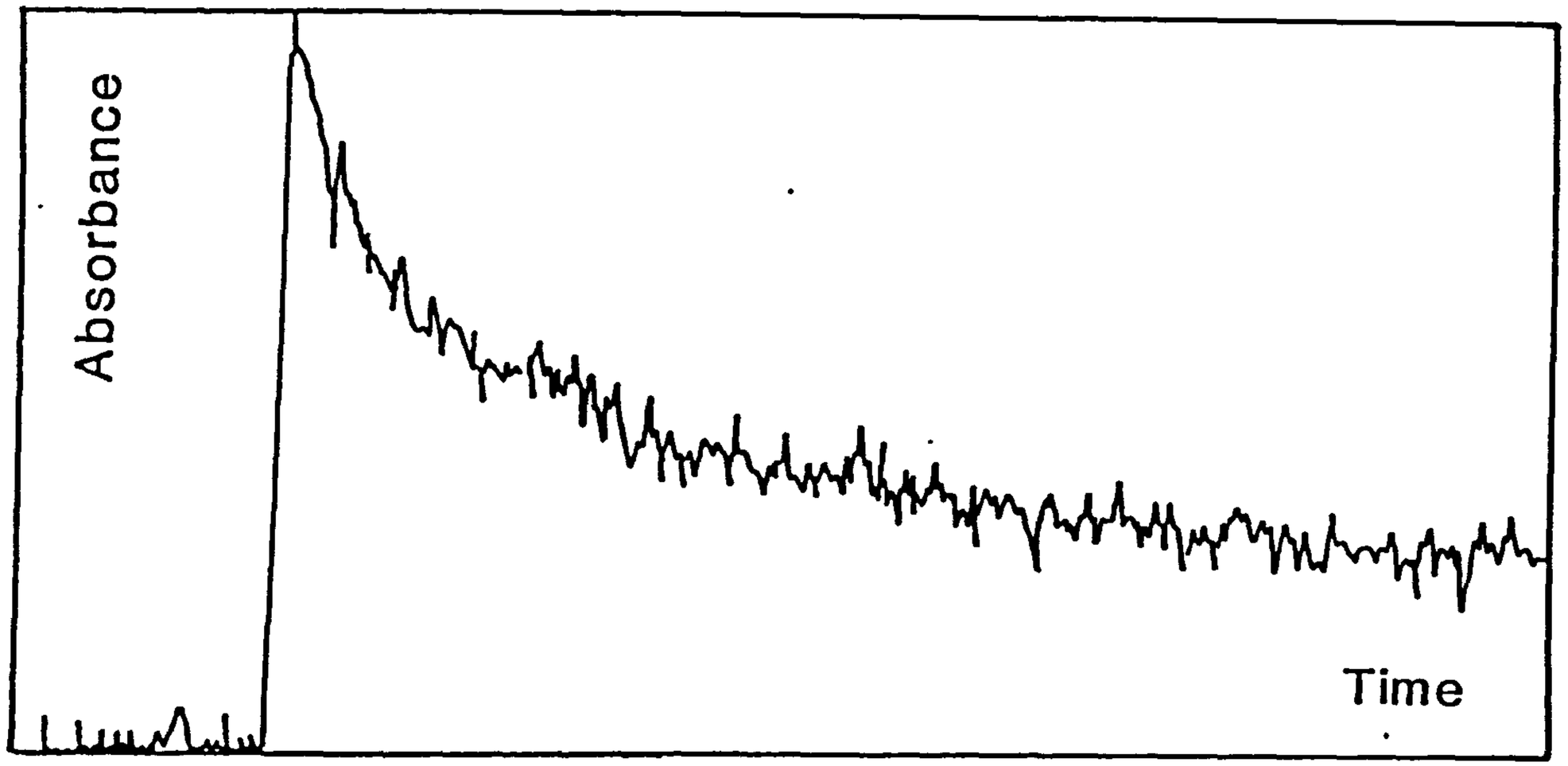

Figure (5.7) Decay trace following the radiolysis of 1mb ^{t}butyl hydroperoxide, 50mb sulphur hexafluoride 1b argon balance mixtures. Temperature = 298K, Wavelength = 240nm, Time span = 400μs.

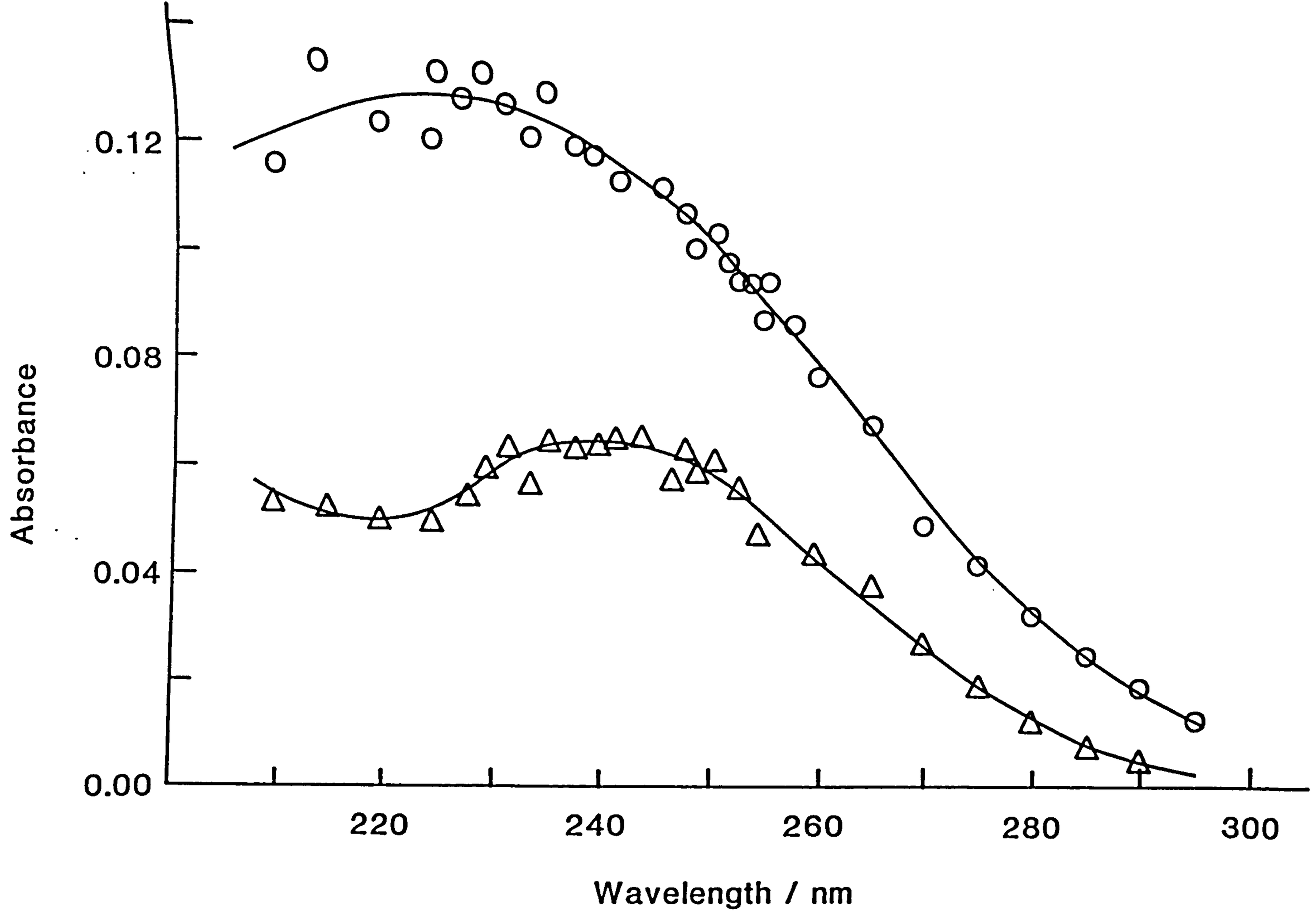

Figure (5.8) U.V. absorption spectra of the initial O and long time Δ absorbances following the radiolysis of 1mb ^{t}butyl hydroperoxide, 50mb sulphur hexafluoride, 1b argon balance room temperature mixtures. Full dose radiolysis. Pathlength = 120cm.

M^{-1} cm^{-1} and 0.65 respectively, 0.25 x 10^{-6} M. Similarly, and consequently, the α-hydroperoxyisobutyl and ^{t}butyl peroxy radical respective concentrations were, with a total unconverted fluorine atom concentration of 1.34 x 10^{-6} M and a statistically based attack of this atom on the hydroperoxide, 0.98 x 10^{-6} and 0.11 x 10^{-6} M. The α-hydroperoxyisobutyl radical u.v. absorption spectrum is given from the related maximum absorption spectrum then by subtraction of the u.v. absorption spectrum of a 0.11 x 10^{-6} ^{t}butyl peroxy radical concentrate[105]. Accordingly, the α-hydroperoxyisobutyl radical u.v. absorption spectrum is shown in figure (5.9), is broad and featureless and peaks at 215 nm, where, using the 0.88 x 10^{-6} M initial α-hydroperoxyisobutyl radical concentration, the molar decadic absorbance is 1011 M^{-1} cm^{-1}.

Finally, the u.v. absorption spectrum of the long-time absorbance concurred with that of the ^{t}butyl peroxy radical and suggested that this radical, at least on a 1 ms timescale, was a stable product.

The radiolysis of 1mb ^{t}butyl hydroperoxide, 20mb methyl chloride, 1b argon balance room temperature mixtures provided similar absorbance-time profiles to those observed in the related sulphur hexafluoride containing system. Similarly, the initial and long-time u.v. absorption spectra observed in this second system are shown, in comparison with the analogous first system spectra, in figure (5.10). Also the α-hydroperoxyisobutyl u.v. absorption spectrum, was derived from the related initial absorption spectrum, noting a prompt and chlorine atom derived hydroxy radical formation. The "309 feature" hydroxy radical absorbance was, correspondingly, and on average, 0.004 and gives the corresponding

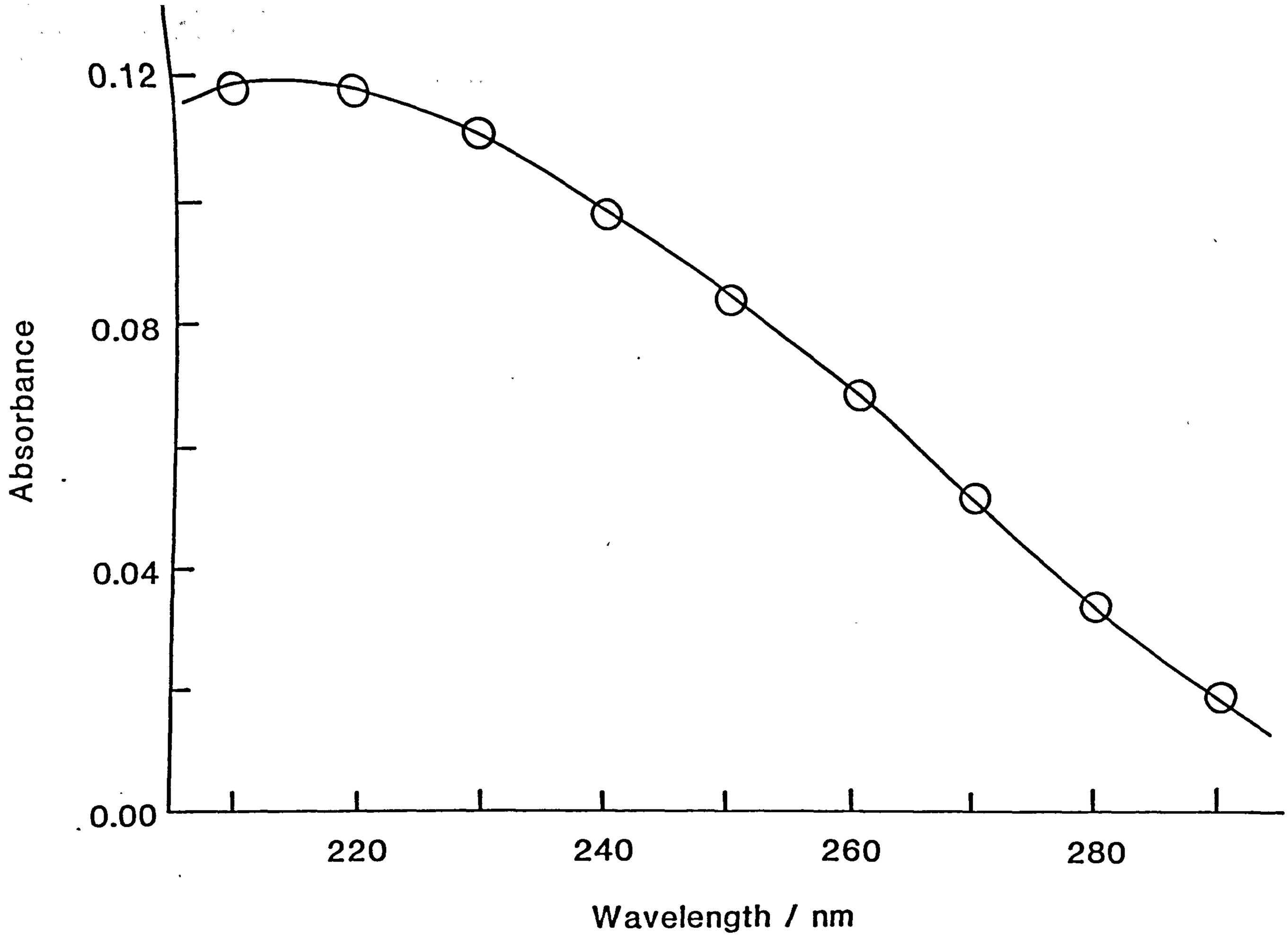

Figure (5.9) U.V. absorption spectrum of the α - hydroperoxyisobutyl radical produced in the radiolysis of 1mb ^{t}butyl hydroperoxide, 50mb sulphur hexafluoride, 1b argon balance room temperature mixtures. Full dose radiolysis Path length = 120cm.

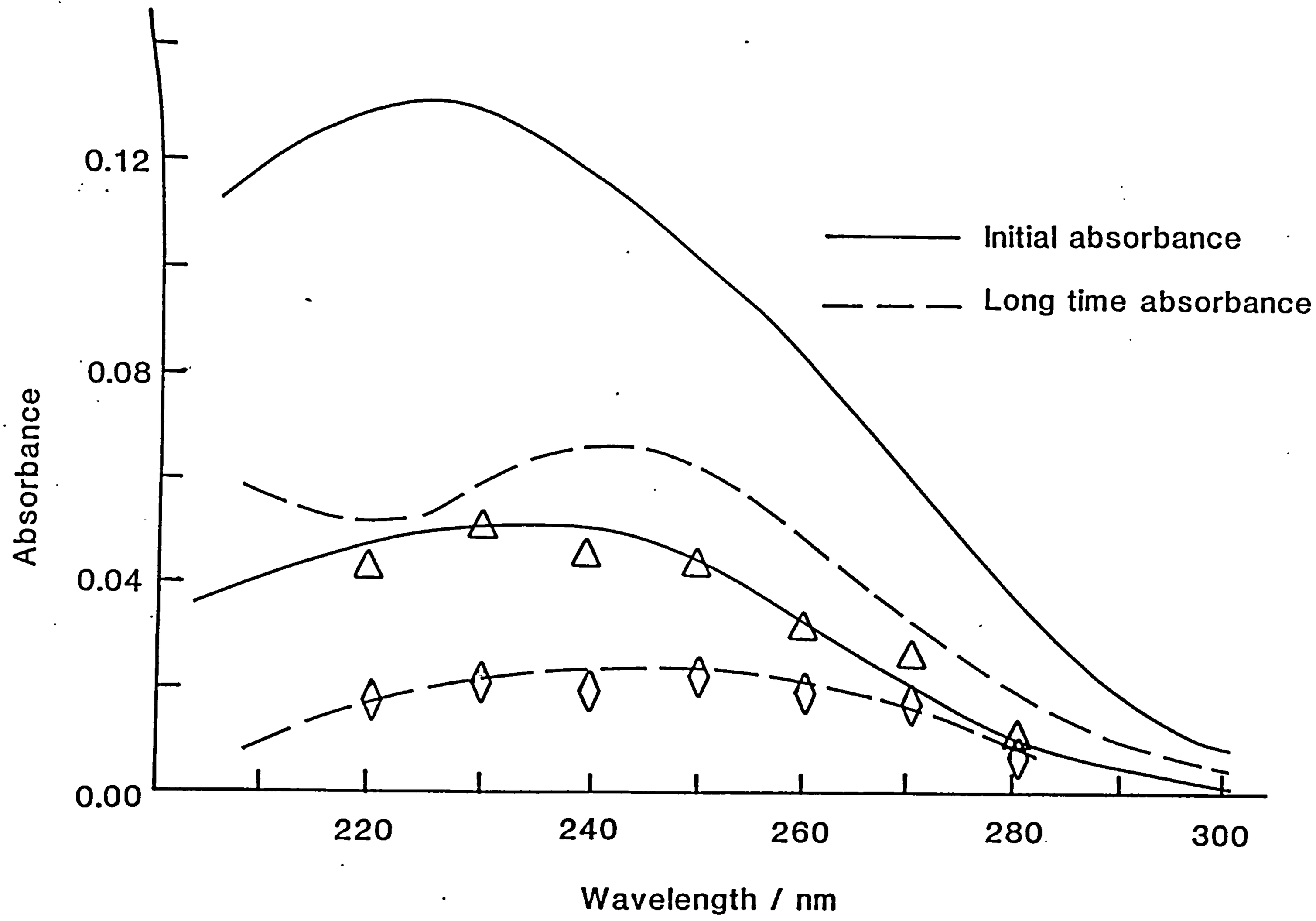

Figure (5.10) U.V. absorption spectra of the initial △ and long time ◇ absorbances following the radiolysis of 1mb ^{t}butyl hydroperoxide, 20mb methyl chloride 1b argon balance room temperature mixtures. The comparable spectra obtained using the sulphur hexafluoride system are also shown. Full dose radiolysis. Pathlength = 120cm.

hydroxy radical concentration to be 4.46 x 10^{-8} M. The maximum total α-hydroperoxyisobutyl and ^{t}butyl peroxy radical concentrations was then, from the 4.83 x 10^{-7} M unconverted chlorine atom concentration and the above maximum hydroxy radical concentration, 4.38 x 10^{-7} M. The maximum relative α-hydroperoxyisobutyl and ^{t}butyl peroxy radical concentrations were estimated to equal the analogous 0.19 relative radical concentration produced in the studied isobutane-chlorine atom reaction[107]. The maximum α-hydroperoxy-isobutyl and ^{t}butyl peroxy respective radical concentrations were then 3.68 x 10^{-7} and 6.99 x 10^{-8} M. The α-hydroperoxyisobutyl radical u.v. absorption spectrum was obtained from the related maximum absorption spectrum by subtraction of the u.v. absorption spectrum of a 6.99 x 10^{-8} M ^{t}butyl peroxy radical concentrate. Figure (5.11) shows the resulting α-hydroperoxyisobutyl radical spectrum in comparison with this radical spectrum obtained using the ^{t}butyl hydroperoxide, sulphur hexafluoride, argon radiolysis system. The α-hydroperoxyisobutyl radical u.v. absorption spectrum obtained using the ^{t}butyl hydroperoxide, methyl chloride, argon radiolysis system peaks at ~ 215 nm, where, using the 2.68 x 10^{-7} M maximum concentration of this radical, the molar decadic absorbance is 930 M^{-1} cm^{-1}.

The assigned α-hydroperoxyisobutyl u.v. absorption spectra are supported by the essential qualitative and quantitative independence of these spectra on the studied radiolysis system.

(5.3.2) Spectrokinetic and mechanistic study of the α-hydroperoxyisobutyl radical.

The ^{t}butyl hydroperoxide, sulphur hexafluoride, argon system

was used in a subsequent spectrokinetic and mechanistic α–hydroperoxyisobutyl radical study that, formerly, used the α–hydroperoxyisobutyl radical u.v. absorption spectrum.

Initially, the ^{t}butyl hydroperoxide, sulphur hexafluoride, argon system was radiolysed and the α–hydroperoxyisobutyl and hydroxy radical removal orders were determined in a dose dependent half–life study of these radicals. Accordingly, the initial α–hydroperoxy–isobutyl and hydroxy radical concentrations, $[Rad]_o$, were varied, post sympathetically with the initial fluorine atom concentrations, according to the radiolysis dose and the radical half–life, $t_{\frac{1}{2}}$, response gave the radical removal order, m, according to the equation given below

$$\frac{d\log_{10} t_{\frac{1}{2}}}{d\log_{10} [Rad]_o} = 1 - m$$

The radiolysis dose was varied between the full dose and, by interposing a range of variously perforated plates between the Febetron source and the radiolysis cell, a half and a third of the full dose. The α–hydroperoxyisobutyl and hydroxy radical half–lives were respectively determined from the corresponding absorbance decay times at 240 nm and of the "309 feature". These absorbance decays were, formerly, taken to be solely due to the major α–hydroperoxyisobutyl and not to the minor ^{t}butyl peroxy radical initial concentrations and, latterly, were corrected for the hydroxy radical non Beer–Lambert law absorbance. Latterly, the hydroxy radical half–life was given by the time for a 36% decay of the "309 feature" absorbance. Tables (5.1) and (5.2) respectively give the α–hydroperoxyisobutyl and hydroxy radical dose and temperature varied half–lives. Accordingly, the α–hydroperoxyisobutyl and

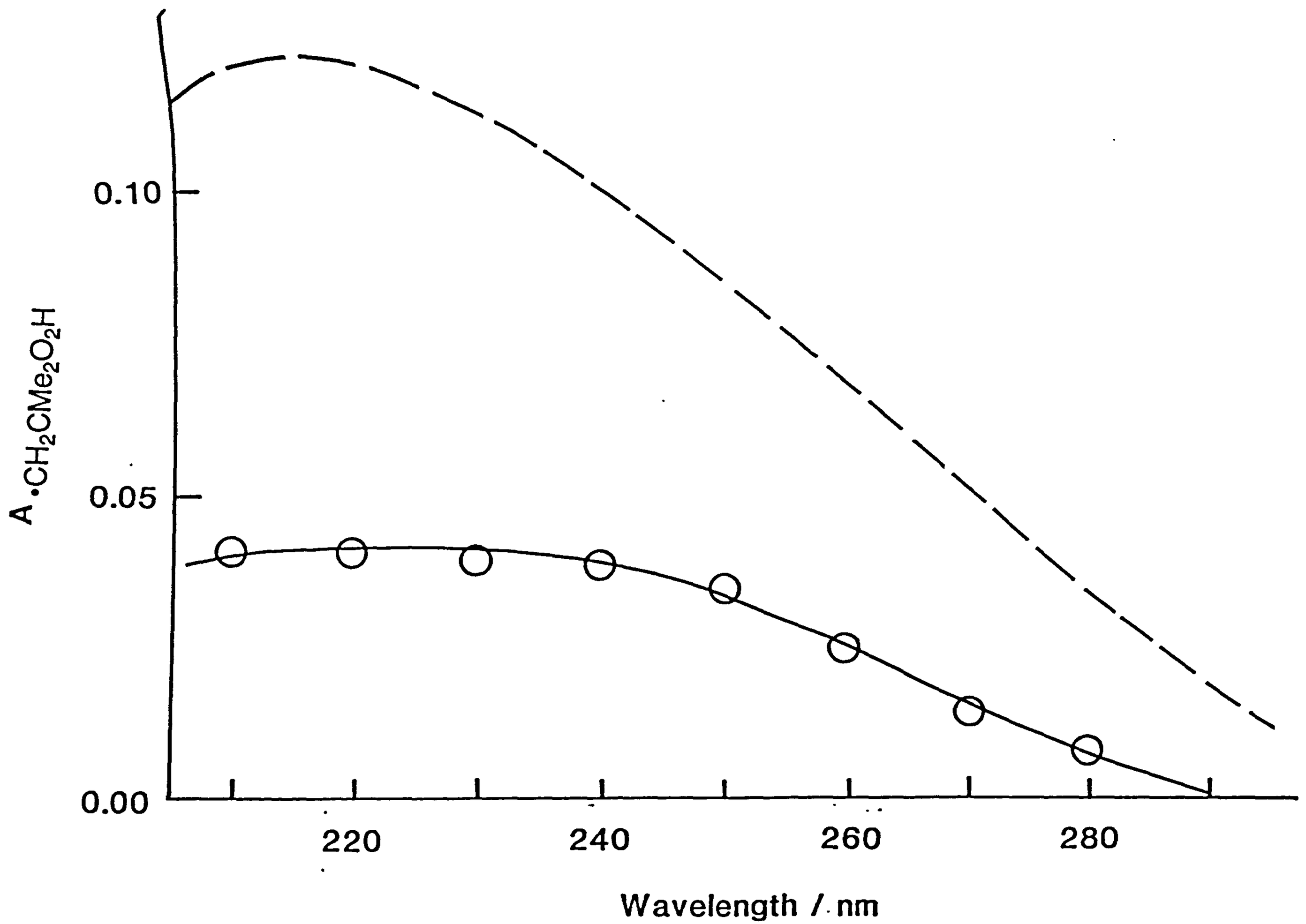

Figure (5.11) U.V. absorption spectrum of the α - hydroperoxyisobutyl radical derived from the radiolysis of 1mb ^{t}butyl hydroperoxide, 20mb methyl chloride 1b argon balance mixtures. The comparable spectrum obtained using the sulphur hexafluoride system is also shown. Full dose radiolysis. Pathlength = 120cm.

hydroxy radical removals are both kinetically dose dependent but temperature independent, although the dose dependency is lower for the hydroxy than the hydroperoxyisobutyl radical. Tables (5.3) and (5.4) respectively give the initial α-hydroperoxyisobutyl and hydroxy radical absorbance measured concentrations at the twelve dose-

Table (5.1) α-Hydroperoxyisobutyl radical half-life/μs versus radiolysis dose and temperature observed following the radiolysis of 1mb ^{t}butyl sulphur hexafluoride, 1b argon balance mixtures.

	Dose(%)		
Temp.(K).	100	50	33
298	25.7	34.3	48.6
333	22.9	32.9	45.7
358	27.1	37.1	50.0
398	28.6	34.3	51.4

Table (5.2) Hydroxy radical half-life/μs versus radiolysis dose andtemperature observed following the radiolysis of 1mb ^{t}butyl hydroperoxide, 50mb sulphur hexafluoride, 1b argon balance mixtures.

	Dose(%)		
Temp.(K).	100	50	33
298	9.8	17.9	16.5
333	12.8	17.6	29.0
358	14.2	20.3	24.4
398	14.2	17.6	14.9

temperature combinations of this study. The half-life and initial radical concentration data of tables (5.1) and (5.3) were used to calculate the α-hydroperoxyisobutyl radical removal order, at each

dose-temperature combination, from the respective log log differentials of these data, that averaged 2.5. An analogous treatment of the data of tables (5.2) and (5.4) gives the average hydroxy radical removal order to equal 1.3.

Table (5.3) Initial α-hydroperoxyisobutyl radical concentrations/ M x 10^6 versus radiolysis dose and temperature produced in the radiolysis of 1mb ^{t}butyl hydroperoxide 50 mb sulphurhexafluoride, 1b argon balance mixtures.

	Dose(%)		
Temp.(K).	100	50	33
298	1.70	1.11	0.75
333	0.81	0.64	0.71
358	1.77	1.18	0.78
398	1.65	1.17	0.69

Table (5.4) Initial hydroxy radical concentrations/M x 10^6 versus radiolysis dose and temperature produced in the radiolysis of 1mb ^{t}butyl hydroperoxide, 50mb sulphur hexafluoride, 1b argon balance mixtures.

	Dose(%)		
Temp.(K).	100	50	33
298	0.35	0.25	0.20
333	0.18	0.12	0.15
358	0.13	0.11	0.06
398	0.62	0.34	0.16

The prompt hydroxy radical origin, that is unexpected, particularly at room temperature, was dismissed as a α-hydroperoxyisobutyl radical decomposition product owing to the disparate removal orders of these two radicals. The prompt hydroxy

radical originates then from either, first, the direct or argon sensitized ^{t}butyl hydroperoxide radiolysis or, second, as a direct product of a fluorine atom reaction. First, the relative amounts of ^{t}butyl hydroperoxide direct radiolysis compared to fluorine atom attack are difficult to estimate. The ^{t}butyl hydroperoxide, sulphur hexafluoride, argon radiolysis mixture is about 1 part to 50 parts to 1000 parts in these respective components. Assuming that 1000 metastable argon atoms are created per directly radiolysed ^{t}butyl hydroperoxide molecule and that only 50/1000 metastable argon atoms collide reactively with sulphur hexafluoride, rather than deactively with the main argon diluent, implies that the ^{t}butyl hydroperoxide undergoes a 2% direct radiolysis compared to fluorine atom reaction. Additionally, the relative amounts of ^{t}butyl hydroperoxide argon sensitized radiolysis compared to fluorine atom reaction are given by the relative ^{t}butyl hydroperoxide and sulphur hexafluoride radiolysis mixture amouts, 1 to 50, and also implies that the ^{t}butyl hydroperoxide undergoes a 2% argon sensitized radiolysis compared to fluorine atom reaction. The total direct and argon sensitized ^{t}butyl hydroperoxide radiolysis maximally provides the prompt hydroxy radical then in a 4% amount compared to the prompt fluorine atom. The prompt hydroxy radical was produced, however, in a 29% amount compared to the fluorine atom and, consequently, the prompt hydroxy radical originates mostly as a direct product of a fluorine atom reaction. The prompt hydroxy radical is postulated then as a product of either a ^{t}butyl hydroperoxide–fluorine atom substitution reaction or a water impurity–fluorine atom reaction.

$$^{t}BuO_2H + F\cdot \longrightarrow {}^{t}BuOF + HF$$

$$H_2O + F\cdot \longrightarrow \cdot OH + HF$$

The spectrokinetic α–hydroperoxyisobutyl radical study was proceeded to determine the rate constants of the α–hydroperoxy–isobutyl radical reactions that are featured in the understood mechanism, given below, of the radiolysed ^{t}butyl hydroperoxide, sulphur hexafluoride, argon system.

1. $\cdot CH_2CMe_2O_2H + \cdot CH_2CMe_2O_2OH \longrightarrow$ Products

2. $\cdot CH_2CMe_2O_2H + {}^{t}BuO_2\cdot \longrightarrow$ Products

3. $^{t}BuO_2H + \cdot OH \longrightarrow \cdot CH_2CMe_2O_2H + H_2O$

4. $^{t}BuO_2H + \cdot OH \longrightarrow {}^{t}BuO_2\cdot + H_2O$

The kinetic absorption spectroscopy of the ^{t}butyl hydroperoxide, sulphur hexafluoride, argon system was examined from the indiscriminate u.v. absorptions of the α–hydroperoxyisobutyl and ^{t}butyl peroxy radicals and the discriminate u.v. absorption of the hydroxy radical. The spectrokinetic features of the radiolysed ^{t}butyl hydroperoxide, sulphur hexafluoride, argon system are characterized then by two absorbance decays and a residual absorbance whereas the radiolyte mechanism is kinetically characterized by four rate constant parameters. A "full" spectrokinetic analysis of the radiolysed ^{t}butyl hydroperoxide, sulphur hexafluoride, argon system requires then a rate constant estimate that pertains to the above mechanism. Correspondingly, the hydroxy radical removal kinetics were determined as a total pseudo first order rate constant for this process that was combined with a fractional estimate of the ^{t}butyl hydroperoxide–hydroxy radical reaction rates, a and b, to respectively give either the α–hydroperoxyisobutyl or ^{t}butyl peroxy radicals. The hydroxy radical total removal rate constant and relative ^{t}butyl hydroperoxide reaction rates essentially provide then the

aforementioned kinetic estimate.

The relative ^{t}butyl hydroperoxide–hydroxy radical reaction rates to give either the α–hydroperoxyisobutyl or ^{t}butyl peroxy radicals were estimated accorded to data respectively provided by Atkinson[108] and Ravishankara[99]. Atkinson has devised a semi–empirical estimation procedure to estimate the reaction rate constants, between 250 and 1000K, of the hydroxy radical with a wide variety of organic substrates. Accordingly, the ^{t}butyl hydroperoxide–hydroxy radical pseudo first order reaction rate constant, to give the α–hydroperoxyisobutyl radical, is given by the expression 2.42×10^4 T^2 exp(–303/T) exp(76/T). The ^{t}butyl hydroperoxide–hydroxy radical reaction kinetics to give the ^{t}butyl peroxy radical were analogously studied by Ravishankara. Accordingly, the methyl hydroperoxide (labelled) hydroxy radical reaction, to give the methyl peroxy radical, was kinetically determined, under pseudo first order conditions, where the rate constant expression was found to be 1.07×10^9 exp(0.053/T). The ^{t}butyl hydroperoxide–hydroxy radical fractional reaction rates to respectively give either (a) the α–hydroperoxyisobutyl radical or (b) the ^{t}butyl peroxy radical are given then, between 298 and 398K, in table (5.5).

Table (5.5) Estimated ^{t}butyl hydroperoxide-hydroxy radical fractional removal rates to give either (a) the α-hydroperoxyisobutyl radical or (b) the ^{t}butyl peroxy radical.

Temp.(K).	a	b
298	0.31	0.69
333	0.40	0.60
358	0.45	0.55
398	0.54	0.46

The spectrokinetic analysis of the ^{t}butyl hydroperoxide, sulphur hexafluoride, argon system was further simplified by assuming that the initial α–hydroperoxyisobutyl radical removal was solely a self removal, where the alternative α–hydroperoxyisobutyl radical and ^{t}butyl peroxy radical cross reaction was considered to be non–competitive. The initial α–hydroperoxyisobutyl radical removal rate is given then in equation (I), where k_1 and k_3' are the respective rate constants for the second order α–hydroperoxyisobutyl radical self reaction and the pseudo first order ^{t}butyl hydroperoxide–hydroxy radical reaction, to give the α–hydroperoxyisobutyl radical, that latterly equals $k_3[RO_2H]$.

$$-\left.\frac{d[\cdot CH_2CMe_2O_2H]}{dt}\right]_o = 2k_1[\cdot CH_2CMe_2O_2H]_o^2 - k_3'[\cdot OH]_o \qquad (I)$$

Equation (I) implies that the initial total α–hydroperoxyisobutyl and ^{t}butyl peroxy radical absorbance is therefore given by the rate expression, (II), where an allowance is made for the ^{t}butyl hydroperoxide–hydroxy radical reaction to give the ^{t}butyl peroxy radical. Accordingly, A_T and $A(\cdot CH_2CMe_2O_2H)$ are the respective total α–hydroperoxyisobutyl and ^{t}butyl peroxy radical and sole ^{t}butyl peroxy radical absorbances, $(k_3 + k_4)'$ equals $(k_3 + k_4)$ $[^{t}BuO_2H]$, ϵ and δ are the respective α–hydroperoxyisobutyl and ^{t}butyl peroxy radical molar decadic absorbances and ℓ is the cell pathlength.

$$-\left.\frac{d\ A_T}{dt}\right]_o = 2k_1\ A(\cdot CH_2CMe_2O_2H)_o^2\delta - (k_{3+4})'a[\cdot OH]_o\epsilon\ell - (k_{3+4})'b[\cdot OH]_o\delta\ell$$

The initial total α–hydroperoxyisobutyl and ^{t}butyl peroxy radical kinetic absorption is equated then with both the second order α–hydroperoxyisobutyl radical removal kinetics and first order

α–hydroperoxyisobutyl and ^{t}butyl peroxy radical formation kinetics. Reciprocally, therefore, the α–hydroperoxyisobutyl radical removal kinetics are given by the total α–hydroperoxyisobutyl and ^{t}butyl peroxy radical kinetic absorptions that are corrected for the first order kinetic formations of these radicals. Accordingly, the hydroxy radical initial concentration and pseudo first order kinetic removal data were respectively determined from the initial and 34% decay times of the hydroxy radical absorbance. The initial hydroxy radical concentrations versus radiolysis does and temperature have already been given in table (5.4) and the corresponding pseudo first order hydroxy radical removal kinetics, expressed under pseudo first order conditions, are given by a reciprocation of the data of table (5.2). Table (5.6) gives then the initial and corresponding corrected

Table (5.6) Initial corrected absorbance-time differentials and corresponding second order α-hydroperoxyisobutyl radical absorbances, both at 240 nm, observed in the variable radiolysis dose and temperature radiolyses of 1mb ^{t}butyl hydroperoxide, 50 mb sulphur hexafluoride, 1b argon balance mixtures.

Temp.(K).	Dose(%)	$-\left[\frac{dA_T}{dt}\right]_o$	+ k_{3+4}' $a[\cdot OH]_o \epsilon \ell$ + k_{3+4}' $b[\cdot OH]_o \delta \ell$	$A(\cdot CH_2CMe_2O_2H)_o^2 \times 10^3$
298	100	2200	+ 781 + 2701 = 5682	28.8
	50	600	+ 305 + 1055 = 1960	12.4
	33	225	+ 264 + 914 = 1403	5.6
333	100	1100	+ 394 + 919 = 2413	6.6
	50	440	+ 192 + 447 = 1079	4.1
	33	315	+ 146 + 339 = 800	5.1
358	100	4957	+ 290 + 550 = 5797	31.3
	50	1518	+ 172 + 326 = 2016	14.0
	33	885	+ 78 + 148 = 1111	6.0
398	100	2041	+ 1660 + 2196 = 5897	27.2
	50	1441	+ 735 + 971 = 3147	13.6
	33	828	+ 409 + 541 = 1778	4.8

absorbance–time differentials and second order α–hydroperoxyisobutyl radical absorbances, both at 240 nm, versus the radiolysis dose and reaction temperature. Figure (5.12) plots the data of table (5.6) and the slope of the figured line is $2k_1/\epsilon\ell$ and equals (1.99 ± 0.10) x 10^5 s^{-1}. Taking the α–hydroperoxyisobutyl radical molar decadic absorbance, ϵ, to be 1011 M^{-1} cm^{-1} gives then k_1, the α–hydroperoxyisobutyl radical self reaction rate constant to equal the temperature independent value, between 298 and 398K, of (1.20 ± 0.06) x 10^{10} M^{-1} s^{-1}.

The spectrokinetic analysis of the ^{t}butyl hydroperoxide, sulphur hexafluoride, argon radiolysis system will now be extended to determine the second order rate constant for the α–hydroperoxyisobutyl radical and ^{t}butyl peroxy radical cross reaction.

The hydro(peroxy) radical cross reaction kinetics were determined in a computer modelling exercise that replicated the entire kinetic absorptions of these radicals, particularly the long time residual absorbance. The kinetic absorption models consisted of the ^{t}butyl hydroperoxide, sulphur hexafluoride, argon system radiolysis mechanism, the existing rate constant and initial concentration data that pertain to this mechanism, various modelled and unknown ^{t}butyl peroxy and α–hydroperoxyisobutyl cross reaction rate constants, and the spectroscopic data used to equate the initial absorbance–time differentials and initial second order α–hydroperoxyisobutyl radical absorbances. The kinetic absorption models were numerically integrated, using a mainframe computer and a predictor–corrector integration program described by Prothero[88], and the modelled and long time absorbances were compared. The kinetic absorption modelling exercise was only applied to the full dose radiolysis of the ^{t}butyl hydroperoxide, sulphur hexafluoride, argon mixtures and table

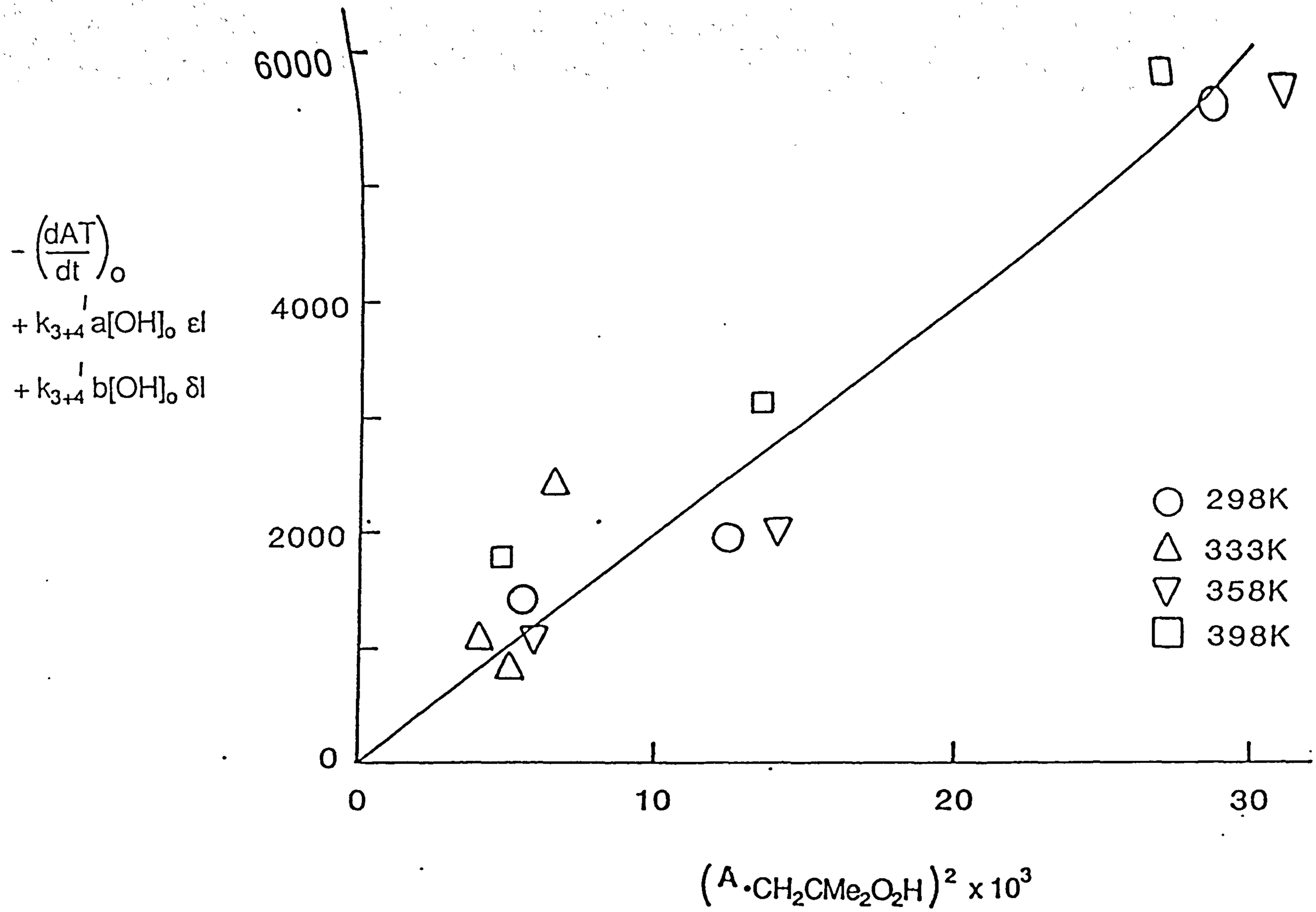

Figure (5.12) Second order plot of the initial α - hydroperoxyisobutyl radical absorbance at 240nm, between 298 and 398K, observed in the variable dose radiolysis of mixtures of 1mb ^{t}butyl hydroperoxide, 50mb sulphur hexafluoride, 1b argon balance mixtures.

(5.7) summarises the model and successfully modelled data of the exercise. The α-hydroperoxyisobutyl radical and ^{t}butyl peroxy radical cross reaction rate constant was given by this exercise to equal the temperature independent value, between 298 and 398K, of $\sim$ 4.0 x 10^{9} M^{-1} s^{-1}. Pilling[109] found the comparable methyl radical and methyl peroxy radical cross reaction rate constant to vary from 5.48 x 10^{10} to 1.93 x 10^{10} M^{-1} s^{-1} between, respectively, 298 and 530K.

Finally, the ^{t}butyl hydroperoxide, methyl chloride, argon system was not spectrokinetically analysed owing to the complexities caused by both the methyl radical product of the argon sensitized methyl chloride radiolysis and the fast methyl chloride-hydroxy radical reaction[110].

(5.4) CONCLUSIONS

This study is the first occasion that both the α-hydro-peroxyisobutyl radical u.v. absorption spectrum or second order self reaction kinetics have been determined.

The radiolysis of ^{t}butyl hydroperoxide, sulphur hexafluoride, argon mixtures has provided the α-hydroperoxyisobutyl radical u.v. absorption spectrum, that occurred between 210 and 290 nm, was broad and featureless, and peaked at 215 nm, where the molar decadic absorbance was 1011 M^{-1} cm^{-1}. The subsequent radiolysis of ^{t}butyl hydroperoxide, methyl chloride, argon mixtures confirmed the aforementioned spectrum.

The α-hydroperoxyisobutyl radical u.v. absorption spectrum has been compared with the analogous alkyl radical spectra that, latterly,

Table (5.7) Summary of computer model initial concentration and rate constant input data and modelled second order α-hydroperoxyisobutyl radical and ^{t}butyl peroxy radical cross reaction rate constants.

Initial concentrations/ M x 10^6			Rate constants						
$\cdot CH_2CMe_2O_2H$	$^tBuO_2\cdot$	$\cdot OH$	$k_1/M^{-1}\,s^{-1}$	$k_{3+4}'a/s^{-1}$	$k_{3+4}'b/s^{-1}$	A(400μs)	k_2(model) $M^{-1}\,s^{-1}$	
Temp.(K)	Dose(%)							
288	100	1.70	0.17	0.35	1.20×10^{10}	1.36×10^4	2.83×10^4	0.037	3.5×10^9
333	50	0.64	0.06	0.12	2.22×10^{10}	1.57×10^4	2.98×10^4	0.037	3.5×10^9
368	100	1.77	0.18	0.13	1.12×10^{10}	1.64×10^4	3.08×10^4	0.074	-
398	100	1.65	0.17	0.62	1.32×10^{10}	1.77×10^4	3.05×10^4	0.052	5.0×10^9

were obtained in both Molecular Modulation Spectroscopy (M.M.S.)[111,112] and Flash Photolysis (F.P.)[113,114] experiments. The M.M.S. and F.P. and experiments generally employed azo compounds as the alkyl radical precursors and the alkyl radical absorption spectra were calibrated from either the precursor removal or the hydrocarbon or nitrogen product formations. Table (5.8) compares the

Table (5.8) Comparison of the α-hydroperoxyisobutyl and various alkyl radical molar decadic absorbances (ε).

Radical.	Technique.	λ/nm.	$\epsilon/M^{-1}\ cm^{-1}$.	T/K.	Determination Method.		Ref.
Me·	MMS	216.4	8050	308	Me_2N_2	loss	115
	FP	216.4	10770	296	C_2H_6	yield	58
	FP	216.4	10480	296	Me_2N_2	loss	58
Et·	MMS	250	494	308	Et_2N_2	loss	115
	FP	250	428	300	N_2	yield	116
^{i}Pr·	MMS	240	1020	308	$^{i}Pr_2N_2$	loss	115
	FP	240	1290	300	N_2	yield	116
^{t}Bu·	MMS	230	1950	308	$^{t}Bu_2N_2$	loss	115
	FP	-	-	-	-	-	-
$\cdot CH_2CMe_2O_2H$	PR	215	1011	298-398	Yield calib.		This work.

α–hydroperoxyisobutyl, methyl[58,115], ethyl[115,116], ^{i}propyl[115,116] and ^{t}butyl[115] radical molar decadic absorbances, at about room temperature, where, in each case, the alkyl radical spectra were characterized in both a M.M.S. and a F.P. experiment. A comparison of the α–hydroperoxyisobutyl and alkyl radical molar decadic absorbances shows, by the disparate α–hydroperoxyisobutyl and ethyl radical molar decadic absorbances, that the α–hydroperoxyisobutyl radical u.v. absorption spectrum is incomparable with the analogous alkyl radical spectra on a simple structural radical centre basis. A more detailed α–hydroperoxyisobutyl and alkyl radical u.v. spectroscopic comparison was not attempted.

The radiolysis of ^{t}butyl hydroperoxide, sulphur hexafluoride, argon mixtures allowed a subsequent spectrokinetic α–hydroperoxyisobutyl radical study between 298 and 398K. The second order α–hydroperoxyisobutyl radical self reaction was kinetically determined, in the variable dose radiolysis of the ^{t}butyl hydroperoxide, sulphur hexafluoride, argon system, and the temperature independent rate constant for this process was found to be $(1.20 \pm 0.06) \times 10^{10}$ s^{-1}.

The second order α–hydroperoxyisobutyl and various alkyl radical self reaction rate constants, where the alkyl radical kinetic and pre–tabulated spectroscopic data were taken from identical sources, that were all determined by kinetic absorption spectroscopy, are compared in table (5.9). Accordingly, the second order

Table (5.9) Comparison of the second order α-hydroperoxyisobutyl and various alkyl radical self reaction rate constants

Radical.	Technique.	k/M^{-1} s^{-1}.	Ref.
Me·	MMS	2.08×10^{10}	115
	FP	3.90×10^{10}	58
Et·	MMS	8.92×10^{9}	115
	FP	1.24×10^{10}	117
^{i}Pr·	MMS	4.18×10^{9}	115
	FP	7.70×10^{9}	117
^{t}Bu·	MMS	1.50×10^{9}	1145
	FP	-	-
$\cdot CH_2CMe_2O_2H$	PR	1.20×10^{10}	This work.

α–hydroperoxyisobutyl and ethyl radical self reaction rate constants most closely compare and suggest that this quantity, unlike the molar decadic absorbance, can be simply related to the structural nature, both primary for these comparable radicals, of the radical centre.

The radiolysis of ^{t}butyl hydroperoxide, sulphur hexafluoride, argon mixtures evidenced a spectrokinetic α-hydroperoxyisobutyl radical removal that was purely second order and no competing first order removal was observed. An upper rate constant estimate of a non-competitive first compared to second order α-hydroperoxyisobutyl radical removal has been made. Accordingly, the maximum possible α-hydroperoxyisobutyl radical first order rate constant was taken to equal $2\sigma[\cdot CH_2CMe_2O_2H]_o$, where σ is the standard error of the second order α-hydroperoxyisobutyl radical removal. The lowest estimate of the first order α-hydroperoxyisobutyl radical removal rate constant is given from the lowest initial α-hydroperoxyisobutyl radical concentration, where the first compared to the second order α-hydroperoxyisobutyl radical removal is kinetically most favoured, produced in the lowest dose ^{t}butyl hydroperoxide, sulphur hexafluoride, argon mixture radiolysis. Accordingly, the lowest initial α-hydroperoxyisobutyl radical concentration was 0.69×10^{-6} M at 398K and implies that the maximum possible first order α-hydroperoxyisobutyl radical removal rate constant is 830 s^{-1} at this temperature. Morley[118] has estimated the first order rate constants for the α-hydroperoxyisobutyl radical removals to give either the hydroxy or hydroperoxy or the ^{t}butyl peroxy radical to respectively equal, in good agreement with this study, 879, 15.7 and 0.44 s^{-1} at 398K.

Finally, the Cox and Cole autoignition model employs a generic hydroperoxyalkyl radical decomposition reaction to give the hydroxy radical as an important process. The Cox and Cole extrapolated rate constant for the generic hydroperoxyalkyl radical decomposition reaction is 237 s^{-1} at 398K and is supported by the upper rate constant estimate, made here, for the α-hydroperoxyisobutyl decomposition reaction.

CHAPTER 6 CONCLUSIONS

The concluding chapter of this thesis is intended to provide both a statement concerning the behavioural ignition improver understanding in hydrocarbon, improver autoignition systems, achieved by this work, and consequently, a direction along which further work could be aimed. The statement concerning the behaviour of ignition improvers in these systems will complementarily draw together, rather than simply reiterate, the various findings of this work, and, as such, is more than simple summary.

First then, the low temperature pyrolyses of an ignition improver variety showed that the correspondingly improved hydrocarbon autoignitions are independent of the exact ignition improver pyrolysis kinetics but vary, in autoignition ease, with the chemistries of these pyrolyte radicals. The low temperature ignition improver pyrolyses isolated the chemistries of the initial pyrolyte alkoxy radicals produced in these processes and found that the 2-^{n}butoxyethoxy radical reactivity was uniquely superior to those of all of the other studied alkoxy radicals. A complementary study of the effects of nitrogen dioxide on hydrocarbon autoignition showed this material to insignificantly contribute, under the conditions of interest, to various nitrate improved hydrocarbon autoignitions.

These pyrolysis and autoignition studies can now be considered together to expose a behavioural ignition improver understanding that is based on the empirical activity order of these materials, BEN > MEN > DTBP > IPN, that was found by Kirsch and Selby. Accordingly, the ignition improver pyrolyses showed that these

materials decompose to provide alkoxy radicals that themselves decompose to provide alkyl radicals. The pyrolyses of 2-^{n}butoxyethyl nitrate and 2-methoxyethyl nitrate respectively provide then the 2-^{n}butoxymethyl and 2-methoxymethyl radicals, whereas the pyrolyses of both di-^{t}butyl peroxide and ^{i}propyl nitrate provide the methyl radical. The ignition improver ranking, BEN > MEN > DTBP > IPN is therefore shown to stem from these alkyl radical oxidations, where a unique 2-^{n}butoxymethyl radical oxidation, to provide the hydroxy radical, was evidenced. However, not only the natures, but the numbers of ignition improver double pyrolyte alkyl radicals should also be considered. Accordingly, the peroxide, di-^{t}butyl peroxide, is stoicheiometrically twice as effective as the nitrates in this regard, which implies a superior ignition improver performance of di-^{t}butyl peroxide over ^{i}propyl nitrate. These considerations would suggest then an ignition improver order of effectiveness to be BEN > DTBP > MEN ~ IPN that, compared to the studies of Kirsch and Selby, misplaces 2-methoxyethyl nitrate and di-^{t}butyl peroxide. This discrepancy might originate in the use of 2-methoxyethyl nitrate surrogates, rather than the original material, in our low temperature pyrolysis study, to provide, after a double decomposition of the parent and the daughter alkoxy radical, the ^{n}propyl rather than the 2-methoxymethyl radical. It is suggested then that the misplacement of 2-methoxyethyl nitrate and di-^{t}butyl peroxide owes to an easier hydroxy radical production in the 2-methoxymethyl rather than the ^{n}propyl radical oxidation. In this case, the 2-^{n}butoxymethyl radical oxidation to provide the hydroxy radical is required to be more facile than both of the above oxidations. Despite the speculation involved, all of these statements are based on accepted belief, and, additionally, the importance of

alkyl radical oxidations to provide the hydroxy radical has been noted in the non-improved hydrocarbon autoignition process. Desirably, these ideas should be tested further and it is suggested that the low temperature pyrolysis of 2-^{n}butoxyethyl nitrate, for example, could be repeated with a careful gas chromatographic search, preferably using a capillary system, for the oxygenates that would be coformed with the speculated hydroxy radical. Figure (6.1a) shows a simplified mechanism for the pyrolysis of 2-^{n}butoxyethyl nitrate in oxygen and indicates the oxygenates that might be searched for. This idea could also be extended to the autoignition situation, that includes a fuel, of the rapid compression machine.

Finally, the achieved insight into the behaviour of ignition improvers in hydrocarbon autoignition systems is suggestive of future investigation into this material class and application. The central idea provided by this work is that an efficacious ignition improver action, as exhibited by the ether nitrates, owes to a hydroxy radical release into the autoignition environment. It is therefore postulated that a premier ignition improver class may be found in the hydroxy ether nitrates, that are expected to be stoicheiometrically more hydroxy radical releasing than their ether nitrate analogues. Figure (6.1b) shows a pyrolysis mechanism of β,β-dihydroxy-2-^{n}butoxyethyl nitrate in oxygen and clearly indicates the potential advantage of this material over its analogue.

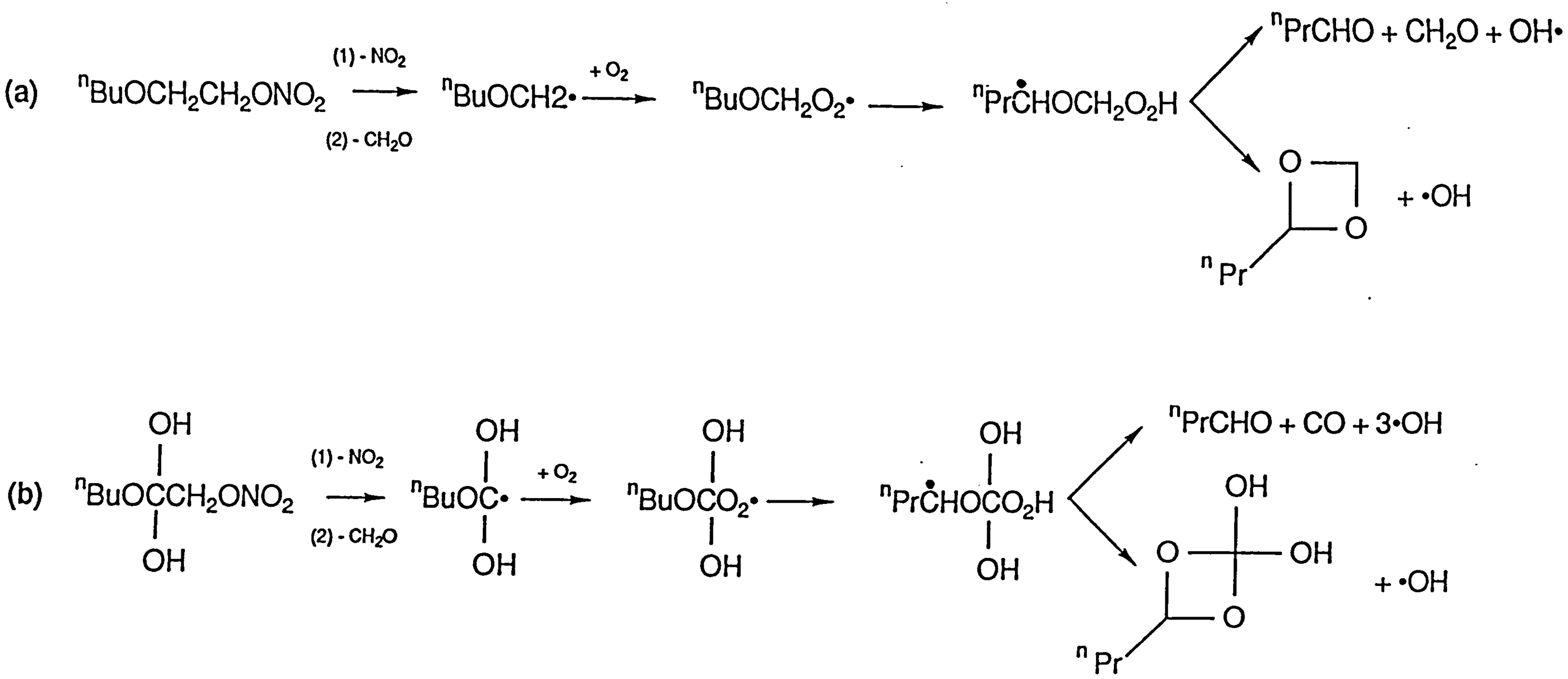

Figure (6.1) The pyrolyses in oxygen of (a) 2-^{n}butylethyl nitrate and (b) β,β-dihydroxy-2-^{n}butoxyethyl nitrate.

REFERENCES

1. J.S. Bogen and G.C. Wilson. Pet. Refiner. 272, 23, 1944.
2. G.F. Obert. Internal Combustion Engines and Air Pollution. Intext Educational Publishers, New York, 1968.
3. L.J. Kirsch. Private Communication.
4. K. Selby. Private Communication.
5. A. Fish, W.W. Haskell and I.A. Read. Proc. R. Soc. London, 261, A323, 1969.
6. L. Batt and G.N. Robinson. The Chemistry of Amino, Nitroso and Nitro Compounds and their derivatives, Ed. S. Patai, Chichester, J. Wiley, 417, 1982.
7. W.H. Richardson and H.E. O'Neil. Comprehensive Chemical Kinetics, Vol. 5, Eds. C.H. Bamford and C.F.H. Tipper, Elsevier, Amsterdam, 381, 1972.
8. L. Batt and M.T.H. Lin. The Chemistry of Peroxides, Ed. S. Patai, Chichester, J. Wiley, 685, 1984.
9. J. Heicklen. Adv. in Photochem. 177, 14, 1988.
10. S.W. Benson and J.H. Buss. J. Chem. Phys. 546, 29, 1958.
11. S.W. Benson, F.R. Cruickshank, D.M. Golden, C.R. Haugen, H.E. O'Neil, A.S. Rodgers, R. Shaw and R. Walsh. Chem. Rev. 279, 69, 1969.
12. D.H. Shaw and H.O. Pritchard. Canad. J. Chem. 2721, 46, 1968.
13. C. Leggett and J.C.J. Thynne. Trans. Farad. Soc. 2504, 63, 1967.
14. L. Batt and G.N. Rattray. Int. J. Chem. Kinet. 1183, 11, 1979.
15. J.R. Barker, S.W. Benson and D.M. Golden. Int. J. Chem. Kinet. 31, 9, 1977.

16. K.A. Sahetchian, R. Rigny, N. Blin and A. Heiss. J. Chem. Soc. Farad. Trans. II, 2035, 83, 1987.

17. L. Batt, R.T. Milne and R.D. McCulloch. Int. J. Chem. Kinet. 567, 9, 1977.

18. L. Batt and R.T. Milne. Int. J. Chem. Kinet. 549, 9, 1977.

19. L. Batt and R.T. Milne. Int. J. Chem. Kinet. 141, 9, 1977.

20. L. Batt, T.S.A. Islam and G.N. Rattray. Int. J. Chem. Kinet. 931, 10, 1978.

21. D.M. Golden, G.N. Spokes and S.W. Benson. Angew. Chem. 534, 12, 1973.

22. G.D. Mendenhall, D.M. Golden and S.W. Benson. Int. J. Chem. Kinet. 725, 7, 1978.

23. A.C. Baldwin and D.M. Golden. Chem. Phys. Letts. 108, 60, 1978.

24. J.B. Levy. J. Am. Chem. Soc. 3254, 76, 1954.

25. R. Longoria. D.Phil. Thesis, University of Aberdeen, 1983.

26. L. Batt and R.D. McCulloch. Int. J. Chem. Kinet. 491, 8, 1976.

27. L. Batt. Int. Rev. Phys. Chem. 53, 6, 1987.

28. L. Batt and G.N. Robinson. Int. J. Chem. Kinet. 1053, 14, 1982.

29. D. Gutman, N. Sanders and J.E. Butler. J. Phys. Chem. 66, 86, 1982.

30. G. Hancock. J. Chem. Soc. Farad. Trans. II, 429, 84, 1988.

31. S. Dobe, T. Berces and F. Marta. Int. J. Chem. Kinet. 329, 18, 1986.

32. S.L. Hirst and L.J. Kirsch. Combustion modelling in reciprocating engines, Ed. C. Amann and J. Mattavi, Plenum, 193, 1980.

33. M.P. Halstead, L.J. Kirsch, A. Prothero and C.P. Quinn. Proc. R. Soc. London, 515, A346, 1975.

34. R.A. Cox and J.A. Cole. Comb. and Flame, 109, 60, 1985.

35. L.J. Kirsch and C.P. Quinn. J. de Chemie Physique, 459, 82, 1985.

36. N.N. Semenov. Chemical Kinetics and Chain Reactions, Oxford University Press, 1935.

37. A. Fish. A.C.S. Adv. Chem. Ser. 69, 76, 1968.

38. J.H. Knox. Comb. and Flame, 297, 9, 1965.

39. R.R. Baldwin, M.W.M. Hisham and R.W. Walker. J. Chem. Soc. Farad. Trans. I, 1615, 78, 1982.

40. S.W. Benson. Prog. Energy Comb. Sci. 125, 7, 1981.

41. M.C. Sauer. Adv. Rad. Chem. 97, 5, 1976.

42. L.S. Kershenbaum and P.W. Leaney. Ind. Eng. Chem. Process Dev. 780, 25, 1986.

43. L.S. Kershenbaum and P.W. Leaney. Ind. Eng. Chem. Res. 369, 26, 1987.

44. C. Morley. Proc. Twenty-Second Symp. (Int.) on Comb. 911, 1988.

45. J.H. Raley, F.F. Rust and W.E. Vaughan. J. Am. Chem. Soc. 88. 70, 1948.

46. F.W. Birss, C.J. Danby and C.N. Hinshelwood. Proc. R. Soc. London, Ser. A. 154, 239, 1957.

47. L. Batt and S.W. Benson. J. Chem. Phys. 895, 36, 1962 ; 3031, 38, 1963.

48. J. Murowski, J.S. Roberts and M. Swarc. J. Chem. Phys. 698, 19, 1951.

49. M.T. Jaquiss, J.S. Roberts and M. Swarc. J. Am. Chem. Soc. 6005, 74, 1952.

50. G.O. Pritchard, H.O. Pritchard and A.F. Trotman-Dickenson. J. Chem. Soc. 1425, 1954.

51. A.R. Blake and K.O. Kutschke. Can. J. Chem. 1462, 37, 1959.

52. F.P. Lossing and A.W. Tickner. J. Chem. Phys. 907, 20, 1952.

53. M.F.R. Mulcahy and D.J. Williams. Aust. J. Chem. 534, 14, 1961.

54. H. Price and R.T.K. Baker. J. Chem. Educ. 614, 42, 1965.

55. W.S. Affleck and A. Thomas. Proc. Instn. Mech. Engrs. 365, 183, 1968.

56. H.C. Christensen, J. Ericksen and P.B. Pagsberg. J. Phys. Chem. 582, 83, 1979.

57. T. Hvild and S.O. Nielson. Rev. Sci. Instrum. 1198, 43, 1972.

58. M.T. MacPherson, M.J. Pilling and M.J.C. Smith. J. Phys. Chem. 2268, 89, 1985.

59. V.C. Sekara and C.S. Marvel. J. Am. Chem. Soc. 345, 55, 1933.

60. F. Welch, H.R. Williams and M.S. Mosher, ibid, 551, 77, 1954.

61. A.I. Vogel. Textbook of Practical Organic Chemistry, Longman Fourth Edition, 1978.

62. A.O. Johnson and A. Pelter. J. Chem. Soc. Part 1, 520, 1964.

63. R.M. Harrison and F.J. Stevenson. J. Gas Chromatography, 240, 1965.

64. S.B. Dave. J. Chromatographic Science, 389, 7, 1969.

65. Supelco Int. Catalogue 24. Supelco Chromatography Suppliers 1986.

66. R.L. Grob. Modern Practice of Gas Chromatography, Second Edition, Wiley, 1977.

67. M.S. Kharasch, A. Fono, W. Nudenberg. J. Org. Chem. 105, 16, 1951.

68. S.W. Benson. Thermochemical Kinetics, Wiley, N. York, 1976.

69. K.Y. Choo and S.W. Benson. Int. J. Chem. Kinet. 833, 13, 1981.

70. H.C. Bailey and G.W. Godin. Trans. Farad. Soc. 68, 52, 1956.

71. J.F. Griffith, M.F. Gilligan and P. Gray. Comb. and Flame, 11, 24, 1975.

72. L. Batt. Int. J. Chem. Kinet. 977, 11, 1979.

73. R.J. Balla, H.H. Nelson and J.R. McDonald. Chem. Phys 323. 99, 1985.

74. W.P.L. Carter, A.C. Lloyd, J.L. Sprung and J.N. Pitts, Jnr. Int. J. Chem. Kinet. 11, 45, 1979.

75. R.A. Cox, K.F. Patrick and S.A. Chant. Environ. Sci. Tech. 587, 15, 1981.

76. H. Niki, P.D. Maker, C.M. Savage and L.P. Breitenbach. J. Phys. Chem. 2698, 85 1981.

77. P. Morobito and J. Heicklen. Bull. Chem. Soc. Jpn. 2641, 60, 1987.

78. M.B. Colket, D.W. Naegeli, F.L. Dryer and I. Glassman. Env. Sci. Tech. 43, 8, 1974.

79. W.A. Pryor, G.L. Kaplen. J. Amer. Chem. Soc. 4234, 86, 1964.

80. E.W.R. Steacie and W.McF Smith. J. Chem. Phys. 504, 4, 1936.

81. H.O. Pritchard. Comb. and Flame, 415, 75. 1989.

82. S.W. Benson and G.N. Spokes. J. Phys. Chem. 1182, 72, 1968.

83. K.A. Sahatchian, A. Heiss, R. Rigny and R.I. Ben-Aim. Int. J. Chem. Kinet. 1325, 14, 1982.

84. L.J. Kirsch. Private Communication.

85. J.P. Buxton. Private Communication.

86. D.L. Baulch, D.D. Drysdale and D.G. Horne. Evaluated Kinetic Data for High Temperature Reactions, Vol. 2, Homogeneous gas phase reactions of the H_2-N_2-O_2 system. Butterworth, 1976.

87. L.J. Kirsch. Private Communication.

88. A. Prothero. Private Communication.

89. F.S. Dainton. Chain Reactions, Methuen, 1956.

90. F.H. Pollard and R.M.H. Wyatt. Trans. Farad. Soc. 630, 49, 1953.

91. C.A. McDowell and J.H. Thomas, ibid, 1030, 46, 1950.

92. S. Koda and M. Tanbaka. Comb. Sci. and Tech. 165, 47, 1986.

93. C.J. Howard. J. Am. Chem. Soc. 6937, 102, 1980.

94. R.W. Walker. Specialist Periodical Reports, Reaction Kinetics, Vol. 1, 161, 1974.

95. R.W. Walker. Int. J. Chem. Kinetic. 573, 17, 1985.

96. K. Selby. Private Communication.

97. A. Fish. Organic Peroxides, Vol. 1, Ed. D. Swern, Wiley, 1970.

98. H. Niki, P.D. Maker, C.M. Savage and L.P. Breitenbach. J. Phys. Chem. 2190, 87, 1983.

99. G.L. Vaghjiani and A.R. Ravishankara. J. Phys. Chem. 1948, 93, 1989.

100. R.N. Perutz. Private Communication.

101. V.J. Simpson, Private Communication.

102. G. Herzberg and J. Shoosmith. Canad. J. Physics. 523, 34, 1956.

103. P. Pagsberg. Private Communication.

104. G.H. Dieke and H.M. Crosswhile. Report No. 87 (Bubblebee series). The John Hopkins University, Baltimore, Maryland.

105. D.A. Parkes. 15th Int. Symp. on Comb. Tokyo 1974 (The Comb. Inst. Pittsburgh, 1975), 795.

106. G.C. Fettis, J.H. Knox and A.F. Trotman-Dickenson. J. Chem. Soc. 4177, 1980.

107. J.H. Knox and R.L. Nelson. Trans. Farad. Soc. 937, 55, 1959.

108. R. Atkinson. Int. J. Chem. Kinet. 555, 18, 1986.

109. M. Keiffer, A.J. Miscampbell and M.J. Pilling. J. Chem. Soc, Faraday Trans. II, 505, 84, 1988.

110. P.H. Taylor, J.A. D'Angelo, M.C. Martin, J.H. Kosher, B. Dellinger. Int. J. Chem. Kinet. 829, 21, 1989.

111. C.J. Hochanadel, J.A. Gormley, J.W. Boyle and P.J. Ogren. J. Phys. Chem. 3, 81, 1977.

112. M.T. Macpherson, M.J. Pilling and M.J.C. Smith. Chem. Phys. Letts. 430, 94, 1983.

113. D.A. Parkes, D.M. Paul and C.P. Quinn. J. Chem. Soc. Farad. Trans. I, 1935, 72, 1976.

114. D.A. Parkes and C.P. Quinn. J. Chem. Soc. Faraday Trans. I, 1952, 72, 1976.

115. C. Anastasi and N.L. Arthur. J. Chem. Soc. Faraday Trans. II, 277, 83, 1987.

116. H. Adachi, N. Basco and D.G.L. James. Int. J. Chem. Kinet. 995, 11, 1979.

117. H. Adachi and N. Basco. Int. J. Chem. Kinet. 367, 13, 1981.

118. C. Morley. Private Communication.